

Plasma-assisted atomic layer deposition : an in situ diagnostic study

Citation for published version (APA):

Langereis, E. (2008). *Plasma-assisted atomic layer deposition : an in situ diagnostic study*. [Phd Thesis 1 (Research TU/e / Graduation TU/e), Applied Physics and Science Education]. Technische Universiteit Eindhoven. <https://doi.org/10.6100/IR637260>

DOI:

[10.6100/IR637260](https://doi.org/10.6100/IR637260)

Document status and date:

Published: 01/01/2008

Document Version:

Publisher's PDF, also known as Version of Record (includes final page, issue and volume numbers)

Please check the document version of this publication:

- A submitted manuscript is the version of the article upon submission and before peer-review. There can be important differences between the submitted version and the official published version of record. People interested in the research are advised to contact the author for the final version of the publication, or visit the DOI to the publisher's website.
- The final author version and the galley proof are versions of the publication after peer review.
- The final published version features the final layout of the paper including the volume, issue and page numbers.

[Link to publication](#)

General rights

Copyright and moral rights for the publications made accessible in the public portal are retained by the authors and/or other copyright owners and it is a condition of accessing publications that users recognise and abide by the legal requirements associated with these rights.

- Users may download and print one copy of any publication from the public portal for the purpose of private study or research.
- You may not further distribute the material or use it for any profit-making activity or commercial gain
- You may freely distribute the URL identifying the publication in the public portal.

If the publication is distributed under the terms of Article 25fa of the Dutch Copyright Act, indicated by the "Taverne" license above, please follow below link for the End User Agreement:

www.tue.nl/taverne

Take down policy

If you believe that this document breaches copyright please contact us at:

openaccess@tue.nl

providing details and we will investigate your claim.

Plasma-assisted atomic layer deposition

an *in situ* diagnostic study

PROEFSCHRIFT

ter verkrijging van de graad van doctor aan de
Technische Universiteit Eindhoven, op gezag van de
Rector Magnificus, prof.dr.ir. C.J. van Duijn, voor een
commissie aangewezen door het College voor
Promoties in het openbaar te verdedigen
op maandag 6 oktober 2008 om 16.00 uur

door

Erik Langereis

geboren te Geldrop

Dit proefschrift is goedgekeurd door de promotor:

prof.dr.ir. M.C.M. van de Sanden

Copromotor:

dr.ir. W.M.M. Kessels

This research was financially supported by the Dutch Technology Foundation STW (EMM.6174)



Printed and bound by: Printservice Technische Universiteit Eindhoven.

Cover image: Onno Gabriel and Erik Langereis.

Cover design: Bregje Schoffelen, Oranje Vormgevers, Eindhoven.

A catalogue record is available from the Eindhoven University of Technology Library

ISBN 978-90-386-1368-0

Contents

A	Framework and overview of the research	1
I	Application and synthesis of ultrathin films	3
II	Research areas within the field of atomic layer deposition	5
III	Outline of the thesis	11
IV	Exploration of plasma-assisted atomic layer deposition	14
V	Outlook	29
B	Publications	37
1	<i>In situ</i> spectroscopic ellipsometry study on the growth of ultrathin TiN films by plasma-assisted atomic layer deposition	39
I	Introduction	41
II	Experimental Setup	43
III	Spectroscopic Ellipsometry	45
IV	Results and Discussion	52
V	Conclusions	63
2	Synthesis and <i>in situ</i> characterization of low-resistivity TaN_x films by remote plasma atomic layer deposition	69
I	Introduction	70
II	Experimental details	72
III	Spectroscopic ellipsometry on TaN _x films	75
IV	TaN _x film growth and material properties	80
V	Conclusions	92
3	Plasma-assisted atomic layer deposition of Al₂O₃ moisture permeation barriers on polymers	99

4	Surface chemistry of plasma-assisted atomic layer deposition of Al₂O₃ studied by infrared spectroscopy	109
5	<i>In situ</i> spectroscopic ellipsometry as a versatile tool to study atomic layer deposition	119
I	Introduction	120
II	Spectroscopic ellipsometry	123
III	Parametrization of dielectric functions	129
IV	ALD film growth studied by <i>in situ</i> SE	137
V	Conclusions	155
VI	Experimental	156
	Summary	163
	List of publications related to this work	167
	Acknowledgments	171
	Curriculum Vitae	175

Part A

Framework and overview of the research

I Application and synthesis of ultrathin films

With the optical, mechanical, electrical, and chemical properties of ultrathin films (<100 nm) being used in numerous application areas, the synthesis of such functional thin films has become a key technology in present-day society. Especially in integrated circuits (ICs) that are present in everyday electronic devices, such as in microprocessors in computers, televisions, cellular phones and automobile electronics, ultrathin films provide a broad range of functionalities required. The miniaturization and diversification in semiconductor industry can even be considered as the main technological driver for developments in ultrathin film synthesis. By definition of the future technology nodes in the international technology roadmap for semiconductors (ITRS) [1], the continuous development of faster and more compact electronic equipment can basically be thought of as squeezing the same or (preferably) even more functionality on a smaller area of the microchip. In the complex manufacturing schemes of these ICs, the synthesis of ultrathin films by deposition methods is an essential manufacturing step.

The most prominent research challenges faced in the synthesis of ultrathin films can be exemplified by the requirements on the complementary metal-oxide-semiconductor (CMOS) transistors and the high-density dynamic random access memory (DRAM) trench capacitors. Due to constraints of a high capacitance and minimal leakage current of the gate oxide in CMOS transistors, high- k dielectrics are required to replace the conventionally used SiO₂ dielectric that has a dielectric constant of $k = 3.9$ [2, 3]. Contrary to the thermal oxidation process to form the ~ 1 nm thick SiO₂ gate oxide, the research challenge lies here in the fact that the nanometer thick high- k dielectric film has to be *deposited* with an ultimate control of thickness and material properties. The requirements on film deposition are even further challenged in DRAM trench capacitors. For these capacitors, ultrathin metallic and high- k dielectric layers have to be deposited highly *conformally* inside high-aspect ratio trench structures.¹ The development of novel deposition methods that provide such ultimate growth control and conformality is essential to extend the possibilities of film synthesis currently provided by physical and chemical vapor deposition techniques. In this respect, these novel deposition methods are critical for the continuation of the technological progress in the semiconductor industry.

The atomic layer deposition (ALD) technique is considered to be one

¹The conformality or step coverage can be defined by the ratio of the film thicknesses at the top and bottom of a 3D structure. Perfect conformal growth, i.e., a step coverage of 100 %, refers to a deposition that yields equal film thickness throughout the structure.

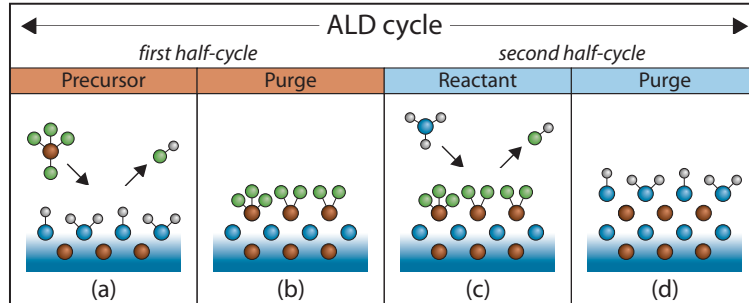


Figure 1: Atomic layer deposition (ALD) illustrated for the two half-cycles of the deposition process. The first half-cycle consists of (a) self-limiting adsorption of precursor molecules on the surface groups available and (b) a purge step to remove the volatile reaction by-products and the excess of precursor dosed. After the first half-cycle, a submonolayer of precursor has chemisorbed on the surface. During the second self-limiting surface reaction (c), the surface is exposed to reactant molecules that react with the surface groups of the adsorbed precursor. The second half-cycle is completed by (d) another purge step to remove the volatile reaction by-products and the excess of reactant dosed. After the full ALD cycle, a submonolayer of material is deposited and the surface groups are again similar to the start of the cycle. Subsequently, the cycle can be repeated to deposit a film with the thickness targeted.

of the primary candidates to fulfil the strict requirements on ultrathin film growth set by semiconductor industry [4–7]. By the virtue of two separate self-limiting surface reactions, ALD has the ability to control film growth and material properties at the atomic level, as schematically illustrated in Fig. 1. The essence of ALD is that the amount of material deposited is determined by the amount of surface adsorption sites initially available rather than by the particle flux impinging on the surface. Thus when sufficient precursor and reactant molecules are dosed to saturate the surface chemistry, (ideally) a monolayer of material is deposited per cycle. ALD provides therefore “digital” thickness control, i.e., the ability to increase the film thickness layer-by-layer by repeating ALD cycles. Moreover, ALD film growth is highly uniform and yields excellent conformality because at every available surface site only one precursor/reactant molecule can adsorb regardless the incoming particle flux or whether these surface sites are distributed over a large surface area or in a demanding 3D topology.

The most established and most studied ALD configuration is the so-called thermal ALD process in which the surface chemistry is driven by thermal energy delivered to the substrate. Over the years many ALD pro-

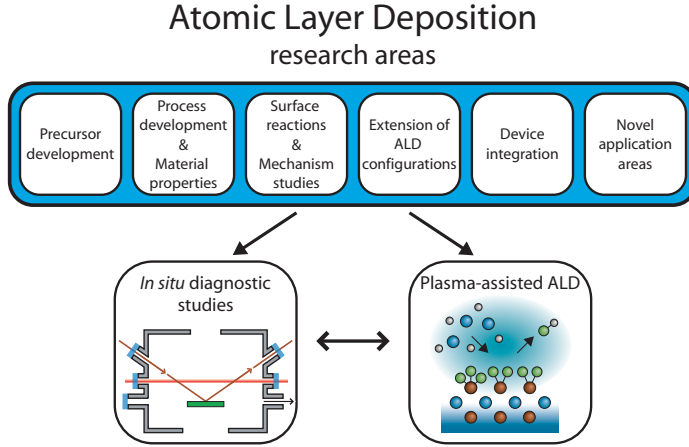


Figure 2: The different research areas related to the development and application of the ALD technique. In particular, the plasma-assisted ALD configuration and *in situ* diagnostics studies will be addressed in this work.

cesses for thin films of inorganic materials have been designed, ranging from pure elements to compounds with oxygen, nitrogen, and sulphur, as reviewed by others [4–10]. Recently, an ALD scheme for organic materials was even designed using bifunctional monomers [11]. Well-established thermal ALD processes have already been implemented for ultrathin film synthesis in industrial applications. For example in Samsung’s synchronic DRAM transistors, ALD is used to deposit $\text{Al}_2\text{O}_3/\text{HfO}_2$ dielectric bilayers and TiN electrodes [12]. More recently, Hf-based high- k dielectrics deposited by ALD are used as gate oxide into Intel’s 45 nm processor [13].

II Research areas within the field of atomic layer deposition

In order to fully exploit the opportunities of the ALD technique, research is carried out in different areas, as schematically shown in Fig. 2. The work described in this thesis aims mainly at the development of new ALD configurations and at the surface reaction and mechanism studies. More specifically, the configuration of plasma-assisted ALD and *in situ* diagnostic studies will be elaborated upon. The research, however, also contributes to the ALD process development and provides insight into the material properties obtained. Moreover, the opportunities of plasma-assisted ALD will be illustrated by demonstrator experiments in novel application areas.

A Plasma-assisted atomic layer deposition

New ALD configurations are pursued in order to extend to possibilities provided by the ALD technique. One approach actively investigated is to supply additional reactivity to the process. In case of some materials, the suitable combination of precursor and reactant is not (yet) available for the chemistry to be driven by thermal energy solely. In other cases, it is from a manufacturing perspective simply not allowed to supply the thermal energy needed for the thermal ALD process, for example, for deposition on temperature-sensitive substrates. For example, the ALD of metal oxides, the use of O_3 as a strong oxidant source [14–16] is being researched to realize improved material properties and/or to deposit at lower temperatures than common for thermal ALD with H_2O [7, 8]. For similar purposes also the use of an O_2 plasma is currently being studied [17–20], however, with the notion that the use of a plasma in ALD processes can be extended to a wider variety of materials than only oxides.²

Plasma-assisted (or plasma-enhanced) ALD is a relatively novel configuration that benefits from the additional reactivity provided by plasma species [18, 21–23]. The essence of plasma-assisted ALD lies in the fact that the reactant species during the second ALD half-reaction are made reactive in a plasma environment. Basically, this implies that a part of the chemical energy required for ALD reactions is supplied by activated reactants from the gas phase. This aspect is conceptually different from thermal ALD processes, where the chemistry occurs fully at the surface. The plasma-assisted ALD configuration yields several potential benefits in addition to the earlier mentioned ultimate growth control intrinsic to the ALD technique [18]:

- Improved material properties including higher film density, lower impurity levels, and better control of film composition and microstructure;
- Deposition at reduced substrate temperatures due to the increased reactivity provided by the plasma species;
- Increased growth per cycle as well as reduced purging steps, especially at low substrate temperatures;

²In these new ALD configurations, the additional reactivity is supplied through surface reactions by O atoms created by decomposition of O_3 at the surfaces or by O radicals (and other plasma species) formed in an O_2 plasma.

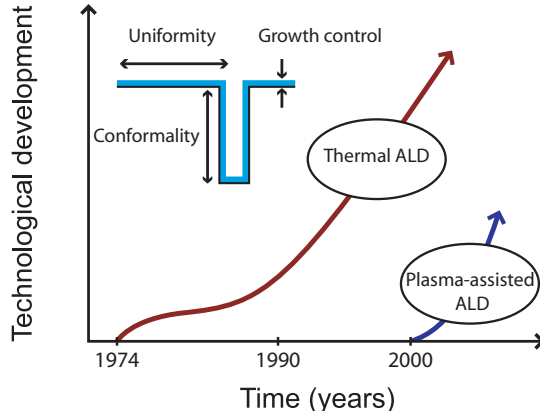


Figure 3: The technological development of thermal and plasma-assisted ALD processes schematically illustrated as a function of time. The development of ALD relies on two important research aspects, i.e., the industrial need for ultrathin film deposited with ultimate growth control and the understanding of the ALD process itself to fully exploit its possibilities. In the inset, the key aspects of ALD, i.e., growth control, uniformity, and conformality, are depicted.

- Good control of film stoichiometry by tailoring the plasma step as well as the possibility to introduce dopants by co-doping during the plasma step;
- Increased choice of precursors and obtainable materials, including high quality single element films (metals), difficult to obtain by thermal ALD;
- More process versatility due to the possibility of *in situ* substrate conditioning, plasma densification, nitridation, etc.

As a consequence of the use of a plasma, various plasma species (i.e., radicals, ions, and electrons) impinge on the surface of the film during the reactant half-cycle in plasma-assisted ALD. These plasma species can all contribute to the ALD chemistry. Considering the various methods of plasma generation (e.g., direct or remote plasma [18]) and the different feed gasses that can be used for plasma operation (e.g., commonly O_2 , H_2 , N_2 , and combinations thereof are used), a large variety of materials can be synthesized by plasma-assisted ALD.

In view of the recent technological development as schematically shown in Fig. 3, plasma-assisted ALD has a high potential in being complementary to thermal ALD and thereby extending the possibilities of the ALD

technique in general. Moreover, because of the industrial acceptance of thermal ALD that is currently taking place, the time to industrial readiness for plasma-assisted ALD can potentially be much shorter because it can basically be considered a small hardware adaptation of thermal ALD. The possibilities and opportunities of plasma-assisted ALD are, however, still relatively unexplored. The majority of research reported so far focusses on the material properties obtained rather than on acquiring fundamental understanding of the plasma-assisted ALD process. Obviously, the latter aspect is as important to fully exploit plasma-assisted ALD and to find new applications areas. In general, the following research objectives have to be addressed to understand and exploit the merits delivered by plasma-assisted ALD:

- Understand the fundamentals of the reaction mechanisms of plasma-assisted ALD.
- Explore the possibilities for plasma-assisted ALD to increase the choice in chemistry and materials.
- Investigate the opportunity for plasma-assisted ALD to obtain improved material properties and to realize deposition at reduced substrate temperatures.
- Demonstrate the industrial feasibility of the plasma-assisted ALD process.

B *In situ* diagnostic studies of ALD

In order to study the film thickness and material properties of the nanometer thick films deposited by ALD, highly sensitive diagnostics are required. The majority of the characterization of the films in the literature is carried out by means of *ex situ* techniques. Also *in situ* studies have been reported and these studies have mainly been focussed on elucidating the ALD reaction mechanism. Commonly employed *in situ* techniques are infrared spectroscopy [24–27] and quartz crystal microbalance [28–30] to provide insight into the surface species that are formed in the ALD half-cycles and to monitor the film growth. Mass spectrometry is often used to quantify the precursor/reactant dosing and identify the volatile reaction by-products created in the ALD reaction mechanism [28, 30–32].

The need for *in situ* studies during the ALD process will be further discussed in this section and the *in situ* approach can be considered relevant

to ALD in general regardless the ALD configuration employed (e.g., thermal or plasma-assisted ALD). As already mentioned, these kinds of studies are essential to address the fundamentals of the ALD reaction mechanism. Moreover, *in situ* techniques provide the opportunity for process monitoring, optimization, and control of the ALD process. The last is illustrated in Fig. 4 for the change of film thickness with ALD cycles.

Fundamentals of ALD reaction mechanism: A fundamental understanding of the reaction mechanisms is required to improve the existing ALD processes and to develop new ALD processes and precursors to enable deposition of novel materials. Fundamental insight into the ALD reaction mechanisms is also required to comprehend the dependence of growth rate and material properties on the deposition temperature. In particular for plasma-assisted ALD, the reaction mechanisms have been scarcely addressed from a fundamental point-of-view and it is often only speculated upon the mechanism governing the process. The challenge is to elucidate the reaction mechanisms during the plasma ALD half-cycle to understand (some of) the benefits of plasma-assisted ALD.

The reaction mechanisms can be derived from the kind of surface species created and volatile reaction by-products formed during the surface reactions of the precursor and reactants species. Obviously, sensitive *in situ* techniques are required to probe the submonolayers of surface groups produced and to detect the equivalent amounts of volatile reaction by-products in the gas phase.

Process monitoring: The ALD process lends itself particularly well for *in situ* studies, because the inherent cycle-by-cycle deposition allows to halt the deposition for sensitive measurements in between the ALD cycles. Data acquisition in between the cycles provides, thus, the opportunity to monitor and address various growth aspects of the ALD process. Considering the amount of data that can easily be acquired, i.e., from cycle-by-cycle acquisition to, typically, after every 10–100 cycles, the influence of thickness on the material properties can be addressed in detail.

Since the ALD process can be continued after data acquisition as illustrated in Fig. 4, the nucleation behavior [being I (ideal), II (delayed), or III (accelerated)] and its dependence on the substrate materials employed can be deduced from the growth curve obtained in a single deposition run. Furthermore, the ALD growth rate (also referred to as the growth per cycle) can be accurately determined from the linear ALD growth regime (after point A). In contrast, *ex situ* studies require separate samples for every thickness to be examined and different samples need to be combined

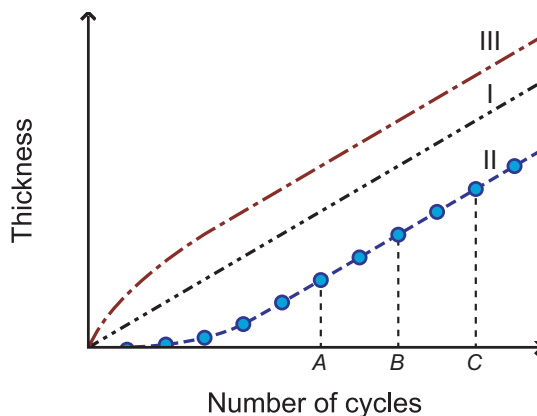


Figure 4: Monitoring the film thickness as a function of number of cycles during an ALD process. Three kinds of nucleation behavior of the ALD films can typically be distinguished during the first few cycles. ALD process with: I) immediate constant growth rate [ideal process], II) [pronounced] nucleation delay, and III) accelerated growth. The circles illustrate data acquisition during the film growth. In this example, it is observed that the film nucleation is completed at point *A* and the growth rate can be calculated from the differences between point *A* and *B*. After changing the ALD process parameters at point *B*, its effect on growth rate can be calculated from the slope of the curve between *B* and *C*.

in order to investigate the thickness dependence of the data.

Process optimization: For every ALD process, the self-limiting character of its surface chemistry has to be verified. This is reflected by the fact that the amount of material deposited per cycle is becoming independent of the ALD process parameters, such as the precursor/reactant dosing and purge times in the cycle. Moreover, to shorten the cycle time and considering the expensive precursors often employed, the ALD process has to be optimized such that the excess of precursor/reactant is minimized without compromising on the self-limiting character of the process.

One approach to optimize the ALD process is by *in situ* thickness monitoring during the ALD process (Fig. 4). By scanning the ALD process window in a single deposition run, the influence of the process parameters on the growth rate can be determined from the *increase* in thickness with the number of ALD cycles employed. Another way of optimizing the precursor/reactant dosing is by examining the volatile reaction by-products formed in the ALD process. Since the amount of material deposited per cycle is limited, also a maximum amount of reaction by-

products can be formed. This implies that by monitoring the amount of reaction by-products in real time, the optimal precursor/reactant dosing of the ALD process can be derived. These *in situ* methods mentioned are particularly fast compared to the laborious process optimization employing *ex situ* methods. In that case (at least) two films with a different thicknesses have to be deposited for every growth condition to extract the growth rate and many depositions are required for a comprehensive scan of the different ALD process parameters.

Process control: Although the ALD process is acknowledged for its layer-by-layer growth, fluctuations in deposition conditions (e.g., substrate temperature, chamber pressure, or wall conditioning before start of deposition) can influence the film growth and the reproducibility of the ALD process. Process control by stand-alone *in situ* techniques is, therefore, becoming increasingly important considering the precise thickness values and material properties of the ALD films required in industrial application.

By accurately monitoring the film thickness with the number of deposition cycles, immediate insight into the nucleation behavior and ALD growth rate can be obtained (Fig. 4). This online thickness information can be used to actively adjust the amount of cycles during deposition such that the ALD process is automatically stopped when the targeted film thickness is reached. On the other hand also by monitoring the amount of precursor/reactant dosed and the amount of volatile reaction by-products created, enables to immediately detect hardware failures, such as non-opening valves, gas flow fluctuations or precursor/reactant shortage. In that case, specific action can be undertaken, either in process interruption or by automatically adding more deposition cycles, etc.

III Outline of the thesis

The aim of the work described in this thesis is to investigate the possibilities and merits delivered by the plasma-assisted ALD technique for certain materials and processes. The research approach adopted is to employ various *in situ* diagnostics to address several aspects of the plasma-assisted ALD process. This approach is twofold, since (i) detailed insights are obtained into growth behavior and material properties of these plasma-assisted ALD processes, while (ii) the development of *in situ* techniques to monitor and control the film growth in industrial environments becomes increasingly important for the ALD process in general.

The research was carried out in the group “Plasma & Materials Pro-

cessing” (PMP) at the Department of Applied Physics of the Eindhoven University of Technology. The group has an extensive expertise on plasma chemistry and physics, plasma-surface interaction, and synthesis of materials by means of plasma-enhanced chemical vapor deposition. Moreover, the availability of various dedicated diagnostics make the PMP group an exceptional environment for detailed studies of the plasma-assisted ALD process. The scientific work has been financially supported by the Dutch technology foundation STW (Stichting Technische Wetenschappen) in the project entitled: “Plasma-assisted atomic layer deposition for processing at the nano-scale”. One of the most important aspects of this project is the active collaboration with institutes and industrial partners in order to assess new ALD processes and materials that have a high potential for industrial application. The partners included in this project were Delft University of Technology, FOM Institute for Plasma Physics Rijnhuizen, ASM, NXP Semiconductors Research, Philips Research, Hauzer Technocoating, OTB Engineering, and Oxford Instruments Plasma Technology. The work described in this thesis complements the thesis work of Heil [18], which was carried out in the same STW project and focussed more on the reaction mechanisms of plasma-assisted ALD and the material properties obtained.

At the beginning of this work, the plasma-assisted ALD process was at its initial stages in the PMP group and the homebuilt ALD-I reactor was just installed [18]. The plasma-assisted ALD of TiN was the first process that was extensively studied and, in particular, the strength of the combination of *in situ* spectroscopic ellipsometry with ALD was immediately prominent in determining thickness and material properties of the films. Subsequently, the plasma-assisted ALD processes of Al₂O₃ and TaN_x were addressed extensively on the ALD-I. Some of the Al₂O₃ depositions were also carried out on the FlexALTM reactor that has been developed by Oxford Instruments Plasma Technology [33] and which is installed in the cleanroom of the Department of Applied Physics (as a part of the collaboration with Oxford Instruments Plasma Technology within the STW project). In addition to the research carried out in the PMP group, the film nucleation of thermal ALD La₂O₃ films was studied during a 3 months internship in the research group of professor Chabal at the Rutgers University (New Jersey, USA).

The *in situ* approach chosen to study the plasma-assisted ALD processes will be further exemplified in Sec. IV of this introductory chapter. First, the different *in situ* diagnostics employed throughout this work will

be introduced and their merits in studying the (plasma-assisted) ALD process will be illustrated by three specific research cases. This chapter will be concluded by an outlook to the future.

The results have been published as several separate articles in different international scientific journals. Each article is presented as a chapter in Part B of this thesis, as outlined below. The plasma-assisted ALD process of TiN as studied by *in situ* spectroscopic ellipsometry is discussed in Chapter 1. The possibility to tailor and tune the TaN_x material properties in plasma-assisted ALD is described in Chapter 2. The feasibility for plasma-assisted ALD with respect to low temperature deposition of Al₂O₃ permeation barriers is reported in Chapter 3. The surface chemistry of plasma-assisted ALD of Al₂O₃ was unveiled by infrared transmission spectroscopy as is described in Chapter 4. An overview of the merits of *in situ* spectroscopic ellipsometry when applied to ALD is presented in Chapter 5.

Overview of the chapters in Part B:

- Chapter 1:** *In situ spectroscopic ellipsometry study on the growth of ultrathin TiN films by plasma-assisted atomic layer deposition*
E. Langereis, S. B. S. Heil, M. C. M. van de Sanden, and W. M. M. Kessels, J. Appl. Phys. **100**, 023534 (2006).
- Chapter 2:** *Synthesis and in situ characterization of low-resistivity TaN_x films by remote plasma atomic layer deposition*
E. Langereis, H. C. M. Knoops, A. J. M. Mackus, F. Roozeboom, M. C. M. van de Sanden, and W. M. M. Kessels, J. Appl. Phys. **102**, 083517 (2007).
- Chapter 3:** *Plasma-assisted atomic layer deposition of Al₂O₃ moisture permeation barriers on polymers*
E. Langereis, M. Creatore, S. B. S. Heil, M. C. M. van de Sanden, and W. M. M. Kessels, Appl. Phys. Lett. **89**, 081915 (2006).
- Chapter 4:** *Surface chemistry of plasma-assisted atomic layer deposition of Al₂O₃ studied by infrared spectroscopy*
E. Langereis, J. Keijmel, M. C. M. van de Sanden, and W. M. M. Kessels, Appl. Phys. Lett. **92**, 231904 (2008).
- Chapter 5:** *In situ spectroscopic ellipsometry as a versatile tool to study atomic layer deposition*
E. Langereis, S. B. S. Heil, H. C. M. Knoops, W. Keuning, M. C. M. van de Sanden, and W. M. M. Kessels, submitted for publication.

IV Exploration of plasma-assisted atomic layer deposition

The *in situ* approach adopted in this work to explore the opportunities and possibilities of plasma-assisted ALD will be illustrated in this section. The results shown are exemplary for the work described in this thesis. The *in situ* approach chosen can, however, be considered more comprehensive since it can be transferred to study other ALD processes and materials. Also the merits of plasma-assisted ALD demonstrated are illustrative to this technique and can be used as a guide to further explore its possibilities in the deposition of other materials.

First, the *in situ* diagnostics employed will be briefly introduced and, subsequently, the insights obtained on the ALD process using these diagnostics will be demonstrated by three research cases; (i) the possibility to tailor the material properties in the plasma-assisted ALD of TaN_x films, (ii) the ability to deposit Al_2O_3 films at reduced temperatures by plasma-assisted ALD for application as water permeation barriers, and (iii) the fundamentals of the reaction mechanisms in plasma-assisted ALD of TaN_x and the nucleation behavior of thermal ALD La_2O_3 films.

A Implementation of *in situ* diagnostics on ALD reactors

In this work, the ALD film growth was studied in a home-built reactor equipped with different optical access ports to implement multiple diagnostics simultaneously, as schematically illustrated in Fig. 5. Several aspects of the ALD processes were studied *in situ* by employing spectroscopic ellipsometry, transmission infrared spectroscopy, mass spectrometry, and optical emission spectroscopy. The reactor was designed such that, in principle, both the plasma-assisted and thermal ALD process could be studied for various materials grown in the same reactor. For the plasma-assisted ALD processes, the plasma was generated upstream from the substrate by an inductively coupled plasma source. This remote plasma configuration was chosen because of the relatively high radical flux impinging on the substrate and the low, but non-negligible and (possibly) beneficial ion bombardment energy, as discussed in more detail by Heil [18].

Spectroscopic ellipsometry (SE) has proven itself over the years to be valuable for determination of the thickness and (optical) properties of thin films. Because SE is an optical and non-intrusive technique detecting the change in polarization of light upon reflection from a surface, it has been commonly applied *in situ* to study the film growth as reported

for many physical and chemical vapor deposition methods [34, 35]. The concept of *in situ* SE for thickness monitoring during an ALD process was already reported by Klaus *et al.* [36], however, the application of *in situ* SE did not settle in ALD research at that time. The knowledge, accuracy, and also user-friendliness of ellipsometer systems and related data analysis has improved in the recent years, as can be expressed by the ability to detect changes in nominal film thickness equivalent to 0.01 monolayer.

The use of *in situ* SE during ALD as explicitly done in this work can, therefore, be considered an establishment of the technique in the ALD research field. Moreover, it will be shown that SE is a versatile technique in the characterization of the ALD processes. Besides the accurate thickness information of the nanometer thick ALD films, the parametrization of the energy dispersion of the optical constants enables to extract film properties from the data, such as optical properties (e.g. refractive index, extinction coefficient, and optical band gap) and material properties (e.g., mass density, crystalline phase, electrical resistivity, free electron density, and electron mean free path). The merits of *in situ* SE during ALD will be demonstrated by results obtained on Al_2O_3 , HfO_2 , Er_2O_3 , TiO_2 , Ta_2O_5 , TiN , and TaN_x films.

Transmission infrared spectroscopy has been commonly employed in fundamental studies on the growth of nanometer thick films and, in particular, provides the sensitivity to detect the surface species created in the ALD half-reactions [24–27]. Using a stable broadband infrared light source, infrared spectroscopy can detect the minimal changes in transmission of the infrared light as caused by absorption of chemical bonds in the film. The challenge is to obtain a sufficient signal-to-noise ratio in the infrared measurements such that the absorbance by the surface species and the ALD film can be detected.

In this work, flat substrates are used and the signal-to-noise ratio is improved by extensive averaging of separate transmission measurements.³ The surface species created in the plasma-assisted ALD of Al_2O_3 have been determined by monitoring the ALD film growth onto the potassium bromide (KBr) optical windows themselves. This has the advantage of a high transmitted light intensity and an experimental configuration that is relatively straightforward. A more sophisticated approach is to use Si substrates in the transmission measurements, as has been done to study the

³In the literature, often the infrared absorbance in a single transmission measurement is increased by using high-surface area porous substrates materials and the ALD growth conformality is exploited to effectively coat the interior surface of the substrate [24, 25].

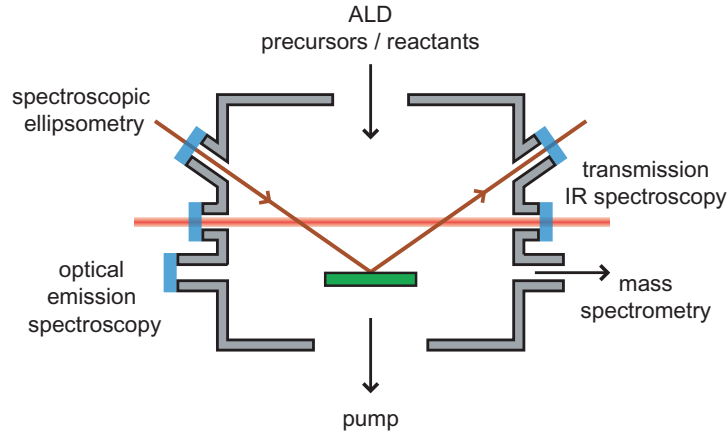


Figure 5: Schematic illustration of the different *in situ* diagnostics implemented on an ALD reactor to address the different aspects of the ultrathin film growth, i.e., thickness and material properties determination by spectroscopic ellipsometry, detection of surface groups and material composition by transmission infrared spectroscopy, and detection of the volatile reaction by-products by mass spectrometry. For plasma-assisted ALD, the light emission by plasma-excited reaction by-products can be recorded by optical emission spectroscopy.

nucleation of thermal ALD La_2O_3 films. These Si substrates can easily be temperature-controlled by employing resistive heating to monitor the ALD film growth at elevated temperatures and to study the interface between the (high- k) film and the Si substrate. Moreover, the effect of an *in situ* post-deposition anneal on the material properties can be addressed.

Mass spectrometry can be used to analyse the amount of precursor/reactant molecules dosed and, moreover, to detect the volatile reaction by-products that are created during the ALD surface reactions. Due to the dissociative ionization of species in the mass spectrometer, the parent species are fragmented and the cracking patterns (or “fingerprint”) of the parent species are detected.

The detection of the volatile reaction by-products created in the plasma-assisted ALD process of Al_2O_3 was described by Heil [18]. In this work, the reducing power of the H_2 plasma will be examined by determination of the reaction by-products by mass spectrometry during the plasma-assisted ALD process of conductive TaN_x films. In order to produce a relatively large amount of reaction by-products, the ALD process is studied at relatively low temperatures ($<150^\circ\text{C}$ as set by using reactor wall heating). As

a consequence, the ALD film growth occurs at the complete interior surface area of the reactor and, in turn, the complete surface area is contributing to the formation of reaction by-products.

Optical emission spectroscopy exploits the fact that the plasma emits light and is, therefore, particularly suited to study the plasma step in plasma-assisted ALD processes. The plasma emission spectrum recorded is composed of spectral lines that originate from the decay of electronically excited states of various plasma species, such as radiating atoms, ions, and molecules. Moreover, the reaction by-products released during the plasma ALD half-cycle can be excited in the plasma as well. These excited reaction by-products can, therefore, emit light in addition to the emission of the “original” plasma species. This additional emission can be probed and traced back to the chemical structure of the species itself, while time dependent monitoring of the emission intensity can be used for process optimization.

Depending on the excited reaction by-product species, the additional emission can be prominent. In particular during plasma-assisted ALD of Al_2O_3 , the excitation of the CO_2 and/or CO reaction by-products resulted in an intense blue “flash” (i.e., a transition from blue to green) during the O_2 plasma step. The extinction of the blue flash can be related to the disappearance of (excited) CO_2 reaction by-products when the surface reactions reach saturation [17, 37]. In fact, this blue is so intense that the saturation of the ALD reaction could be observed by the human eye.⁴ In this work, mainly the plasma emission in the plasma-assisted ALD process of TaN_x is examined revealing the formation of an additional $\text{C}\equiv\text{N}$ radical species which can be related to the ALD surface chemistry.

In addition to the characterization of the ALD processes by the *in situ* techniques aforementioned, extensive *ex situ analysis* has been carried to corroborate the results obtained and, moreover, complement the film characterization of the ALD deposited films with respect to thickness and various material properties. As summarized in Table 1, the *ex situ* techniques employed in this work provide additional information on aspects such as mass density, film closure, film composition, microstructure, grain size, roughness, and electrical resistivity.

⁴For a movie of the plasma emission during a plasma-assisted ALD cycle visit the online article’s HTML reference section of Ref. [17]. Or follow the direct link: <http://netserver.aip.org/cgi-bin/epaps?ID=E-APPLAB-89-331639>

Table 1: Overview of the *in situ* and *ex situ* diagnostics employed in this work to characterize various aspects of the ALD film growth and to unravel the reaction mechanism of each ALD process. *In situ*: spectroscopic ellipsometry (SE), Fourier-transform infrared spectroscopy (FTIR), quadrupole mass spectrometry (QMS), and optical emission spectroscopy (OES). *Ex situ*: Rutherford backscattering spectroscopy (RBS), x-ray reflectometry (XRR), x-ray photoelectron spectroscopy (XPS), atomic force microscopy (AFM), transmission electron microscopy (TEM), elastic recoil detection (ERD), x-ray diffraction (XRD), and four-point probe (FPP) analysis.

Aspects of ALD growth	<i>in situ</i>	<i>ex situ</i>
Film thickness		
Growth rate	SE	XRR
Film nucleation	SE, FTIR	XPS, RBS
Roughness	SE	AFM, TEM
Interface formation	SE, FTIR	XPS, RBS, TEM
Film composition		
Stoichiometry		RBS
Impurity content	FTIR	RBS, ERD
Mass density		RBS, XRR
Chemical bonding	FTIR	XPS
Microstructure		
Crystal phase	SE	XRD, TEM
Grain size		XRD, TEM
Electrical properties		
Resistivity	SE	FPP
Electron mean free path	SE	
Electron density	SE	
Reaction mechanism of ALD		
Gas phase reaction by-products	QMS, OES	
Surface groups	FTIR, SE	

B Plasma-assisted ALD of conductive TaN_x films

Conductive tantalum nitride (TaN_x) films are actively researched for application as metal electrodes in, among others, CMOS transistors and high-density capacitors, and for application as Cu diffusion barrier in Ta/TaN liner materials for advanced metallization in interconnect technology. In line with the ongoing miniaturization, ALD processes of conductive TaN_x are developed to replace the conventional deposition methods currently employed. Tantalum nitride exists, however, in various crystal phases with different material properties that range from conductive, cubic TaN to semiconductive Ta₃N₅ [38]. In thermal ALD processes using metal-halide or metal-organic Ta precursors in combination with NH₃ [39–42], semiconductive Ta₃N₅ films were deposited because the reducing power of NH₃ was insufficient to change the oxidation state of the Ta atom (state +5 in most ALD precursors) to state +3 in the conductive TaN film. The challenge is, therefore, to supply more reactivity to the ALD process in order to have sufficient reducing power to deposit conductive (cubic) TaN_x films.

Using the strong reducing power of a H₂ plasma, it was already demonstrated that conductive, low-resistivity TaN_x films can be deposited by means of plasma-assisted ALD [42–45]. In this work, the opportunities for the plasma-assisted ALD process to tailor the TaN_x film properties were extensively addressed by examining the influence of plasma exposure time and plasma gas composition on the material properties obtained. Moreover, monitoring the film growth by *in situ* spectroscopic ellipsometry (SE) is an excellent approach to distinguish the different TaN_x phases that can be deposited under various ALD growth conditions. Figure 6 illustrates the sensitivity of the optical dielectric function ϵ_2 to changes in TaN_x film composition. A clear transition from a metallic film to a band gap material is observed in the dielectric function while changing the H₂ plasma exposure time and admixing N₂ to the H₂ plasma gas or by using an NH₃ plasma.

In particular for the conductive films, the Drude absorption by free conduction electrons in the film is observed in the infrared part of the photon spectrum.⁵ From the magnitude of the Drude absorption in the dielectric function ϵ_2 in Fig. 6, it is immediately clear that the conductive properties of the TaN_x improved with increasing H₂ plasma exposure time.

⁵In the current work, an ellipsometer system with a photon energy range extended down to the near-infrared (0.75–5.0 eV) has been used. Due to this near-infrared extension, the Drude absorption can be probed to a larger extent compared to commonly applied visible-range ellipsometers (typically, 1.25–5.0 eV).

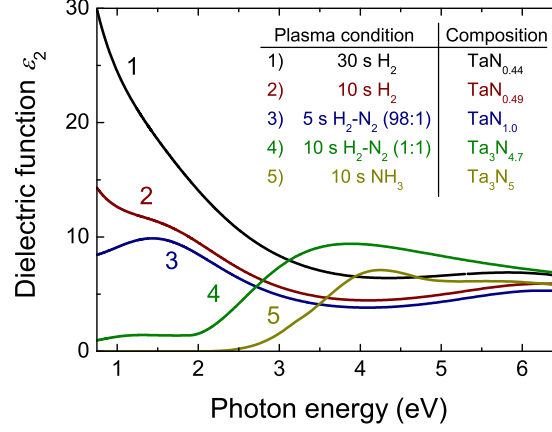


Figure 6: The change from conductive TaN_x [films 1–3] to semiconductive Ta₃N₅-like [films 4 and 5] films with variation of plasma exposure time and plasma gas composition in the ALD cycle can be observed from the shape of the dielectric function ϵ_2 as determined by *in situ* spectroscopic ellipsometry. For the conductive TaN_x films, the increasing magnitude of the Drude absorption with H₂ plasma exposure time (as observed in the infrared part of the photon spectrum), is a direct indication of the improved electrical properties of the TaN_x film obtained. The inset shows the film composition as determined by Rutherford backscattering spectroscopy to further illustrate the change in TaN_x composition with plasma condition.

Subsequently by parametrization of the Drude absorption, electrical film properties, such as electrical resistivity, can be derived from the optical dielectric function *during* the ALD process.

In summary, the plasma-assisted ALD process provides a large freedom in tailoring the material properties of the deposited TaN_x films. The conductive TaN_x film properties obtained in this work, i.e., a low-resistivity (380 $\mu\Omega$ cm), a high mass-density (12.1 g cm⁻³), and a cubic microstructure, are among the best results reported in the literature [43, 45]. These results demonstrate the strong reducing power of the H₂ plasma and the ability to control and tune the film properties by changing the plasma conditions in plasma-assisted ALD processes.

C Plasma-assisted ALD of Al₂O₃ at low deposition temperatures

Thin Al₂O₃ ALD films are researched for water and oxygen permeation barriers required for encapsulation in food packaging, electrochromics, pho-

to voltaics, and, ultimately, (flexible) electronic displays. The basis for ALD films to serve as ultrathin permeation barriers is evident. The ALD Al_2O_3 films typically have a relatively high mass density, low impurity content, and the amorphous films are considered (virtually) pinhole-free. The ALD growth is conformal and is expected to coat small defects or dust particles inevitably present on the device surface during industrial processing.⁶ In addition, for the encapsulation of temperature-sensitive organic substrates or devices, low temperature deposition is essential and, in fact, room temperature deposition process is preferred for process simplicity and compatibility issues.

The thermal ALD process of Al_2O_3 has been demonstrated to allow for film growth at substrate temperatures down to room temperature [29], however, with the notion that it becomes difficult to achieve saturation of the second half-reaction when dosing H_2O at relatively low temperatures ($<100^\circ\text{C}$) [20, 46]. Low temperature thermal ALD of Al_2O_3 requires also an extensive purge time to remove the excess of H_2O vapor from the reactor after the second half-cycle (e.g., 180 s at 33°C [29]). In this respect, the use of the O_2 plasma has practical advantages over the use of H_2O , since the purge time after the O_2 plasma can be short (<1 s) and independent of deposition temperature.

In this section, the development of the plasma-assisted ALD Al_2O_3 process and the understanding of the material properties obtained at low temperature deposition will be discussed. Moreover, the industrial feasibility of the plasma-assisted ALD technique for deposition of high-quality Al_2O_3 barriers on an operational device will be demonstrated.

1 Plasma-assisted ALD of Al_2O_3 at $25\text{--}150^\circ\text{C}$

The plasma-assisted ALD process of Al_2O_3 from $\text{Al}(\text{CH}_3)_3$ precursor and a remote O_2 plasma has been developed for depositions in the range from 25°C to 400°C [18, 20, 47]. In particular the film properties obtained for depositions below 150°C have been studied in this work. The influence of deposition temperature on the material properties obtained can be addressed in detail by elucidating the fundamental reaction mechanism governing the ALD process. The surface species that were produced during the plasma-assisted ALD process of Al_2O_3 were detected by transmission infrared spectroscopy (as will be discussed in Chapter 4), while the volatile

⁶Especially for the barrier deposition by conventional methods, the surface defects are considered critical centers for pinhole formation in the barrier film as caused by the non-perfect growth conformality of these techniques in coating/sealing the defects.

reaction by-products were determined by real-time mass spectrometry and optical emission spectroscopy [17, 18, 37].

It was established that the surface reactions of the plasma-assisted ALD process proceed via the formation of $-\text{CH}_3$ surface groups and CH_4 volatile by-products upon $\text{Al}(\text{CH}_3)_3$ precursor adsorption. During the O_2 plasma half-reaction, these $-\text{CH}_3$ groups are “burnt” off in a combustion-like reaction with the plasma species leading to $-\text{OH}$ surface groups and CO_2 and H_2O reaction by-products. Also at room temperature, the surface chemistry of plasma-assisted ALD is ruled by these $-\text{CH}_3$ and $-\text{OH}$ groups, where it is noted that the amount of $-\text{OH}$ surface groups involved in the ALD chemistry strongly increased for lower deposition temperatures. This observation accounts for the increase in growth per cycle when going to lower temperatures as reported for plasma-assisted ALD of Al_2O_3 [19, 20, 47], because more precursor molecules can adsorb due to the higher density of $-\text{OH}$ adsorption sites at lower temperatures.

With reducing temperatures, the transmission spectra showed that an increased amount of OH and C-related impurities were incorporated in the Al_2O_3 film, i.e., at 25 °C: $[\text{O}]/[\text{Al}] = 2.1$, ~ 5 at. % C, and ~ 17 at. % H as determined by Rutherford backscattering spectroscopy and elastic recoil detection. The presence of these impurities is an indication that the surface reactions are in fact not fully saturated for the ALD conditions employed (25 ms $\text{Al}(\text{CH}_3)_3$ and 2 s O_2 plasma), especially at 25 °C deposition. This view was supported by the fact that doubling the plasma exposure time could be used to effectively improve the film quality, as was observed by the reduction of OH and C-related impurities by transmission infrared spectroscopy and by the compositional data (at 25 °C: $[\text{O}]/[\text{Al}] = 1.8$, < 2 at. % C, and ~ 14 at. % H). Most likely, the film properties can be further improved by fine-tuning of the O_2 plasma exposure time in the ALD cycle.

These results demonstrate the ability of plasma-assisted ALD to deposit dense Al_2O_3 films down to room temperature. For higher deposition temperatures (> 150 °C), the film properties obtained by plasma-assisted ALD are very similar to those obtained by thermal ALD [20]. The benefits of plasma-assisted ALD are, however, evident at lower temperature deposition, i.e., a higher growth rate, higher mass density, and lower impurity content.

2 Moisture permeation barrier properties of Al_2O_3 films

The ALD Al_2O_3 films deposited at low temperature (< 100 °C) are researched for the encapsulation of (flexible) organic light emitting diodes

(OLEDs). Stringent demands are put on the barrier quality to minimize water and oxygen uptake in order to guarantee an OLED device lifetime of >10 years, i.e., the barrier should yield an extremely low water vapor transmission rate (WVTR) of $<10^{-6} \text{ g m}^{-2} \text{ day}^{-1}$.

The barrier quality of the plasma-assisted ALD Al_2O_3 films was studied for different deposition temperatures (25–100 °C) and for different film thicknesses (10–40 nm) on poly(2,6-ethylene naphthalate) (PEN) polymeric substrates, as described in Chapter 3. Surprisingly, the best barrier quality of $5 \times 10^{-3} \text{ g m}^{-2} \text{ day}^{-1}$ was obtained for the deposition at room temperature, despite the fact that the film contained relatively the highest amount of impurities. The reason for the barrier improvement with lower deposition temperature still has to be resolved. Due to the high polarizability of the Al-OH bond [48], the hydroxyl impurities in the film might obstruct water permeation through the film and, thus, can be beneficial to the barrier properties. On the other hand, some stress formation can also occur upon cooling down the Al_2O_3 films deposited at temperatures $>25 \text{ °C}$ and that can also slightly deteriorate the barrier quality that is measured at room temperature.

The barrier properties of the plasma-assisted ALD Al_2O_3 films are excellent in comparison to those of thicker films deposited by plasma-enhanced chemical vapor deposition (PECVD), as shown in Fig. 7. Also Al_2O_3 films deposited by thermal ALD yield excellent permeation barrier properties. Groner *et al.* reported good permeation barrier properties of $\sim 1 \times 10^{-3} \text{ g m}^{-2} \text{ day}^{-1}$ of very thin (10–25 nm) Al_2O_3 films deposited at 120 °C [49]. More recently, an excellent barrier quality of $\sim 10^{-5} \text{ g m}^{-2} \text{ day}^{-1}$ was reported for a 20 nm thick thermal ALD Al_2O_3 film deposited at 38 °C [50], but that required most likely careful substrate cleaning and handling to minimize the amount of particles on the surface.

The industrial compatibility of the plasma-assisted ALD process for encapsulation of polymer light-emitting diode (PLED) devices is demonstrated in Fig. 8, where the Al_2O_3 barriers were deposited on a real device. For this purpose, the encapsulation by the Al_2O_3 films is compared to the encapsulation obtained by a PECVD SiN_x film. The encapsulation by this SiN_x film drastically increased the life-time of the PLED device, although the formation of black spots was still observed due the presence of pin-holes in the film that facilitate water and oxygen diffusion through the film [Fig. 8(b)]. In this respect, the encapsulation by the ALD Al_2O_3 film was more effective and resulted in a reduction of the number of black spots formed [Fig. 8(c)]. This illustrates that the conformal ALD film has prob-

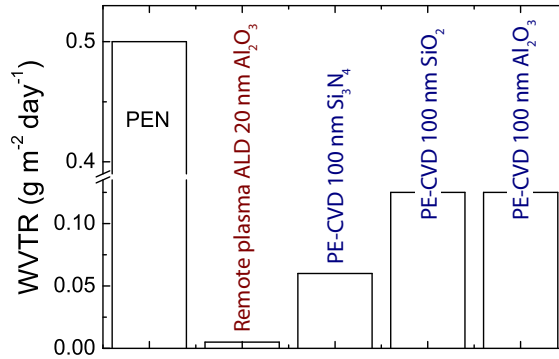


Figure 7: Barrier properties of the plasma-assisted ALD Al₂O₃ films compared to typical barrier films deposited by plasma-enhanced chemical vapor deposition (PECVD). The water vapor transmission rate (WVTR) through the barrier coating was quantified by means of the calcium test in a controlled environment (21°C and 60% relative humidity). Note the difference in film thickness of the ALD and PECVD films that further expresses the quality of the barriers deposited by ALD. For reference the WVTR of the uncoated PEN polymeric substrate is also shown (note the break present in the WVTR scale).

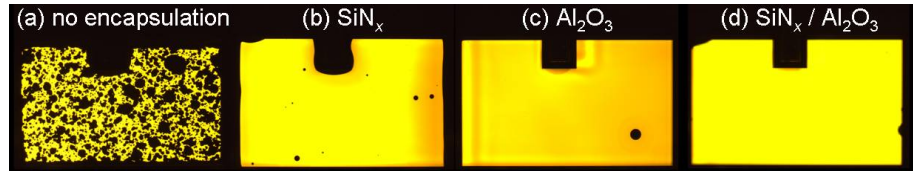


Figure 8: Life-time test of polymer light-emitting diodes (PLEDs) encapsulated with different barrier films, i.e., 300 nm SiN_x deposited by PECVD at 110°C and 40 nm Al₂O₃ deposited by plasma-assisted ALD at 25°C. Electroluminescence of encapsulated working PLED devices: (a) no encapsulation [168 h], (b) SiN_x [504 h] (c) ALD Al₂O₃ [504 h], and (d) SiN_x/ALD Al₂O₃ [2235 h]. The different durations of the shelf test measurements at 20°C and 50% relative humidity are indicated in between the brackets and shows the improved device operation after encapsulation. The black spot formation in the PLED device is caused by local diffusion of water and oxygen through the pinholes in the barrier resulting in a fast oxidation of the electrode at that position. The dramatic decrease in number of black spots as a result of encapsulation is evident and the number of black spots observed in the ALD-encapsulated devices is the lowest. The research was conducted in collaboration with Philips Research Eindhoven.

ably sealed more surface defects/particles than the SiN_x film. The combination of the growth conformality of ALD Al_2O_3 and the intrinsic barrier quality of the SiN_x film resulted in a further improvement of the barrier properties [Fig. 8(d)]. Currently, different combinations and configurations of ALD and PECVD films are, therefore, researched in collaboration with Philips Research Eindhoven to meet the stringent requirements imposed by encapsulation applications.

D Fundamentals of ALD reaction mechanisms

A fundamental understanding of the ALD reaction mechanism aids substantially in the optimization and further development of the processes involved. As evident from the previous section, the Al_2O_3 material properties obtained at lower temperatures were better understood by establishing its reaction mechanism. In this section, the reducing power of the H_2 in the plasma-assisted ALD process of conductive TaN_x films and the initial film nucleation of thermal ALD La_2O_3 films will be examined by detection of the volatile reaction by-products and by monitoring the surface groups, respectively.

1 Reducing power of the H_2 plasma

Fundamental insight into the reducing power of the H_2 plasma during the plasma-assisted ALD process of conductive TaN_x films (as discussed in Sec. IV B) can be obtained by detecting the volatile reaction by-products created during the plasma step, as done by mass spectrometry and optical emission spectroscopy.

The cracking patterns as obtained by mass spectrometry during the $\text{Ta}[\text{N}(\text{CH}_3)_2]_5$ precursor and H_2 plasma step are shown in Fig. 9. During the precursor half-reaction [Fig. 9(a)], predominantly the formation of $\text{HN}(\text{CH}_3)_2$ reaction by-products was observed. This indicates that the $\text{Ta}[\text{N}(\text{CH}_3)_2]_5$ precursor splits off ligands upon adsorption on H-containing surface groups, e.g., $-\text{NH}_x$, and probably $-\text{Ta}[\text{N}(\text{CH}_3)_2]_x$ surface species are formed. Considering the nature of this adsorption reaction, no reduction of the Ta-atom is expected during this ALD half-cycle. This view is supported by the fact that in thermal ALD processes using the same metal-organic precursor in combination with NH_3 only semiconductive Ta_3N_5 films were deposited.

During the H_2 plasma exposure step as shown in Fig. 9(b), the formation of $\text{HN}(\text{CH}_3)_2$, HCN , C_2H_2 , and CH_4 reaction by-products was

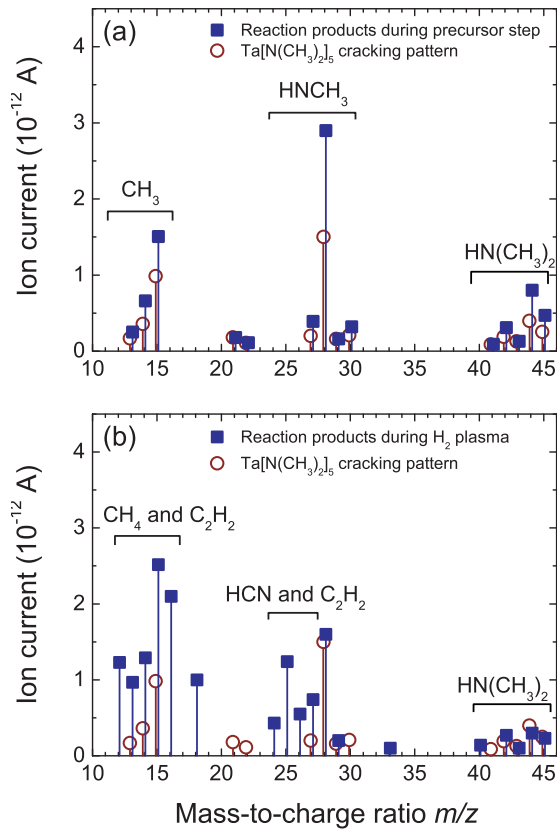


Figure 9: The cracking patterns obtained by mass spectrometry during (a) the $\text{Ta}[\text{N}(\text{CH}_3)_2]_5$ precursor and (b) H_2 plasma half-reactions of plasma-assisted ALD of conductive TaN_x films. By comparing these cracking patterns to the cracking pattern of the precursor [shown in (a) and (b)] and the H_2 plasma [only $m/z \leq 2$ (not shown)], the reaction by-products can be deduced. (a) $\text{HN}(\text{CH}_3)_2$ molecules (being the parent molecule for the HNCH_3^+ and CH_3^+ fragments) are the dominant reaction by-products upon $\text{Ta}[\text{N}(\text{CH}_3)_2]_5$ adsorption. (b) $\text{HN}(\text{CH}_3)_2$, HCN , C_2H_2 , and CH_4 reaction by-products are formed in the H_2 plasma step, where the assignment of the $\text{HN}(\text{CH}_3)_2$ molecules is again clear from the cracking pattern of the precursor, which is shown as reference.

observed. The formation of the large $\text{HN}(\text{CH}_3)_2$ molecule is a direct evidence of the ability of the H_2 plasma species to break the Ta–N bond of the adsorbed precursor. This is further substantiated by examination of the plasma emission spectrum during the ALD half-cycle by optical emission spectroscopy. The emission spectra revealed the presence of excited $\text{C}\equiv\text{N}$ radicals in the plasma. This is another indication that the Ta–N bond of the adsorbed precursor molecule is broken by the H_2 plasma species. In turn, the breaking of the Ta–N bond is essential to reduce the oxidation state of the Ta atom in order to deposit the conductive TaN_x films.

The mechanism for the formation of the $\text{C}\equiv\text{N}$ radicals and the additional HCN, C_2H_2 , and CH_4 reaction by-products [Fig. 9(b)] still has to be resolved. These species can be formed either at the surface as a part of the stepwise removal of the precursor ligands by the plasma species, or by reaction of the $\text{HN}(\text{CH}_3)_2$ (or another species containing a C–N bond) in the plasma. To completely resolve the reaction mechanism of this plasma-assisted ALD process, the surface groups formed in the ALD process have to be determined, for example, by transmission infrared spectroscopy measurements.

Additional insight into the ALD reaction mechanism can be obtained by monitoring the amount of reaction by-products in real time during the ALD process. First, it was observed that the $\text{C}\equiv\text{N}$ radicals and the $\text{HN}(\text{CH}_3)_2$ and HCN molecules are only created during the first 5 s of H_2 plasma operation, which is an indication of the saturation of the ALD surface reactions. Remarkably, the formation of CH_4 molecules was still observed after 40 s of H_2 plasma exposure. This indicated an increased removal of C impurities from TaN_x film with increasing plasma exposure. In line with the results in Sec. IV B, it can be concluded that the H_2 plasma continues to interact with the TaN_x film even after completing the plasma-assisted ALD surface reactions. This is supported by the fact that the TaN_x film properties can be improved and tuned by varying the plasma exposure time, as was shown in Fig. 6.

2 Nucleation behavior of ALD La_2O_3

For the research and development of new (ultra) high- k dielectrics, the nucleation behavior and possible formation of an interfacial layer between film and substrate are important aspects of study [3]. Especially for the gate oxide in CMOS transistors, the nanometer thick high- k dielectrics should nucleate easily (resulting in a fast film closure) when deposited on top of the crystalline silicon channel of the transistor. Moreover, the

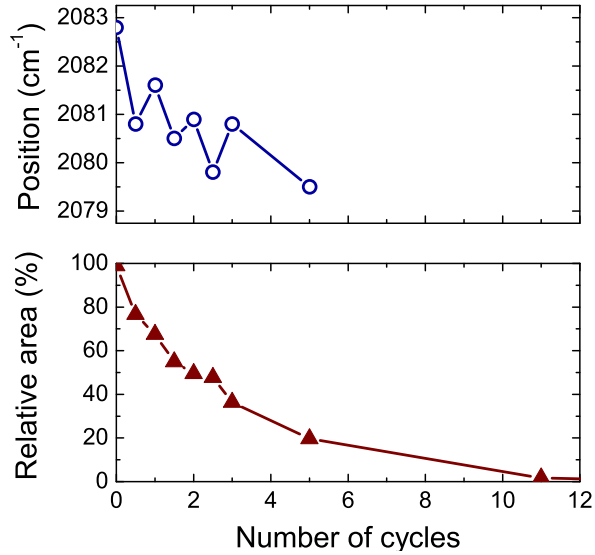


Figure 10: Peak position and relative peak area of the Si–H surface peak during nucleation of thermal ALD La_2O_3 films on H-terminated Si(111) as deduced from transmission infrared spectroscopy measurements. The ALD half-cycles of the $\text{La}(\text{}^i\text{PrAMD})_3$ precursor adsorption and the D_2O oxidation are represented by half-integer and full-integer data points, respectively. The nucleation of the La_2O_3 film is most evident by the decrease in area and position of the Si–H peak with increasing number of cycles. The slight increase in peak position after every D_2O dosing can be attributed to the formation of a SiO_2 interfacial layer.

formation of a silicon oxide layer in between the high- k dielectric and the Si channel should be avoided or, if impossible, be well-controlled. In this section, *in situ* transmission infrared spectroscopy was used to study the nucleation behavior of La_2O_3 (with dielectric constant $k = 27$) on H-terminated Si(111) substrates, which are assumed representative for the surface of the Si channel in CMOS transistors.

The La_2O_3 films were deposited by a thermal ALD process at 200°C using $\text{La}(\text{}^i\text{PrAMD})_3$ precursor [51, 52] and D_2O as oxidant source.⁷ In order for the La_2O_3 film to nucleate on the H-terminated Si(111) surface,

⁷The ALD chemistry using D_2O can be assumed identical to the chemistry using H_2O oxidant source. The use of D_2O has, however, a practical advantage in infrared spectroscopy since its absorbance occurs in a different wavenumber range than H_2O . As a consequence, D_2O -related absorbances related to the ALD process can easily be distinguished from H_2O fluctuations in the (purged) experimental environment.

the precursor has to adsorb on the Si–H surface groups that are initially present. Therefore, by monitoring the peak position and peak area of the Si–H surface group with number of ALD cycles, the film nucleation behavior of this thermal ALD process can be addressed, as shown in Fig. 10. From the decrease in Si–H peak area with number of cycles, it can be concluded that during the $\text{La}({}^i\text{PrAMD})_3$ precursor and the D_2O dosing, the Si–H peaks are slowly removed and are completely removed after 11 ALD cycles. A similar effect can be observed by monitoring the Si–H peak position with number of cycles. First, it is observed that overall the peak position shifts to lower wavenumbers with increasing number of ALD cycles. This indicates that the (remaining) Si–H peaks become more isolated on the surface [53]. Interestingly, the peak position shifts to slightly higher wavenumbers after each D_2O half-cycle (Fig. 10). Combining this observation with the decrease in peak area during the D_2O dosing, it can be concluded that the D_2O also reacts with Si–H resulting in the formation of Si–O–Si backbonds, which causes the Si–H peak to shift to higher wavenumber [53].

From the *in situ* transmission infrared study, it can be concluded that the nucleation of the La_2O_3 films is relatively fast indicating that the $\text{La}({}^i\text{PrAMD})_3$ precursor readily reacts with the H-terminated Si(111) surface. The formation of an interfacial oxide layer is observed, however, further analysis is required to quantify thickness and properties of this layer.

V Outlook

The research on ALD has been vastly expanding in the last few years and the industrial integration of well-established ALD materials in industrial devices is currently taking place. The plasma-assisted ALD process is in this respect complementing the portfolio of ALD processes in providing specific growth benefits delivered by supplying plasma reactivity to the process. This work demonstrated the ability of plasma-assisted ALD in obtaining high quality films at low deposition temperatures and in tailoring the film properties by controlling the plasma condition. The feasibility of the plasma-assisted ALD processes has been shown by the deposition of excellent Al_2O_3 based moisture permeation barrier films for the encapsulation of OLEDs. These plasma-assisted ALD Al_2O_3 films also yield an excellent level of surface passivation on *c*-Si solar cells in order to increase the solar cell efficiency [54–56]. The conductive TiN and TaN_x ALD

films show promising results as Cu diffusion barrier layer in through-silicon vias for system-in-package applications and as Li diffusion barrier in new battery concepts [57].

The strength of *in situ* monitoring the ALD process was highlighted for various diagnostic studies throughout this work and the approach chosen is exemplary for the use of other techniques during ALD in general. By acquiring data in between the ALD cycles, detailed insight into various aspects of the ALD growth process of various materials was obtained, such as film nucleation behavior and size effects in thin conductive films. Fundamental insight into the influence of thickness on the material properties of these nanometer thick films are of key interest considering the continuous miniaturization and increased demands on thickness and properties of the ALD films. Moreover, the *in situ* diagnostics were used to elucidate the reaction mechanisms governing the plasma-assisted ALD of metal oxides and metal nitrides. The combustionlike surface reactions by the O₂ plasma species and the reducing power of the H₂ plasma which were demonstrated in this work, are expected to have generic implications for similar plasma-assisted ALD processes using metal-organic precursors.

Spectroscopic ellipsometry was shown to be very versatile to study various aspects related to the ALD film growth. This optical diagnostic is particularly valuable for integration on *research* ALD reactors in order to study and design new ALD processes and materials. This aspect was recognized and has recently led to the development of commercial ALD reactors equipped with ellipsometers, such as the FlexALTM and OpALTM systems of Oxford Instruments Plasma Technology [33]. On the other hand, mass spectrometry and optical emission spectroscopy can be considered well-suited for use in an industrial environment. The adaptation of the reactor is relatively straightforward and these techniques provide the opportunity to monitor and control the ALD process on an industrial reactors.

The ALD processes and materials studied are becoming increasingly complex considering the stringent demands on the film properties. Novel electrode materials and ultra high-*k* dielectrics are necessary and this requires the synthesis of novel precursor molecules, which contain other classes of elements of the Periodic Table (e.g., the transition metals and rare-earth elements) and more diverse ligands. The knowledge obtained on the reaction mechanisms of plasma-assisted ALD can be used to synthesize novel precursor molecules specifically designated for the use in a plasma-based process. These kinds of precursor molecules for plasma-assisted ALD can have their specific merits in terms of volatility, reactivity, and stabil-

ity over the equivalent molecules used for other (thermal) ALD processes. In addition, a plasma can also be used to functionalize the substrate in order to make its surface more reactive to the precursor molecules and to facilitate the nucleation and closure of the ALD film. Especially for complex materials, it is expected that the additional reactivity provided by plasma-assisted ALD is key to facilitate the chemistry at relatively low temperatures while having the ability to control the film properties obtained.

Bibliography

- [1] International Technology Roadmap for Semiconductors, 2007 (<http://public.itrs.net>).
- [2] A. I. Kingon, J.-P. Maria, and S. K. Streiffer, *Nature* **406**, 1032 (2000).
- [3] G. D. Wilk, R. M. Wallace, and J. M. Anthony, *J. Appl. Phys.* **89**, 5243 (2001).
- [4] T. Suntola, *Mater. Sci. Rep.* **4**, 261 (1989).
- [5] M. Ritala and M. Leskelä, *Handbook of Thin Film Materials*, volume 1, Academic, San Diego, CA (2001).
- [6] M. Leskelä and M. Ritala, *Thin Solid Films* **409**, 138 (2002).
- [7] R. L. Puurunen, *J. Appl. Phys.* **97**, 121301 (2005).
- [8] S. M. George, A. W. Ott, and J. W. Klaus, *J. Phys. Chem.* **100**, 13121 (1996).
- [9] H. Kim, *J. Vac. Sci. Technol. B* **21**, 2231 (2003).
- [10] K.-E. Elers, T. Blomberg, M. Peussa, B. Aitchison, S. Haukka, and S. Marcus, *Chem. Vap. Dep.* **12**, 13 (2006).
- [11] Y. Du and S. M. George, *J. Phys. Chem. C* **111**, 8509 (2007).
- [12] *Micro Magazine*, July 2005 (<http://micromagazine.fabtech.org>).
- [13] *Solid State Technology*, March 2007 (<http://sst.pennnet.com>).
- [14] S. D. Elliot, G. Scarel, C. Wiemer, M. Fanciulli, and G. Pavia, *Chem. Mater.* **18**, 3764 (2006).
- [15] S.-C. Ha, E. Choi, S.-H. Kim, and J. S. Roh, *Thin Solid Films* **476**, 252 (2005).
- [16] S. D. Elliot and J. C. Greer, *J. Mater. Chem.* **14**, 3246 (2004).
- [17] S. B. S. Heil, P. Kudlacek, E. Langereis, R. Engeln, M. C. M. van de Sanden, and W. M. M. Kessels, *Appl. Phys. Lett.* **89**, 131505 (2006).

- [18] S. B. S. Heil, *Plasma-assisted Atomic Layer Deposition of Metal Oxides and Nitrides*, PhD thesis, Eindhoven University of Technology, Eindhoven (2007).
- [19] E. Langereis, M. Creatore, S. B. S. Heil, M. C. M. van de Sanden, and W. M. M. Kessels, *Appl. Phys. Lett.* **89**, 081915 (2006).
- [20] J. L. van Hemmen, S. B. S. Heil, J. H. Klootwijk, F. Roozeboom, C. J. Hodson, M. C. M. van de Sanden, and W. M. M. Kessels, *J. Electrochem. Soc.* **154**, G165 (2007).
- [21] M. de Keijser and C. van Opdorp, *Appl. Phys. Lett.* **58**, 1187 (1990).
- [22] S. M. Rossnagel, A. Sherman, and F. Turner, *J. Vac. Sci. Technol. B* **18**, 2016 (2000).
- [23] H. Kim and S. M. Rossnagel, *J. Vac. Sci. Technol. A* **20**, 802 (2002).
- [24] A. C. Dillon, A. W. Ott, J. D. Way, and S. M. George, *Surf. Sci.* **322**, 230 (1995).
- [25] S. Haukka, E.-L. Lakomaa, and A. Root, *J. Phys. Chem.* **97**, 5085 (1993).
- [26] M. D. Halls, K. Raghavachari, M. M. Frank, and Y. J. Chabal, *Phys. Rev. B* **68**, 161302 (2003).
- [27] M. M. Frank, Y. J. Chabal, and G. D. Wilk, *Appl. Phys. Lett.* **82**, 4758 (2003).
- [28] A. Rahtu, T. Alaranta, and M. Ritala, *Langmuir* **17**, 6506 (2001).
- [29] M. D. Groner, F. H. Fabreguette, J. W. Elam, and S. M. George, *Chem. Mater.* **16**, 639 (2004).
- [30] J. W. Elam, M. Schuisky, J. D. Ferguson, and S. M. George, *Thin Solid Films* **436**, 145 (2003).
- [31] H. Tiznado and F. Zaera, *J. Phys. Chem. B* **110**, 13491 (2006).
- [32] R. Matero, A. Rahtu, and M. Ritala, *Langmuir* **21**, 3498 (2005).
- [33] Oxford Instruments Plasma Technology, North End, Yatton BS49 4AP, United Kingdom (<http://www.oxford-instruments.com>).

- [34] H. G. Tompkins and E. A. Irene, *Handbook of Ellipsometry*, William Andrews, Inc., New York (2005).
- [35] H. Fujiwara, *Spectroscopic Ellipsometry: Principles and Applications*, John Wiley & Sons, Ltd., West Sussex, England (2007).
- [36] J. W. Klaus, A. W. Ott, J. M. Johnson, and S. M. George, *Appl. Phys. Lett.* **70**, 1092 (1997).
- [37] S. B. S. Heil, J. L. van Hemmen, M. C. M. van de Sanden, and W. M. M. Kessels, *J. Appl. Phys.* **103**, 103302 (2008).
- [38] C. Stampfl and A. J. Freeman, *Phys. Rev. B* **71**, 024111 (2005).
- [39] M. Ritala, P. Kalsi, D. Riihelä, K. Kukli, M. Leskelä, and J. Jokinen, *Chem. Mater.* **11**, 1712 (1999).
- [40] Y. Travaly, J. Schuhmacher, A. M. Hoyas, M. V. Hove, K. Maex, T. Abell, V. Sutcliffe, and A. M. Jonas, *J. Appl. Phys.* **97**, 84316 (2005).
- [41] R. Sreenivasan, T. Sugawara, K. C. Saraswat, and P. C. McIntrye, *Appl. Phys. Lett.* **90**, 102101 (2007).
- [42] W. J. Maeng, S.-J. Park, and H. Kim, *J. Vac. Sci. Technol. B* **24**, 2276 (2006).
- [43] H. Kim, C. Detavenier, O. van der Straten, S. M. Rossnagel, A. J. Kellock, and D.-G. Park, *J. Appl. Phys.* **98**, 014308 (2005).
- [44] J.-S. Park, M. J. Lee, C. S. Lee, and S.-W. Kang, *Electrochem. Solid-State Lett.* **4**, C17 (2001).
- [45] J.-S. Park, H.-S. Park, and S.-W. Kang, *J. Electrochem. Soc.* **149**, C28 (2002).
- [46] R. Matero, A. Rahtu, M. Ritala, M. Leskelä, and T. Sajavaara, *Thin Solid Films* **368**, 1 (2000).
- [47] E. Langereis, J. Keijmel, M. C. M. van de Sanden, and W. M. M. Kessels, *Appl. Phys. Lett.* **92**, 231904 (2008).
- [48] W. H. Koo, S. M. Jeong, S. H. Choi, W. J. Kim, H. K. Baik, S. M. Lee, and S. J. Lee, *J. Phys. Chem. B* **109**, 11354 (2005).

-
- [49] M. D. Groner, S. M. George, R. S. McLean, and F. Carcia, Appl. Phys. Lett. **88**, 051907 (2006).
- [50] P. F. Carcia, R. S. McLean, M. H. Reilly, M. D. Groner, and S. M. George, Appl. Phys. Lett. **89**, 031915 (2006).
- [51] B. S. Lim, A. Rahtu, P. de Rouffignac, and R. G. Gordon, Appl. Phys. Lett. **84**, 3957 (2004).
- [52] B. S. Lim, A. Rahtu, and R. G. Gordon, Nat. Mater. **2**, 749 (2003).
- [53] X. Zhang, Y. J. Chabal, S. B. Christman, E. E. Chaban, and E. Garfunkel, J. Vac. Sci. Technol. A **19**, 1725 (2001).
- [54] B. Hoex, S. B. S. Heil, E. Langereis, M. C. M. van de Sanden, and W. M. M. Kessels, Appl. Phys. Lett. **89**, 042112 (2006).
- [55] B. Hoex, J. Schmidt, R. Bock, P. P. Altermatt, M. C. M. van de Sanden, and W. M. M. Kessels, Appl. Phys. Lett. **91**, 112107 (2007).
- [56] B. Hoex, *Functional Thin Films for High-Efficiency Solar Cells*, PhD thesis, Eindhoven University of Technology, Eindhoven (2008).
- [57] H. C. M. Knoop, L. Baggetto, E. Langereis, M. C. M. van de Sanden, J. H. Klootwijk, F. Roozeboom, R. A. H. Niessen, P. H. L. Notten, and W. M. M. Kessels, ECS Transactions **11**, 45 (2007).

Part B

Publications

Chapter 1

In situ spectroscopic ellipsometry study on the growth of ultrathin TiN films by plasma-assisted atomic layer deposition*

Abstract

The growth of ultrathin TiN films by plasma-assisted atomic layer deposition (ALD) was studied by *in situ* spectroscopic ellipsometry (SE). In between the growth cycles consisting of TiCl₄ precursor dosing and H₂-N₂ plasma exposure, ellipsometry data was acquired in the photon energy range of 0.75 to 5.0 eV. The dielectric function of the TiN films was modeled by a Drude-Lorentz oscillator parameterization, and the film thickness and the TiN material properties, such as conduction electron density, electron mean free path, electrical resistivity, and mass density, were determined. *Ex situ* analysis was used to validate the results obtained by *in situ* SE. From the *in situ* spectroscopic ellipsometry data several aspects related to thin film growth by ALD were addressed. A decrease in film resistivity with deposition temperatures between 100 and 400 °C was attributed to the increase in electron mean free path due to a lower level of impurities incorporated into the films at higher temperatures. A change in resistivity and electron mean free path was observed as a function of film thickness (2–65 nm) and was related to an increase in electron-sidewall scattering for decreasing film thickness. The TiN film nucleation was studied on thermal

*Published as: E. Langereis, S. B. S. Heil, M. C. M. van de Sanden, and W. M. M. Kessels, *J. Appl. Phys.* **100**, 023534 (2006).

oxide covered *c*-Si substrates. A difference in nucleation delay was observed on these substrates and was related to the varying surface hydroxyl density. For plasma-assisted ALD on H-terminated *c*-Si substrates, the formation of an interfacial SiN_{*x*} film was observed, which facilitated the TiN film nucleation.

I Introduction

Atomic layer deposition (ALD) has recently gained a lot of interest in research and development due to its intrinsic growth control by the virtue of self-limited surface reactions [1–4]. The characteristic layer-by-layer growth, excellent uniformity, and ultimate conformality in high-aspect ratio features, make ALD a promising technique to deposit ultrathin films in integrated circuits [1]. In the literature, many ALD schemes are reported to achieve layer-by-layer growth of a large variety of materials [2, 4]. In addition, the plasma-assisted ALD technique is believed to offer the same advantages as ALD as well as a larger freedom in materials and processes, improved material quality, and lower deposition temperature [5–7].

When reducing the film dimensions towards the nanometer scale, detailed insight into aspects such as finite size effects, film nucleation, and interface formation/modification becomes essential [8–11]. Therefore, successful application of ultrathin films in devices has to be accompanied by accurate metrology techniques to determine the properties of these thin films. The films are mostly studied by *ex situ* diagnostics giving detailed insight into the thin film properties, however, at the cost of time-consuming and often sample-destructive procedures. For example, Satta *et al.* reported on the ALD film growth process using elaborate Rutherford backscattering spectroscopy [9], but the analysis required separate samples for each condition and film thickness that was examined. Furthermore, for materials that are air-sensitive, an *ex situ* measurement could result in different material properties due to the exposure of the films to the ambient.

A detailed understanding of the growth process and material properties of the ultrathin films can be obtained by the application of *in situ* diagnostics. In the literature, several *in situ* studies on ALD-deposited thin films have been reported using diagnostics such as quartz crystal microbalance [12, 13], x-ray diffraction [14], and infrared spectroscopy [15, 16]. In this paper, we will present an *in situ* study of ALD thin film growth using the optical, non-intrusive technique of spectroscopic ellipsometry (SE), which can give insight into both the film thickness as well as the film properties of the thin films. Several aspects of ultrathin film growth can be addressed by monitoring the process with spectroscopic ellipsometry. First, ellipsometry is an accurate diagnostic to determine the thickness of the deposited layer. Ellipsometry is fast and non-destructive and can be used on-wafer, which enables the *in situ* determination of the film thickness and, consequently, the growth rate of the process. The high sensitivity of ellipsometry (~ 0.01 monolayer) can also be used to study the film nucleation

at the early stages of growth [17]. For many ALD processes, a distinct nucleation delay is observed due to the limited density of nucleation sites on the substrate surface [9, 16]. Therefore, an understanding of the film nucleation is indispensable to know the film thickness after a certain number of cycles. Another important aspect which is closely related to initial film growth is substrate modification and interface layer formation which can take place during the deposition process. Especially for applications relying on interface properties or based on a nanolaminate stack of films, the oxidation or nitridation of the underlying material during film growth could affect the aimed device structure and, thereby, deteriorate the device performance [10, 18]. Because ellipsometry is sensitive to the optical constants of a material, it can be used to monitor the formation of an interfacial film given that the optical contrast between the different layers is sufficient.

Secondly, from the dielectric function of the deposited film determined from the spectroscopic ellipsometry data, material properties such as refractive index and extinction or absorption coefficient can be extracted. In addition, for thin metal films or films with metallic behavior, also the electronic properties can be calculated. Following the classical theory of light dispersion, the Drude theory can be used to model the intraband absorption in the metallic film [19, 20]. In an ideal metal with all electrons free, the unscreened plasma energy $\hbar\omega_{\text{pu}}$ is defined by the energy position where the real part of the dielectric function is zero [19]:

$$\hbar\omega_{\text{pu}} = \hbar\sqrt{\frac{Ne^2}{\varepsilon_0 m^*}}, \quad (1.1)$$

where \hbar is Dirac's constant, N is the conduction electron density, e is the electron charge, ε_0 is the permittivity of free space, and m^* is the electron effective mass. From the unscreened plasma energy in combination with the Drude broadening of the absorption, material parameters such as conduction electron density, electron mean free path, electrical resistivity, and mass density can be calculated. Therefore, *in situ* spectroscopic ellipsometry can be used to probe the electronic properties of films obtained under different deposition conditions as well as the dependence of the electronic properties on the film thickness. The so-called size effects become increasingly important for the future application of ultrathin films. For instance, Steinhögl *et al.* showed for the application of copper in interconnects, that the conductivity of the metal strongly depends on the dimensions. They reported that an increase in resistivity caused by size effects in narrow

copper lines (<100 nm) can not be avoided and will require design rule modification [8]. It is obvious that the change of material properties with film thickness is of key importance for ALD of ultrathin metallic films and should be studied in greater detail.

In addition to the work of Patsalas and co-workers who used spectroscopic ellipsometry to study dc reactive magnetron sputtered TiN films [21, 22], we will use *in situ* spectroscopic ellipsometry to obtain detailed information on the film thickness and the material properties during the plasma-assisted ALD growth process of ultrathin TiN films. First, the experimental procedure and ellipsometry data analysis procedure using the Drude-Lorentz oscillator parameterization will be described in more detail in Secs. II and III, respectively. The TiN film thickness and material properties determined by spectroscopic ellipsometry will be related to the results of *ex situ* diagnostics and aspects such as size effects, film nucleation, and interface layer formation during plasma-assisted ALD will be discussed in Sec. IV. The conclusions are given in Sec. V.

II Experimental Setup

The thin TiN films were deposited by the plasma-assisted ALD technique using the deposition system schematically shown in Fig. 1.1 and that is described extensively in a previous publication [6]. Briefly, the system consists of a deposition chamber, a TiCl_4 dosing system, and a plasma source, which are separated by pneumatic gate valves. The radio frequency plasma power (100 W) is coupled inductively to the plasma source which consists of a multiple-turn copper coil wrapped around a quartz tube. The wall-heated ($\sim 80^\circ\text{C}$) deposition chamber contains a resistively heated substrate holder ($25\text{--}500^\circ\text{C}$). A plasma-assisted ALD cycle consists of 5 s of TiCl_4 exposure, followed by a 10 s purge with argon gas, subsequently 15 s plasma exposure, and 10 s pump-down to base pressure (10^{-6} Torr). During TiCl_4 dosing the top and bottom pneumatic gate valves are closed and TiCl_4 vapor from a trapped volume is injected (Fig. 1.1). This leads to a pressure of 3 mTorr in the chamber during TiCl_4 dosing. The plasma is operated on H_2 and N_2 gas (10:1 ratio) at a total pressure of 11 mTorr.

The film growth was monitored by *in situ* SE using the optical viewports on the vacuum chamber (Fig. 1.1). The SE measurements were performed using a J.A. Woollam, Inc. M2000U visible and near infrared rotating compensator ellipsometer (0.75–5.0 eV). The ellipsometer light source consists of a high pressure xenon arc lamp, a fixed polarizer (P) and ro-

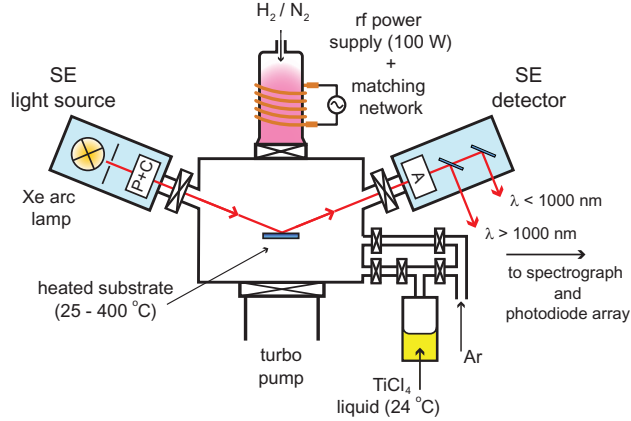


Figure 1.1: Schematic representation of the plasma-assisted atomic layer deposition system to deposit TiN films. The chamber is equipped with optical viewports to monitor the film growth *in situ* by spectroscopic ellipsometry.

tating compensator (C) to define the polarization state of the light. After reflection on the substrate the polarization state of the light is determined by a fixed analyzer (A). In the detector, two mirrors split the reflected light into infrared and visible light. These two light beams are coupled via two optical fibers towards the spectrographs and photodiode arrays where the spectroscopic information of the reflected light is extracted. The angle of incidence was fixed to 68° with respect to the substrate normal and is close to the Brewster angle of silicon, which enlarges the sensitivity of *in situ* SE when measuring on silicon-based substrates [23]. The spot size on the substrate was ~ 5 mm in diameter. Pneumatic gate valves are present between the vacuum chamber and the optical windows to prevent film deposition on the windows during the plasma-assisted ALD cycles.

The plasma-assisted ALD TiN films were deposited on different substrate materials. Depositions on native oxide covered *c*-Si substrates were used to determine typical material properties of the TiN film. The nucleation of TiN was studied on different silicon oxide substrates prepared by the method of calcination. The surface of the silicon oxides are covered with hydroxyl groups and siloxane bridges with the surface density of the hydroxyls mainly depending on the preheat temperature of the oxide [24]. Thermal oxides were prepared by heating *c*-Si substrates up to 750°C (24 h, ~ 50 nm SiO_2) and 1000°C (6 h, ~ 180 nm SiO_2) and the oxide surfaces are reported to have a hydroxyl density of $1\text{--}2\text{ nm}^{-2}$ and $0\text{--}0.5\text{ nm}^{-2}$, respectively [24]. The nucleation on these oxides was com-

pared to the growth on a standard, as-received thermal silicon oxide wafer (~ 410 nm SiO₂ on *c*-Si). Furthermore, plasma-assisted ALD was studied on H-terminated *c*-Si substrates obtained by removal of the native oxide from a Si wafer with a 2% buffered HF solution.

The film properties obtained from the *in situ* SE data were compared to the properties obtained by *ex situ* diagnostics [7]. The film thickness and mass density were determined from x-ray reflectometry (XRR). The film stoichiometry and impurity content were determined by Rutherford backscattering spectroscopy (RBS), elastic recoil detection (ERD), and x-ray photoelectron spectroscopy (XPS). Four-point probe (FPP) measurements and x-ray diffraction (XRD) were used to determine the film resistivity and grain size, respectively.

III Spectroscopic Ellipsometry

A. Data acquisition and optical model

After each plasma-assisted ALD cycle, spectroscopic data over the entire photon energy range was obtained by opening the gate valves to the ellipsometer light source and detector. To obtain a high signal to noise ratio in both the visible and the infrared part of the spectrum, each SE measurement consisted of the averaging of 500 data acquisitions leading to a measurement time of approximately 1 minute. After the measurement, the gate valves were closed and the deposition process continued.

From model-based analysis of the ellipsometry data, the thickness of the film (for sufficiently thin films in the case of metallic films) as well as the optical constants can be extracted. The ellipsometry data can be expressed in terms of the pseudo-dielectric function $\langle \varepsilon \rangle$, which is represented in a real $\langle \varepsilon_1 \rangle$ and imaginary $\langle \varepsilon_2 \rangle$ part. Prior to the film deposition, the pseudo-dielectric function of the substrate was determined. For the H-terminated *c*-Si substrates, the pseudo-dielectric function was modeled with a semi-infinite silicon substrate which includes the substrate temperature dependence of the optical constants of silicon [25]. The substrate modeling of the native and thermal oxide substrates required an additional Cauchy layer to describe the contribution of the transparent oxide film to the pseudo-dielectric function of the substrate [17].

The deposited TiN film was modeled by adding another layer on top of the substrate model. Assumptions within this approach are that the deposition process does not affect the substrate properties and that a surface roughness layer can be neglected. The latter assumption was validated

by the low surface roughness (0.4 nm for a 12 nm film) observed by AFM measurements (see Sec. IV). In the present work, the modeling of the ellipsometry data was performed using the WVASE32 software for data analysis from J.A. Woollam [26]. The quality of the fit can be expressed by the mean squared error (MSE) between the experimental data and the model fit. The data fitting used a Levenberg-Marquard algorithm to minimize the MSE [17].

B. Dielectric function of TiN

1. Drude-Lorentz oscillator parameterization

The dielectric function of the TiN films can be modeled by a Drude-Lorentz oscillator parameterization [21, 22]. The Drude oscillator accounts for the intraband absorption of the free electrons and, therefore, contains information on the metallic properties of the TiN film [19]. The interband absorption in the TiN can be described by Lorentz oscillators [21]. In the literature, the dielectric function of TiN is often composed of two Lorentz oscillators to account for the interband absorption around 3.5 and 5.2 eV [21, 27, 28]. We adopted the same model and described the dielectric function ε by the combination of a Drude term and two Lorentz oscillators:

$$\varepsilon(\omega) = \varepsilon_\infty - \frac{\omega_{\text{pu}}^2}{\omega^2 - i\Gamma_D\omega} + \sum_{j=1}^2 \frac{f_j\omega_{0j}^2}{\omega_{0j}^2 - \omega^2 + i\gamma_j\omega}. \quad (1.2)$$

In Eq. 1.2, ε_∞ is equal or larger than unity to compensate for the contribution of higher-energy transitions that are not taken into account by the Lorentz terms. The Drude term is characterized by the unscreened plasma energy $\hbar\omega_{\text{pu}}$ and the damping factor Γ_D . The Lorentz oscillators are located at energy position $\hbar\omega_{0j}$, with strength f_j , and damping factor γ_j .

Figure 1.2 shows a typical example of the dielectric function of a thin TiN film, which was deposited in 220 cycles onto a thermal oxide substrate prepared at 750 °C. The dielectric function of the thin TiN film was extracted from the data by the Drude-Lorentz parameterization. Both the real (ε_1) and imaginary (ε_2) part of the dielectric function are shown and the contributions of the Drude and Lorentz oscillators are indicated. Due to the near-infrared extension down to a photon energy of 0.75 eV, a large part of the Drude oscillator is probed and, therefore, the Drude term can be fitted with high accuracy.

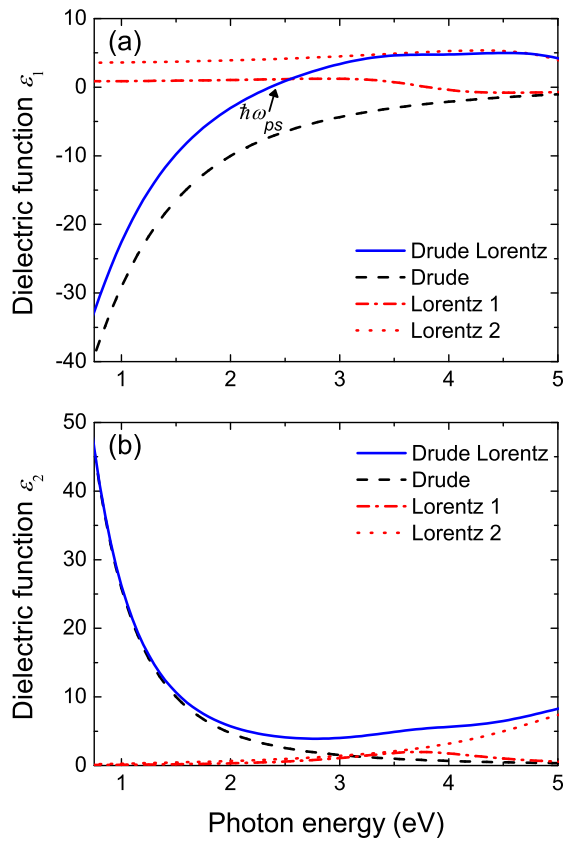


Figure 1.2: (a) The real (ϵ_1) and (b) the imaginary (ϵ_2) part of the dielectric function for an 11.7 nm thick TiN film deposited at 400 °C as obtained from the spectroscopic ellipsometry data using the Drude-Lorentz parameterization. The separate contributions of the Drude and two Lorentz oscillators to the dielectric functions are indicated.

From the Drude oscillator parameters, material parameters such as the conduction electron density (Eq. 1.1), the mean free path (MFP) of the conducting electrons, the resistivity (ρ), and mass density (ρ_m) can be calculated according to the free-electron model [19]:

$$\text{MFP} = \hbar \left[\frac{3\pi^2 \varepsilon_0}{(m^* e)^2} \right]^{1/3} \frac{\omega_{\text{pu}}^{2/3}}{\Gamma_D}, \quad (1.3)$$

$$\rho = \left(\frac{1}{\varepsilon_0} \right) \frac{\Gamma_D}{\omega_{\text{pu}}^2}, \quad (1.4)$$

$$\rho_m = \left(\frac{\varepsilon_0 m^* A}{e^2 N_0 Z} \right) \omega_{\text{pu}}^2, \quad (1.5)$$

where N_0 is the number of Avogadro, Z is the number of conduction electrons per atom, and A is the atomic mass of the material, respectively. For TiN, the atomic mass is $A (=A_{\text{Ti}} + A_{\text{N}}) = 62$ amu and we assume a value of $Z=0.95$ [21]. An estimation on the effective electron mass is required to calculate the mass density. Following Patsalas *et al.*, we estimate the effective electron mass to be $m^* = 1.15m_e$, in which m_e is the electron rest mass [21].

The Lorentz oscillators can be used to obtain insight into the stoichiometry of the TiN film. In the literature, it is reported that the stoichiometry of the films can be related to the screened plasma energy [29, 30]. In contrast to the unscreened plasma energy which is defined for an ideal metal (only a Drude oscillator), the screened plasma energy ($\hbar\omega_{\text{ps}}$) is introduced for a non-ideal metal with interband transitions related to absorptions by bound electrons. The screened plasma energy is defined by the energy position where the real part of the dielectric function of the non-ideal metal is zero (cf. Fig. 1.2). The strength and position of the Lorentz oscillators will mainly affect the screened plasma energy and, thereby, give insight into the film stoichiometry. However, it must be noted that the Lorentz oscillator fitting is often not unique resulting in a relatively large uncertainty in the Lorentz fit parameters.

2. Direct numerical inversion

The dielectric function of the TiN film can also be extracted directly from the pseudo-dielectric function of the total sample by the method of direct numerical inversion [31]. Assuming that the substrate properties are not affected by the deposition, trial spectra of ε_1 and ε_2 can be obtained by a wavelength point-to-point exact numerical inversion using trial film

thicknesses. This procedure is repeated for several trial thicknesses and it is decided upon the correct film thickness from the criterion that the ε_1 and ε_2 spectra should be smooth and show no unphysical artifacts such as strange (oscillatory) features. Here, the method of direct numerical inversion was used to examine whether the Drude-Lorentz parameterization is adequate to model the very thin TiN films. Figure 1.3 shows a comparison of the dielectric functions obtained from both model approaches applied to the same data used in Fig. 1.2. It is seen that the dielectric functions of both the model approaches overlap very well in a large photon energy region. The TiN film thicknesses obtained from the Drude-Lorentz parameterization and the direct numerical inversion method result in consistent thicknesses of 11.7 ± 0.5 nm and 11 ± 1 nm, respectively. Furthermore, it is observed that both methods show good agreement for film thicknesses down to 3 nm, as reported elsewhere [32].

The pseudo-dielectric function of a 65 nm thick TiN film is also plotted in Fig. 1.3. The pseudo-dielectric function of this thick film is approximately equal to the bulk TiN dielectric function because the film is nearly opaque. Fig. 1.3 shows that the dielectric function of the thin TiN film has a good overlap with the pseudo-dielectric function of the thick TiN film. A slight discrepancy between the dielectric function of the thin and thick TiN is however observed at higher photon energies. The influence of a surface roughness layer on the dielectric function of the thin film was simulated, but could not account for the observed difference. Most likely, the discrepancy can be explained by slight change in TiN material properties during growth (see Sec. IV), which might shift the Lorentz oscillator to a higher photon energy.

From a careful examination, it was found that the film thickness deduced does not depend critically on the specific material properties used. This has the important implication that the film thickness as a function of plasma-assisted ALD cycles can be accurately determined using the fit parameters that are optimized for the final film thickness. This approach makes the data analysis less laborious than having to optimize the complete set of model parameters to extract film thickness for each *in situ* measurement. Typical Drude-Lorentz fit parameters for a thin and a thick TiN film are presented in Table 1.1. These values are compared to values obtained from the literature and a good agreement in Drude-Lorentz fit parameters is found with the results obtained by Patsalas *et al.*, who used dc reactive magnetron sputtering and an additional substrate bias to deposit their TiN films [21]. In particular, the Drude term is well-defined due

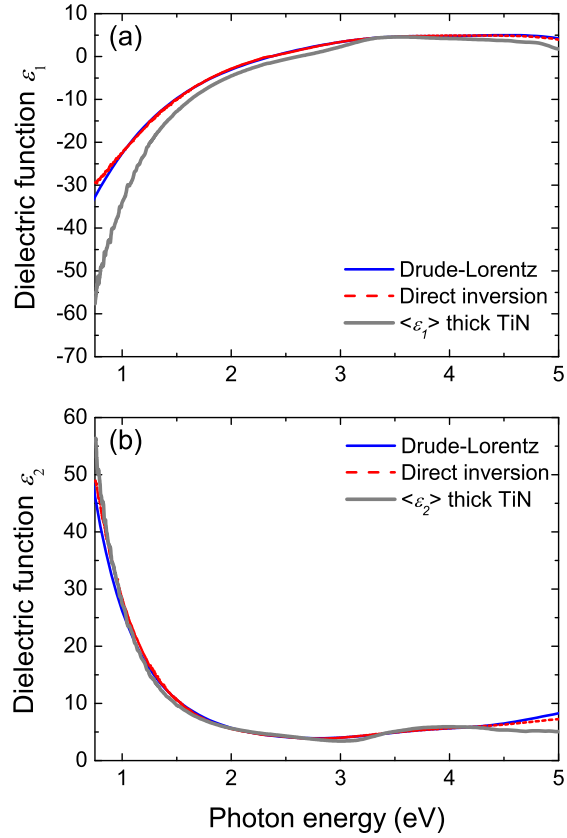


Figure 1.3: (a) The real (ϵ_1) and (b) the imaginary (ϵ_2) part of the dielectric function of an 11.7 nm thick TiN film deposited at 400 °C as obtained from the spectroscopic ellipsometry data using the Drude-Lorentz parameterization and the direct numerical inversion method. The dielectric functions are compared to the pseudo-dielectric functions $\langle \epsilon_1 \rangle$ and $\langle \epsilon_2 \rangle$ of a nearly opaque 65 nm thick TiN film.

Table 1.1: Typical Drude-Lorentz oscillator model parameters for a thin and a thick (nearly-opaque) TiN film deposited by plasma-assisted ALD at 400°C. The unscreened plasma energy $\hbar\omega_{\text{pu}}$ and the Drude broadening Γ_D are given for the Drude term. The oscillator strength f_j , position $\hbar\omega_{0j}$, and broadening γ_j are shown for the two Lorentz oscillators and the offset energy ε_∞ takes higher energy terms into account. The values reported by Patsalas *et al.* for dc magnetron sputtered TiN films (thickness 10–100 nm) are shown for comparison [21]

	12 nm plasma-assisted ALD	65 nm plasma-assisted ALD	10–100 nm magnetron sputtered TiN
Drude			
$\hbar\omega_{\text{pu}}$ (eV)	7.22±0.05	7.29±0.02	5.7–7.8
$\hbar\Gamma_D$ (eV)	0.86±0.05	0.61±0.01	0.3–1.1
Lorentz			
f_1	0.8±0.2	0.2±0.1	0.1–0.6
$\hbar\omega_{01}$ (eV)	3.8±0.1	3.6±0.1	3.62–3.68
$\hbar\gamma_1$ (eV)	1.6±0.1	0.7±0.1	0.7–1.0
f_2	3.5±0.3	5.8±0.1	1.5–5.8
$\hbar\omega_{02}$ (eV)	5.6±0.1	6.4±0.1	5.2–6.3
$\hbar\gamma_2$ (eV)	2.3±0.3	4.7±0.2	2.3–3.8
ε_∞ (eV)	3.0±0.1	1.5±0.1	Not reported

to the dominant contribution in the dielectric function (cf. Fig. 1.2). The fit procedure was therefore mainly focused on this Drude term, which is also used to calculate the material parameters of the TiN film. The results obtained are compared to *ex situ* analysis in the next section.

IV Results and Discussion

A. Material properties of ultrathin TiN films determined by *in situ* SE

1. Physical properties of TiN films

Spectroscopic ellipsometry is used to monitor the plasma-assisted ALD of TiN for different deposition temperatures (100–400 °C) on native oxide covered silicon substrates. The TiN film thickness as a function of plasma-assisted ALD cycles is shown in Fig. 1.4. The material properties calculated from the *in situ* ellipsometry data are shown in Table 1.2 for the films ranging in thickness between 10 to 23 nm. Figure 1.4 shows that the film thickness is linear with the number of ALD cycles for the full range of deposition temperatures investigated, apart from a nucleation region (<50 cycles) for initial film growth (see Sec. IV B). The growth rate of the plasma-assisted ALD process is given by the slope of the growth curves for the linear growth region (cf. Table 1.2) and it is observed that the growth rate per cycle increases with increasing deposition temperature. Such an increase in growth rate with deposition temperature was also reported by others for similar ALD processes [33, 34].

Ex situ XRR measurements were carried out to measure the film thickness for TiN films deposited at H-terminated *c*-Si substrates, however, the films were deposited with a different number of cycles compared to the films listed in Table 1.2. Therefore, the growth rate obtained from both techniques will be compared. The growth rates calculated from the XRR measurements are 0.062 ± 0.002 , 0.035 ± 0.002 , 0.027 ± 0.002 , and 0.026 ± 0.002 nm/cycle for depositions at 400, 300, 200, and 100 °C, respectively, which is in fair agreement with the growth rate obtained by SE.

Atomic force microscopy data in Table 1.2 shows that the deposited films have a low surface roughness which is comparable to the surface roughness (~ 0.3 nm) of the substrate itself. On the basis of this low surface roughness, as expected for the layer-by-layer growth by ALD, we conclude that the films are sufficiently smooth to omit a surface roughness layer in the optical model used for SE data analysis.

Table 1.2: Material properties of thin TiN films deposited on native oxide covered *c*-Si substrates at different substrate temperatures. Using the Drude-Lorentz parameterization, the film thickness, growth rate, conduction electron density, electron mean free path (MFP), resistivity, and mass density are calculated from the *in situ* ellipsometry data. The resistivity and electron MFP are given at deposition temperature and at room temperature (in between brackets). The accuracy of the data fit is expressed by the mean squared error (MSE) of the fit. Atomic force microscopy is used to determine the surface roughness, while the stoichiometry and impurity content are determined by Rutherford backscattering spectroscopy. The typical absolute errors in the parameters are shown for the substrate temperature of 400 °C unless indicated otherwise.

	Deposition temperature			
	400 °C	300 °C	200 °C	100 °C
MSE of fit	16	16	18	95
Film thickness (nm)	23.0±0.5	17.1	10.7	10.2±1
Growth rate (nm/cycle)	0.057±0.001	0.044	0.028	0.028±0.003
Conduction electron density N (10^{22} cm ⁻³)	4.4±0.1	4.3	4.3	4.6±0.3
Electron mean free path (MFP) (nm)	0.72 (0.90)±0.05	0.73 (0.86)	0.59 (0.68)	0.32 (0.36)±0.2
Resistivity ρ ($\mu\Omega$ cm)	142 (121)±10	142 (126)	176 (166)	315 (310)±40
Mass density ρ_m (g cm ⁻³) ^a	4.7±0.1	4.7	4.6	5.0±0.4
Surface roughness (nm)	0.5±0.1	0.5	0.3	0.4
Stoichiometry [N]/[Ti]	1.0±0.05	0.91	0.95	1.0
Cl content (at. %)	0.3±0.2	0.4	1	7
O content (at. %)	1.6±0.2	2.8	1.4	4.4

^aAssuming that the effective mass $m^* = 1.15m_e$ as reported in Ref. 21

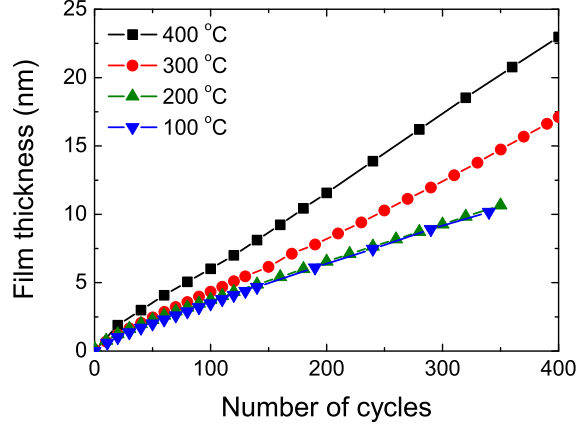


Figure 1.4: Thickness of TiN films as a function of number of plasma-assisted ALD cycles as obtained by *in situ* spectroscopic ellipsometry. The films were deposited on native oxide covered *c*-Si substrates for substrate temperatures between 100 and 400 °C.

RBS analysis showed that the TiN films are (nearly) stoichiometric ($[N]/[Ti] = 1.0 \pm 0.1$) with only a small Cl and O impurity content. This shows that good quality TiN films can be deposited by plasma-assisted ALD even at a low substrate temperature, while it also validates the SE data analysis based on the Drude-Lorentz parameterization for TiN. The film stoichiometry is also deduced from the SE analysis by the determination of the screened plasma energy. We found that the screened plasma energy of the deposited films does not depend on deposition temperature and the value of $\hbar\omega_{ps} = 2.3 \pm 0.1$ eV corresponds to a slightly overstoichiometric TiN_x ($x = 1.1$) film [29, 30]. Considering the uncertainty in this method, this is in fair agreement with the results obtained by RBS analysis.

The mass density calculated from *in situ* SE can be compared with *ex situ* XRR data for two thick TiN films that were deposited at 100 and 400 °C in order to obtain a sufficient sensitivity in the XRR mass density. For a 45 nm thick TiN deposited at 100 °C mass densities of 3.9 ± 0.1 and 3.7 ± 0.1 g cm⁻³ were obtained from the SE and XRR data respectively. For a 65 nm thick TiN deposited at 400 °C, the SE and XRR measurements resulted in 4.8 ± 0.1 and 4.9 ± 0.1 g cm⁻³, respectively. These values for the mass density are somewhat lower than the literature value for bulk TiN (5.21 g cm⁻³) [35], but the values are similar to densities of thin TiN films reported in the literature [9, 21].

2. Electronic properties of TiN films

The electronic properties of the TiN films are directly calculated from the *in situ* SE data using the Drude-Lorentz parameterization. However, the electronic properties of the TiN film depend on the substrate temperature due to electron-phonon scattering [36]. Therefore, to make a correct comparison between the electronic properties of the films deposited at different temperatures, these properties should be determined at the same substrate temperature. To do so, the temperature coefficient of the electronic properties was determined and used to correct the *in situ* data obtained at the specific deposition temperature to room temperature.

A TiN film was deposited at a substrate temperature of 400 °C and *in situ* SE was used to monitor the change in the Drude fit parameters as a function of substrate temperature during the cooling down of the sample. It was observed that only the Drude broadening varied with temperature and that the unscreened plasma energy remained approximately constant. The resistivity, electron MFP and conduction electron density were calculated from the data and are shown in Fig. 1.5 as a function of substrate temperature. The resistivity increases and the electron MFP decreases linearly with increasing substrate temperature as caused by a more pronounced electron-phonon scattering at higher substrate temperature. Electron-phonon scattering should have no influence on conduction electron density, which is validated by the temperature independent conduction electron density observed in Fig. 1.5(b). The calculated temperature coefficient of resistivity (TCR) for TiN of $5.5 \times 10^{-4} \text{ K}^{-1}$ is in good agreement with the TCR values of $6 \times 10^{-4} \text{ K}^{-1}$ [37] and $(1.9\text{--}8.3) \times 10^{-4} \text{ K}^{-1}$ [38] reported for TiN in the literature.

The resistivity values determined by *in situ* SE for the films deposited at different substrate temperatures were corrected to room temperature and are compared to *ex situ* four-point probe (FPP) measurements in Fig. 1.6(a). The figure shows that the resistivity of the TiN films decreases with increasing deposition temperature. A good agreement is observed between the *in situ* SE and *ex situ* FPP data for substrate temperatures between 200 and 400 °C. The larger difference observed for 100 °C can possibly be attributed to post-process oxidation [39] of the 100 °C TiN film which has a lower mass density (as clearly suggested by the 45 nm thick film) and a higher O impurity content (cf. Table 1.2). Furthermore, from the data we can draw the important conclusion that our plasma-assisted ALD technique results in low resistivity TiN films, even at 100 °C deposition temperature as compared with results reported in the litera-

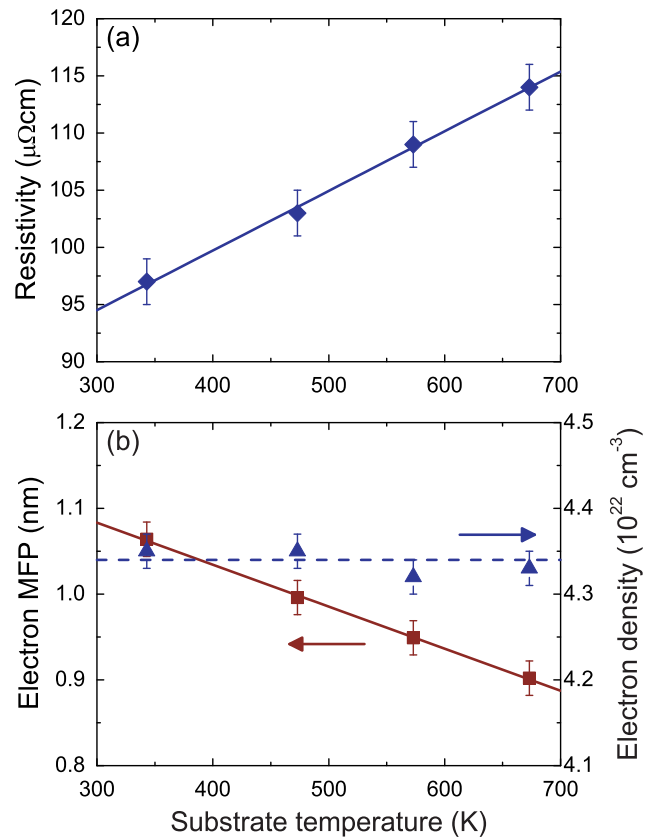


Figure 1.5: The intrinsic temperature dependence of (a) the resistivity, and (b) the electron mean free path (MFP) and the conduction electron density. The data were obtained for a TiN film deposited at $400\text{ }^\circ\text{C}$ by monitoring the film by ellipsometry during the cooling down process from 400 to $70\text{ }^\circ\text{C}$. For the resistivity and electron mean free path, the solid lines are fits to the data which are used to extrapolate the *in situ* data to room temperature. The dashed line for the conduction electron density is a guide to the eye.

ture [7, 34, 40].

The electrical resistivity of a metallic film is inversely proportional to both the electron MFP as well as the conduction electron density. Therefore, the trend of the resistivity in Fig. 1.6(a) can be understood in more detail by considering these properties, which were also calculated from the *in situ* SE data and which are shown in Fig. 1.6(b). The figure shows that the electron MFP increases with deposition temperature, while the conduction electron density remains virtually constant. The observed increase in resistivity for lower deposition temperature in Fig. 1.6(a) can therefore be attributed to the decrease in electron MFP.

The electron MFP can be compared to the grain size, which was determined from XRD analysis on the 45 nm thick TiN film deposited at 100 °C. The XRD analysis showed that the TiN film contained elliptical grains with a height and lateral width of 10 nm and 6 nm, respectively. Assuming that films initially grow by the coalescence of nucleation sites, we estimate that a thinner TiN film will have a smaller grain height, but a similar value of the lateral grain size. This estimation is substantiated by Li *et al.*, who determined the grain size of a thin TiN film. They reported a lateral grain size of 4 nm for 6 nm thin TiN films deposited by dc reactive magnetron sputtering [14]. Consequently, the observed electron MFP of the TiN films deposited at 100 °C is an order of magnitude smaller than the grain size determined with XRD. Therefore, it can be concluded that the electron MFP is not limited by the grain size of the TiN film but by the presence of point defects and impurities in the film (cf. Table 1.2). Especially the increasing Cl impurity level shows a clear correlation with the decreasing electron mean free path in the film as shown in Fig. 1.6(b).

B. Issues related to ultrathin TiN film growth

In the previous section, it was shown that information on important material properties of the TiN films can be obtained by *in situ* SE and that the results are in good agreement with those obtained from *ex situ* analysis techniques. In this section, *in situ* SE will be used to get a more detailed understanding of film growth by plasma-assisted ALD. Three important issues of ultrathin film growth will be addressed, i.e., size effects in ultrathin metallic films, nucleation for films deposited by ALD, and interface layer formation during the plasma-assisted ALD growth process.

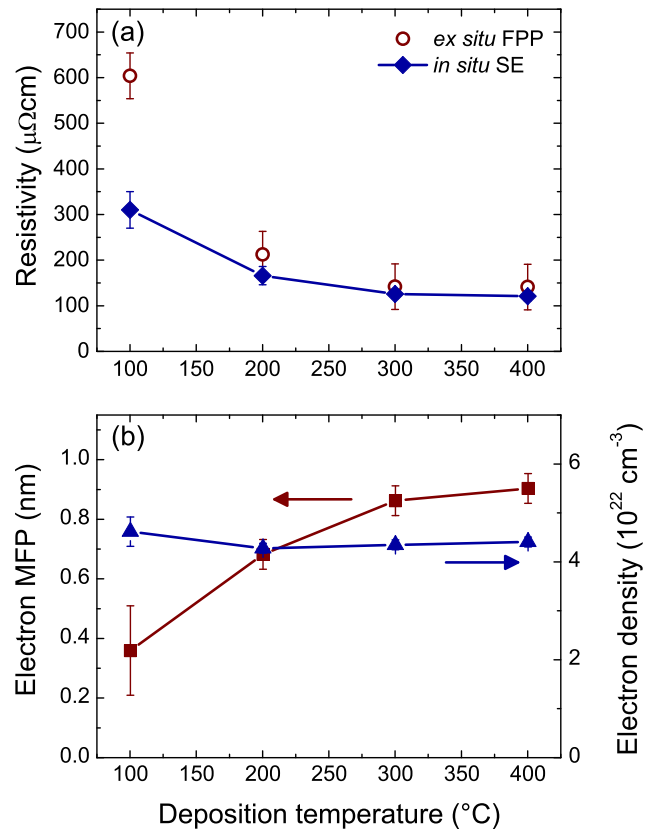


Figure 1.6: (a) Room temperature values of the resistivity, determined by *in situ* spectroscopic ellipsometry and *ex situ* four-point probe analysis, and (b) the electron mean free path (MFP) and the conduction electron density as a function of deposition temperature. The data obtained at a certain deposition temperature was converted to room temperature values using the relations presented in Fig. 1.5.

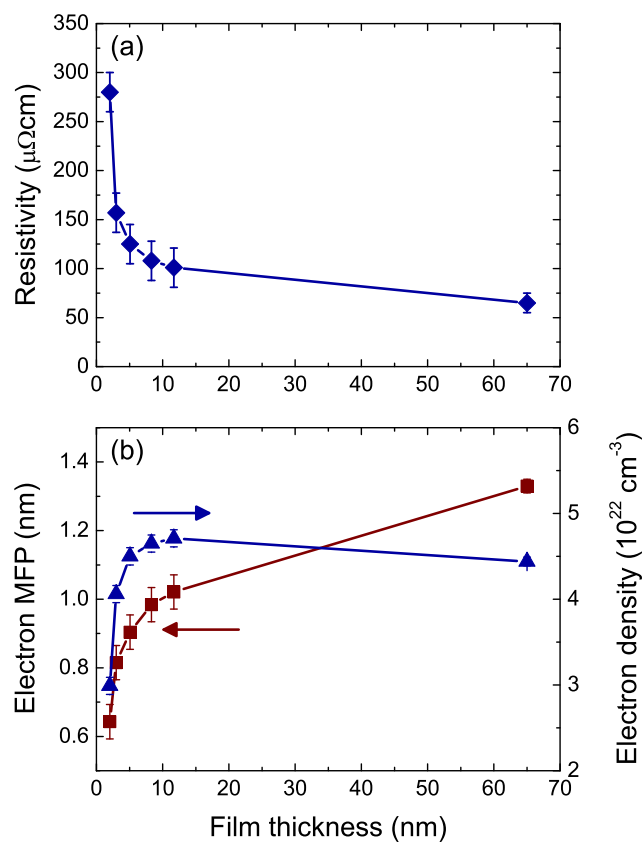


Figure 1.7: (a) The resistivity, and (b) the electron mean free path and the conduction electron density as a function of film thickness monitored by *in situ* spectroscopic ellipsometry. The film was deposited at 400 °C and the data was converted to represent room temperature values.

1. Size effects

In situ SE is used to monitor the change in electrical properties of TiN as a function of the film thickness for a film deposited at 400 °C. The complete Drude-Lorentz oscillator model is optimized for various film thicknesses and from the optimized fit parameters, the resistivity is calculated as a function of film thickness. Figure 1.7(a) shows that the resistivity is increasing for decreasing film thickness revealing a clear thickness dependence of the electrical properties of the TiN. The resistivity of the 65 nm thick film of $65 \pm 10 \mu\Omega \text{ cm}$ is in good agreement with the resistivity value of $71 \pm 10 \mu\Omega \text{ cm}$ determined by *ex situ* FPP.

The electron MFP and conduction electron density were also calculated as a function of film thickness and are shown in Fig. 1.7(b). The electron MFP decreases with decreasing film thickness, while the conduction electron density is constant down to a film thickness of 5 nm and decreases when going to even a thinner film. The decrease in electron MFP with decreasing film thickness is the result of a more pronounced contribution of electron-sidewall scattering, which start to dominate the electron MFP for the ultrathin films [8, 41]. In principle, electron-sidewall scattering always has a contribution to the total of scattering mechanisms in the film, but can be neglected for thick films. Figure 1.7(b) therefore clearly reveals that size effects are strongly influencing the material properties for ultrathin films and that these size effects can be investigated by *in situ* SE.

2. Film nucleation

The high sensitivity of SE in combination with the ALD technique is an excellent tool to study the nucleation of thin films on differently prepared substrates. To this end, TiN films were deposited at a substrate temperature of 400 °C on different thermal oxides prepared by the procedures described in Sec. II. During the nucleation phase, *in situ* SE data is obtained after each plasma-assisted ALD cycle and Fig. 1.8 shows the TiN thickness as a function of the number of ALD cycles. A distinction in nucleation behavior on the different thermal oxides is observed as can clearly be seen from the inset of Fig. 1.8. All films show a nucleation delay after which the growth rate increases when the surface becomes completely covered with TiN nucleation sites. Figure 1.8 shows that at a film thickness of approximately 2 nm, film closure is obtained and the growth rate becomes constant as expected for ALD growth. The difference in nucleation

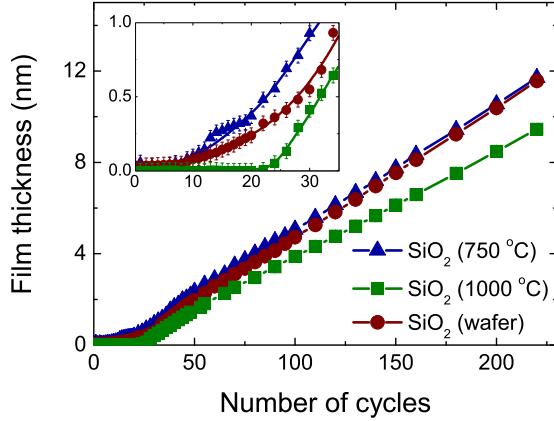


Figure 1.8: The thickness of TiN films grown on different thermal SiO₂ substrates monitored by *in situ* spectroscopic ellipsometry and shown as a function of number of plasma-assisted ALD cycles. The inset displays the initial growth region in more detail. Two substrates were prepared by the method of calcination and preheated at temperatures of 750 and 1000 °C, the other substrate was an as-received wafer with 410 nm thermal oxide.

delay can be related to the number of reactive surface groups on the initial thermal oxide surface [16, 24, 42]. The surface of thermal oxide mainly consists of siloxane bridges and only few hydroxyl groups are present depending on the preheat temperature of the oxide (750 °C: 1–2 OH nm⁻², 1000 °C: 0–0.5 OH nm⁻²) [24, 42]. Because the TiCl₄ precursor molecules can only react with the surface hydroxyls to form nucleation sites, the most distinct nucleation delay is observed for the thermal oxide preheated at 1000 °C. Satta *et al.* observed a similar nucleation delay on thermal oxide substrates using Rutherford backscattering spectroscopy [9]. A slight difference in growth rate after nucleation on different substrate material was also reported by Satta *et al.* [9], but the underlying mechanism is still unclear.

3. Interface layer formation

Another issue related to the application of the (plasma-assisted) ALD technique is the possible modification of the substrate by interface layer formation during growth. *In situ* SE can also be applied to study this effect as revealed by an experiment in which a TiN film is deposited on an H-terminated *c*-Si substrate, while the growth is monitored by *in situ* SE. To

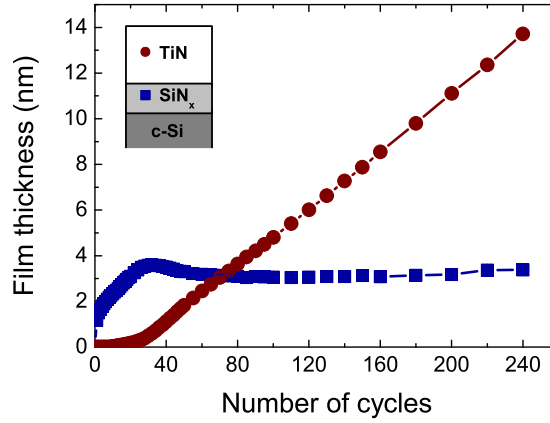


Figure 1.9: The thickness of a TiN film deposited by plasma-assisted atomic layer deposition on an H-terminated *c*-Si substrate shown as a function of the number of plasma-assisted ALD cycles. The inset shows the model used to analyze the *in situ* ellipsometry data. The change in thickness of a SiN_x interface layer formed during the plasma-assisted ALD process is also given.

fit the SE data, the two-layer SE model was extended with an additional layer to model the formation of an interface layer of SiN_x in between the *c*-Si substrate and TiN film, as also supported by *ex situ* RBS and XPS measurements. The dielectric function of the interfacial SiN_x was modeled by means of a standard Cauchy dispersion relation [17] and the TiN and SiN_x thickness were fitted as a function of the number of plasma-assisted ALD cycles. Figure 1.9 shows the resulting change in thickness of the TiN and SiN_x films. Prior to the TiN film growth, the formation of the SiN_x layer is observed, which can be explained by the exposure of the substrate to the H₂-N₂ plasma. Subsequently, the TiN film nucleates on the SiN_x surface. Figure 1.9 shows that the interfacial film thickness finally saturates to a thickness of 3.4 nm. The interface layer thickness determined from the SE data is close to the interface thickness determined by XPS (~2.5 nm) and RBS analysis (~3 nm).

In the literature, it is reported that TiCl₄ molecules do not react with silicon-hydrides on a crystalline silicon surface [43]. As a consequence, the film nucleation is very slow on H-terminated *c*-Si, because the TiCl₄ molecules can only nucleate on surface defects [16]. The plasma-induced formation of the SiN_x film creates surface groups such as NH_x groups that are reactive to the TiCl₄ molecules and facilitates the film nucleation. The formation of an interfacial layer during (PA-)ALD is also observed for the

growth of HfO_2 [44–46] and Al_2O_3 [15, 47], but the use of *in situ* SE to monitor the interface formation during ALD has not been reported yet.

V Conclusions

The growth process of ultrathin TiN films by the plasma-assisted atomic layer deposition technique was monitored by *in situ* spectroscopic ellipsometry with a photon energy range of 0.75 to 5 eV. Adopting the Drude-Lorentz oscillator parameterization to describe the dielectric function of the TiN films, the film thickness and material properties were determined from the *in situ* ellipsometry data. The dielectric function of the thin TiN films and the film thickness obtained by the Drude-Lorentz parameterization showed good agreement with the dielectric function and film thickness obtained by the method of direct numerical inversion and with the bulk dielectric function of a (nearly) opaque TiN film. Furthermore, it was verified that the thickness and material properties of the thin TiN films determined by *in situ* spectroscopic ellipsometry were in good agreement with the results obtained by *ex situ* film analysis such as x-ray reflectometry and four-point probe measurements.

Because electronic properties such as conduction electron density, electron mean free path, and electrical resistivity can directly be obtained from the *in situ* ellipsometry data, the variation in resistivity of the TiN films with deposition temperature could be related to the change in electron mean free path in the films caused by a deposition temperature dependent impurity level in the films. Moreover, by acquiring *in situ* spectroscopic ellipsometry data during TiN film growth, several aspects related to thin film properties were addressed. The electrical resistivity of the films increased with decreasing film thickness (2–65 nm) and this so-called finite size effect is caused by a more pronounced electron-sidewall scattering for decreasing film thickness leading to a reduced electron mean free path. A distinct difference in nucleation delay on different thermal oxide substrates was observed by *in situ* SE, which could be directly related to the difference in density of surface hydroxyls on the substrates. Using ellipsometry to monitor the plasma-assisted ALD deposition of TiN on an H-terminated *c*-Si substrate, the formation of an interfacial SiN_x layer was observed before the onset of TiN film growth. It was therefore clearly established that fundamental insight into the growth of ultrathin films by techniques such as ALD can be obtained by monitoring the process with *in situ* spectroscopic ellipsometry.

Acknowledgments

Dr. P. C. Thune and E. M. E. van de Kimmenade of the Department of Chemical Engineering are thanked for the preparation of the thermal oxide substrates. Part of the *ex situ* analysis was carried out at Philips Research Eindhoven; the RBS analysis by Dr. Y. Tamminga and T. Dao, the XRD measurements by F. Bakker and Dr. H. Wondergem, and the XPS analysis by A. H. C. Hendriks. Dr. A. Rahtu of ASM Microchemistry is acknowledged for the XRR thickness and density calculations. M. J. F. van de Sande, J. F. C. Jansen, A. B. M. Hüsken, and H. M. M. de Jong are thanked for their skillful technical assistance. This work was supported by the Dutch Technology Foundation STW. The research of one of the authors (W.M.M.K.) has been made possible by a fellowship from the Royal Netherlands Academy of Arts and Sciences (KNAW).

Bibliography

- [1] T. Suntola, Mater. Sci. Rep. **4**, 261 (1989).
- [2] M. Leskelä and M. Ritala, Thin Solid Films **409**, 138 (2002).
- [3] M. Ritala and M. Leskelä, *Handbook of Thin Film Materials*, volume 1, Academic, San Diego, CA (2001).
- [4] H. Kim, J. Vac. Sci. Technol. B **21**, 2231 (2003).
- [5] K.-E. Elers, J. Winkler, K. Weeks, and S. Marcus, J. Electrochem. Soc. **152**, G589 (2005).
- [6] S. B. S. Heil, E. Langereis, A. Kemmeren, F. Roozeboom, M. C. M. van de Sanden, and W. M. M. Kessels, J. Vac. Sci. Technol. A **23**, L5 (2005).
- [7] S. B. S. Heil, E. Langereis, F. Roozeboom, M. C. M. van de Sanden, and W. M. M. Kessels, J. Electrochem. Soc. **153**, G956 (2006).
- [8] W. Steinhögl, G. Schindler, G. Steinlesberger, M. Traving, and M. Engelhardt, J. Appl. Phys. **97**, 23706 (2005).
- [9] A. Satta, A. Vantomme, J. Schuhmacher, C. M. Whelan, V. Sutcliffe, and K. Maex, Appl. Phys. Lett. **84**, 4571 (2004).
- [10] Y. Travaly, J. Schuhmacher, A. M. Hoyas, M. V. Hove, K. Maex, T. Abell, V. Sutcliffe, and A. M. Jonas, J. Appl. Phys. **97**, 84316 (2005).
- [11] A. Satta, M. Baklanov, O. Richard, A. Vantomme, H. Bender, T. Conard, K. Maex, W. M. Li, K.-E. Elers, and S. Haukka, Microelect. Eng. **60**, 59 (2002).
- [12] F. Greer, D. Fraser, J. W. Coburn, and D. B. Graves, J. Vac. Sci. Technol. A **21**, 96 (2003).
- [13] J. W. Elam, M. Schuisky, J. D. Ferguson, and S. M. George, Thin Solid Films **436**, 145 (2003).
- [14] T. Q. Li, S. Noda, F. Okada, and H. Komiyama, J. Vac. Sci. Technol. B **21**, 2512 (2003).

- [15] M. M. Frank, Y. J. Chabal, and G. D. Wilk, *Appl. Phys. Lett.* **82**, 4758 (2003).
- [16] S. Haukka, E.-L. Lakomaa, and A. Root, *J. Phys. Chem.* **97**, 5085 (1993).
- [17] H. G. Tompkins and W. A. McGahan, *Spectroscopic Ellipsometry and Reflectometry*, John Wiley & Sons, Inc., New York (1999).
- [18] B. Sell, A. Sanger, and W. Krautschneider, *J. Vac. Sci. Technol. B* **21**, 931 (2003).
- [19] N. W. Ashcroft and N. D. Mermin, *Solid State Physics*, Saunders College, Orlando, FL (1976).
- [20] F. Wooten, *Optical Properties of Solids*, Academic, New York (1972).
- [21] P. Patsalas and S. Logothetidis, *J. Appl. Phys.* **90**, 4725 (2001).
- [22] P. Patsalas and S. Logothetidis, *J. Appl. Phys.* **93**, 989 (2003).
- [23] H. G. Tompkins and E. A. Irene, *Handbook of Ellipsometry*, William Andrews, Inc., New York (2005).
- [24] L. T. Zhuravlev, *Colloids Surf. A: Physicochem. Eng. Aspects* **173**, 1 (2000).
- [25] G. E. Jellison, Jr. and F. A. Modine, *Phys. Rev. B* **27**, 7466 (1983).
- [26] J. A. Woollam Co., Inc., 650 J Street, Suite 39, Lincoln, NE 68508, USA (<http://www.jawoollam.com>).
- [27] B. Karlsson, J.-E. Sundgren, and B.-O. Johansson, *Thin Solid Films* **87**, 181 (1982).
- [28] K. Postava, M. Aoyama, and T. Yamaguchi, *Appl. Surf. Sci.* **175-176**, 270 (2001).
- [29] S. Logothetidis, I. Alexandrou, and A. Papadopoulos, *J. Appl. Phys.* **77**, 1043 (1995).
- [30] J. H. Kang and K. J. Kim, *J. Appl. Phys.* **86**, 346 (1999).
- [31] H. Arwin and D. E. Aspnes, *Thin Solid Films* **113**, 101 (1984).

- [32] E. Langereis, S. B. S. Heil, M. C. M. van de Sanden, and W. M. M. Kessels, *Phys. Stat. Sol. C* **2**, 3958 (2005).
- [33] J. Kim, H. Hong, S. Ghosh, K.-Y. Oh, and C. Lee, *Jpn. J. Appl. Phys.* **42**, 1375 (2003).
- [34] D.-H. Kim, Y. J. Kim, J.-H. Park, and J. H. Kim, *Mater. Sci. Eng. C* **24**, 289 (2004).
- [35] D. R. Lide, *Handbook of Chemistry and Physics*, CRC Press, Boca Raton, 85th edition edition (2005).
- [36] N. Kontoleon, K. Papathanasopoulos, K. Chountas, and C. Papatoukoudis, *J. Phys. F: Met. Phys.* **4**, 2109 (1974).
- [37] H. Zafer Durusoy, O. Duyar, A. Aydinli, and F. Ay, *Vacuum* **70**, 21 (2003).
- [38] J. F. Creemer, P. M. Sarro, M. Laros, H. Schellevis, T. Nathoeni, L. Steenweg, V. Svetchnikov, and H. W. Zandbergen, in *Proceedings of SAFE 2004*, 724 (2004).
- [39] D.-H. Kim, J. J. Kim, J. W. Park, and J. J. Kim, *J. Electrochem. Soc.* **143**, L188 (1996).
- [40] K. Yokota, K. Nakamura, T. Kasuya, K. Mukai, and M. Ohnishi, *J. Phys. D* **7**, 1095 (2004).
- [41] A. F. Mayadas and M. Shatzkes, *Phys. Rev. B* **1**, 1382 (1970).
- [42] S. Haukka and T. Suntola, *Interface Sci.* **5**, 119 (1997).
- [43] G. C. Abeln, M. C. Hersam, D. S. Thompson, S.-T. Hwang, H. Choi, J. S. Moore, and J. W. Lyding, *J. Vac. Sci. Technol. B* **16**, 3874 (1998).
- [44] Y. Won, S. Park, J. Koo, J. Kim, and H. Jeon, *Appl. Phys. Lett.* **87**, 262901 (2005).
- [45] Y. Senzaki, S. Park, H. Chatham, L. Bartholomew, and W. Nieveen, *J. Vac. Sci. Technol. A* **22**, 1175 (2004).
- [46] P. S. Lysaght, B. Foran, G. Bersuker, P. J. Chen, R. W. Murto, and H. R. Huff, *Appl. Phys. Lett.* **82**, 1266 (2003).
- [47] S.-C. Ha, E. Choi, S.-H. Kim, and J. S. Roh, *Thin Solid Films* **476**, 252 (2005).

Chapter 2

Synthesis and *in situ* characterization of low-resistivity TaN_x films by remote plasma atomic layer deposition*

Abstract

The remote plasma atomic layer deposition (ALD) of TaN_x films from Ta[N(CH₃)₂]₅ and H₂, H₂-N₂, and NH₃ plasmas is reported. From film analysis by *in situ* spectroscopic ellipsometry and various *ex situ* techniques, data on growth rate, atomic composition, mass density, TaN_x microstructure, and resistivity are presented for films deposited at substrate temperatures between 150 and 250 °C. It is established that cubic TaN_x films with a high mass density (12.1 g cm⁻³) and low electrical resistivity (380 μΩ cm) can be deposited using a H₂ plasma with the density and resistivity of the films improving with plasma exposure time. H₂-N₂ and NH₃ plasmas resulted in N-rich Ta₃N₅ films with a high resistivity. It is demonstrated that the different TaN_x phases can be distinguished *in situ* by spectroscopic ellipsometry on the basis of their dielectric function with the magnitude of the Drude absorption yielding information on the resistivity of the films. In addition, the saturation of the ALD surface reactions can be determined by monitoring the plasma emission, as revealed by optical emission spectroscopy.

*Published as: E. Langereis, H. C. M. Knoop, A. J. M. Mackus, F. Roozeboom, M. C. M. van de Sanden, and W. M. M. Kessels, *J. Appl. Phys.* **102**, 083517 (2007).

I Introduction

The deposition of nanometer thick conductive tantalum nitride (TaN_x) films is relevant for various applications in next-generation semiconductor devices. TaN is considered as a candidate to replace the poly-Si gate in metal-oxide-semiconductor field effect transistors (MOSFET) [1], as metal electrode in high-density 3D capacitors [2], and as Cu diffusion barrier [3–5] and possible liner material for interconnect technology [6, 7]. In addition to a high level of growth control, several applications require conformal deposition in high-aspect ratio structures, which is a requirement beyond reach of current physical vapor deposition (PVD) techniques. Due to its layer-by-layer growth, atomic layer deposition (ALD) is believed to be the method of choice for deposition in demanding 3D features [4, 8–10]. Sequentially employing two self-limiting surface reactions, a sub-monolayer of material is deposited per ALD cycle and the process is proven to yield excellent uniformity and conformality [11–13]. Since different TaN_x crystal phases exist including low-resistivity cubic TaN and very-high-resistivity Ta₃N₅ [14], successful integration of TaN_x films synthesized by ALD requires control over film stoichiometry and composition.

Several precursors are commercially available for ALD of TaN_x films, such as Ta[N(CH₃)₂]₅ (PDMAT) [4], Ta[N(C₂H₅)₂]₃NC(CH₃)₃ (TBTDET) [15], Ta[NC(CH₃)₂C₂H₅][N(CH₃)₂]₃ (TAIMATA) [16], TaCl₅ [10, 17], and TaF₅ [18]. For many applications metal-organic precursors are preferred over metal-halide precursors due to potential problems in reliability posed by halide impurities in the film [4]. In order to deposit the conductive TaN_x phase, the oxidation state of the Ta atom in the precursor (+5 in most precursors) has to be reduced to oxidation state +3. Using the PDMAT precursor with NH₃ in a thermal ALD process, Travaly *et al.* observed that the high-resistivity Ta₃N₅ phase was deposited [19]. Ritala *et al.* showed that the reducing power of NH₃ is indeed insufficient and thermal ALD using TaCl₅ precursor resulted in the deposition of the Ta₃N₅ phase [10]. They reported that they could only deposit conductive TaN_x films by thermal ALD when applying additional zinc dosing during the NH₃ exposure. Recently, it was demonstrated that low-resistivity TaN films can be deposited by plasma-assisted ALD using the reducing power of a H₂ plasma in combination with the metal-organic precursors PDMAT [4] or TBTDET [15]. Sreenivasan *et al.* reported the deposition of Ta₃N₅ using an amido-based Ta precursor and a H₂-N₂ plasma and they showed that the conductive cubic TaN_x phase could be obtained from this material by a post-deposition thermal anneal at 850 °C [20]. From the aforementioned

results it is clear that plasma-assisted ALD can yield different TaN_x compositions which are determined by the plasma conditions and gas mixtures used. Plasma-assisted ALD provides therefore additional freedom to tailor the deposition process and the resulting TaN_x film properties to order. However, comprehensive studies on the influence of different plasma conditions and different gas mixtures on the TaN_x properties are still lacking.

Obviously, accurate and sensitive diagnostics to characterize the film growth process and the resulting material properties are essential for the development of suitable TaN_x ALD processes. In particular *in situ* diagnostics are generally preferred as they can return immediate information on the process and films deposited while they can also be used for online process control. In previous work, we introduced spectroscopic ellipsometry (SE) for an *in situ* study of remote plasma ALD of conductive TiN films [21]. It was demonstrated that SE is a powerful tool to investigate ALD processes. It yields thickness information which can for example be used to study the growth rate per cycle, nucleation effects, and fast ALD cycle optimization. Moreover, it also gives insight into the material properties. For example, for conductive materials information on the electric film properties such as resistivity and electron mean free path can be extracted during the deposition process [21]. This kind of information has recently also been extracted by SE for sputtered TaN_x films as reported by Aoudi *et al.* [22] and Mistrik *et al.* [23]. The plasma-assisted ALD process also yields the possibility to use plasma-related diagnostics during the plasma exposure step. In our previous work on plasma-assisted ALD of Al_2O_3 from a metal-organic precursor and O_2 plasma, we showed that optical emission spectroscopy can yield information on the ALD reaction mechanisms and the timing of the plasma step [24]. Evidently, similar insight can be expected for plasma-assisted ALD for metal nitrides.

In this article, we report on the plasma-assisted atomic layer deposition (ALD) process of TaN_x films from PDMAT precursor and different remote plasma conditions. Whereas in PVD processes the TaN_x film properties can be tuned by controlling the N_2 pressure and deposition temperature [14], we will show that a good control over TaN_x properties can be achieved in the plasma-assisted ALD process using different plasma gas compositions (H_2 , H_2 - N_2 mixtures, and NH_3) and plasma exposure times. The influence of the plasma exposure time is particularly interesting in this respect since the continuous interaction between the plasma radicals and the growing film can be used to alter the material properties even after completed removal of the precursor ligands, whereas in thermal ALD

the material properties depend solely on the chemical reactions between the precursors and reactive surface groups. For the different TaN_x films synthesized, the material properties were determined using various *ex situ* analysis techniques whereas spectroscopic ellipsometry is used to monitor the film growth *in situ*. It is demonstrated that different TaN_x phases can be distinguished during the deposition process by measuring the dielectric function of the films by *in situ* SE. Furthermore, optical emission spectroscopy (OES) is introduced during plasma-assisted ALD of TaN_x to reveal information on the ALD reactions and to determine the required dosing of precursor and plasma step to achieve ALD growth saturation. First, the experimental configuration and ellipsometry data analysis procedure will be described in detail in Secs. II and III, respectively. In Sec. IV, the ALD film growth and the material properties of the TaN_x films for the different deposition conditions, such as deposition temperature, plasma exposure time, and plasma gas composition, will be presented and discussed. Process characterization by *in situ* SE and OES during the ALD process is also described in Sec. IV. The conclusions of this work are summarized in Sec. V.

II Experimental details

A. Remote plasma ALD reactor and process conditions

The experimental setup is schematically shown in Fig. 2.1(a) and consists of a vacuum chamber equipped with a remote plasma source and a precursor dosing system. The configuration is similar to the setup used for the TiN deposition described in previous work [21, 25] and, therefore mainly the aspects relevant for remote plasma ALD of TaN_x films will be briefly discussed.

The solid metal-organic precursor Ta[N(CH₃)₂]₅ (PDMAT, pentakis-(dimethylamino)tantalum, Sigma-Aldrich, >99.99% purity) was contained in a stainless steel bubbler heated to 75 °C to reach adequate vapor pressure. Ar was used as carrier gas (>99.999% purity, working pressure of ~30 mTorr) and the flow was controlled using a leak valve upstream. This Ar flow is also used for purging the chamber after precursor dosing using a divert line. In addition, the chamber was pumped down (<10⁻⁴ Torr) after purging to remove any remaining gaseous precursor and reaction by-products before plasma excitation. The PDMAT gas lines and vacuum chamber were heated (>80 °C) by heating tape to prevent precursor condensation during transport to the substrate. To avoid film deposition in the

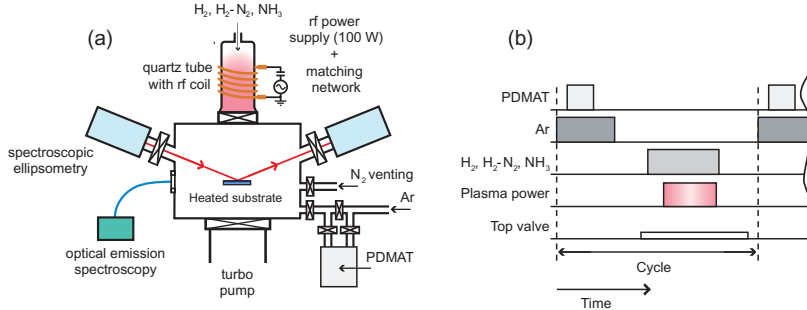


Figure 2.1: (a) Schematic representation of the remote plasma atomic layer deposition (ALD) setup for TaN_x deposition. The optical access on the reactor chamber for *in situ* spectroscopic ellipsometry and optical emission spectroscopy is indicated. (b) Typical timing scheme for remote plasma ALD of TaN_x showing the PDMAT dosing, the Ar carrier and purge gas, the plasma gas (H₂, H₂-N₂ or NH₃), and the switching of the plasma power and the top valve between plasma source and reactor chamber.

plasma source, the top valve positioned between the source and chamber was closed during the PDMAT dosing.

The ALD reaction was completed by exposing the substrate to a plasma generated in the remote inductively coupled plasma (ICP) source. The radio frequency power coupling (100 W) was optimized by impedance matching [25]. Different gases [H₂, N₂ (purities >99.999%) and NH₃ purity >99.995%)] and their mixtures can be fed into the plasma source to investigate the effect of the plasma gas composition on the TaN_x material properties. The plasma gas pressure was set to 7.5 mTorr for all depositions. A typical ALD cycle used for the deposition of TaN_x films is represented in Fig. 2.1(b) and the switching on/off of the relevant valves and gas flows is indicated. The TaN_x films were deposited on resistively heated substrates in the temperature window of 150 to 250 °C. The silicon substrates [p-type Si (10–30 μΩ cm)] did not undergo additional cleaning steps and were covered with a 1–2 nm native oxide layer. Typically a 2 inch substrate size was used, but a 4 inch substrate holder could be used for deposition on larger sized substrates.

B. *In situ* diagnostics

The ALD film growth was monitored by *in situ* spectroscopic ellipsometry (SE) using the two optical viewports on the chamber that allow for SE measurements under a fixed angle of incidence of 68° to the substrate nor-

mal (Fig. 2.1). Pneumatic gate valves separated the vacuum chamber and the viewports to prevent film deposition on the optical ports. A visible and near-infrared (NIR) rotating compensator ellipsometer (J.A. Woollam, Inc., M2000U) was used for the *in situ* SE measurements such that the TaN_x dielectric function could be determined in the photon energy range 0.75–5.0 eV. In addition, a visible and ultraviolet (UV) extended (J.A. Woollam, Inc., M2000D, 1.2–6.5 eV) ellipsometer was used *ex situ* to probe the dielectric function deeper into the ultraviolet. The different parametrizations used to model the conductive and high-resistivity TaN_x films will be described in more detail in Sec. III.

An optical viewport on the side of the chamber allowed for optical emission spectroscopy (OES) to study the emission of excited species during the plasma step in the ALD cycle. An Ocean Optics USB2000 spectrometer was used with a wavelength detection range of 250–870 nm and with a resolution of approximately 1 nm. The light was collected by an optical fiber placed in front of the side viewport of the reactor chamber and was dispersed via a fixed grating across a linear CCD array detector. The typical integration time used was 100 ms.

C. *Ex situ* material analysis

Electrical resistivity measurements were carried out at room temperature using a Signatone four-point probe (FPP) in combination with a Keithley 2400 Sourcemeter acting both as current source and as a voltage meter. The sheet resistance was determined from the slope of the I – V curve and the resistivity was obtained after multiplication by the film thickness deduced from the SE measurements. The film composition was determined from Rutherford backscattering spectroscopy (RBS) and elastic recoil detection (ERD) using 2 MeV ⁴He⁺ ions. The ion beam was targeted at the surface at two different angles (–80° and –10°) for every sample to get improved sensitivity for both the heavy and light elements, while it also allowed for depth profiling of the TaN_x layer. The RBS and ERD data were modeled using the RUMP program [26]. X-ray diffraction (XRD) was performed to determine the film microstructure using a Philips X’Pert MPD diffractometer equipped with a Cu K_α source (1.54 Å radiation). To reduce the measurement time a Philips X’Celerator detector was used and to increase the surface sensitivity the measurements were performed under a grazing angle of incidence. The thickness and mass density were also determined from x-ray reflectometry (XRR) measurements carried out on a Bruker D8 Advance x-ray diffractometer.

III Spectroscopic ellipsometry on TaN_x films

A. Data acquisition and optical model

Spectroscopic ellipsometry data can be acquired *in situ* after every ALD cycle after opening the gate valves to the light source and detector, but typically data were obtained after 10 completed cycles. A high signal-to-noise ratio was obtained by averaging each SE measurement over 400 data acquisitions, which led to a measurement time of approximately 45 seconds. After the measurement, the gate valves were closed and the deposition process continued. The WVASE32 software from J.A. Woollam was used to analyze ellipsometry data [27]. In WVASE32, *in situ* ellipsometry data from the NIR-extended ellipsometer can be combined with *ex situ* data obtained on the same film by the UV-extended ellipsometer. This makes it possible to determine the dielectric functions of the different TaN_x films over the photon energy range from 0.75 to 6.5 eV.

The ellipsometry data can be expressed in terms of the pseudo-dielectric function $\langle \varepsilon \rangle$, which is represented in a real $\langle \varepsilon_1 \rangle$ and imaginary $\langle \varepsilon_2 \rangle$ part. From model-based analysis of the ellipsometry data, the thickness of the film and the optical constants of the TaN_x film can be extracted. Prior to the film deposition, the pseudo-dielectric function of the substrate was determined in order to isolate the starting substrate from the deposited TaN_x film. The Si substrates with native oxide were modeled by a semi-infinite Si layer of which the optical constants were obtained by a point-to-point fit and a top oxide layer of ~ 1.5 nm as described by the Cauchy relation. The TaN_x film deposited was modeled by adding a layer on top of the substrate and various parameterizations were used to describe the different TaN_x optical properties. Assumptions within this approach were that the deposition process does not affect the substrate properties and that a surface roughness layer can be neglected, which was corroborated by the small surface roughness (< 0.3 nm) measured by atomic force microscopy. More details on the ellipsometer configuration and measurement procedure during remote plasma ALD can be found elsewhere [21].

B. Dielectric function of TaN_x films

The dielectric functions of the conductive TaN_{*x*,*x*≤1} phase and semiconductive Ta₃N₅ phase are quite dissimilar and this fact lies at the basis for the distinction between the different TaN_x phases by SE. The parameterizations used to describe the dielectric functions of these TaN_x films will be

introduced below. A comparison between typical parameters derived from the SE data and *ex situ* analysis is presented in the subsequent section.

1. Conductive TaN_x films

The low-resistivity TaN_{x, x≤1} films were described by a Drude-Lorentz oscillator parametrization. The Drude oscillator accounts for the intraband absorption by conduction electrons and contains information on the metallic properties of the film. The Lorentz oscillators account for the interband absorption by bound electrons. Following the literature on PVD TaN films [22, 23], we used a combination of one Drude and two Lorentz oscillators to describe the dielectric function of the conductive TaN_x deposited by ALD:

$$\varepsilon(\omega) = \varepsilon_\infty - \frac{\omega_{\text{pu}}^2}{\omega^2 - i\Gamma_D\omega} + \sum_{j=1}^2 \frac{f_j\omega_{0j}^2}{\omega_{0j}^2 - \omega^2 + i\gamma_j\omega}. \quad (2.1)$$

In Eq. 2.1, ε_∞ is equal or larger than unity to compensate for the contribution of higher-energy transitions that are not taken into account by the Lorentz terms. The Drude term is characterized by the unscreened plasma energy $\hbar\omega_{\text{pu}}$ and the damping factor Γ_D . The Lorentz oscillators were located at energy position $\hbar\omega_{0j}$, with strength f_j , and damping factor γ_j . For TaN_x, the two Lorentz oscillators account for interband absorptions around 2.2 and 6.4 eV [22, 23].

The imaginary (ε_2) part of the dielectric function for a typical TaN_x film with a low resistivity is shown in Fig. 2.2(a) and the contributions of the Drude and Lorentz oscillators are indicated. In particular, the NIR extension of the spectroscopic ellipsometer aids to distinguish the Drude absorption from the strong Lorentz oscillator around 2.2 eV, while the second Lorentz oscillator is determined more accurately using the UV extended SE.

Several film properties, such as electron density, electrical resistivity, electron mean free path, and mass density, can be calculated from the Drude absorption as was shown for Drude parameters obtained for TiN films [21]. However, the data modeling of the thin TaN_x films revealed that the Drude amplitude and broadening are correlated, which is caused by the large Lorentz oscillator around 2.2 eV. Consequently, only the ratio of the Drude parameters could be uniquely determined. Since the electrical

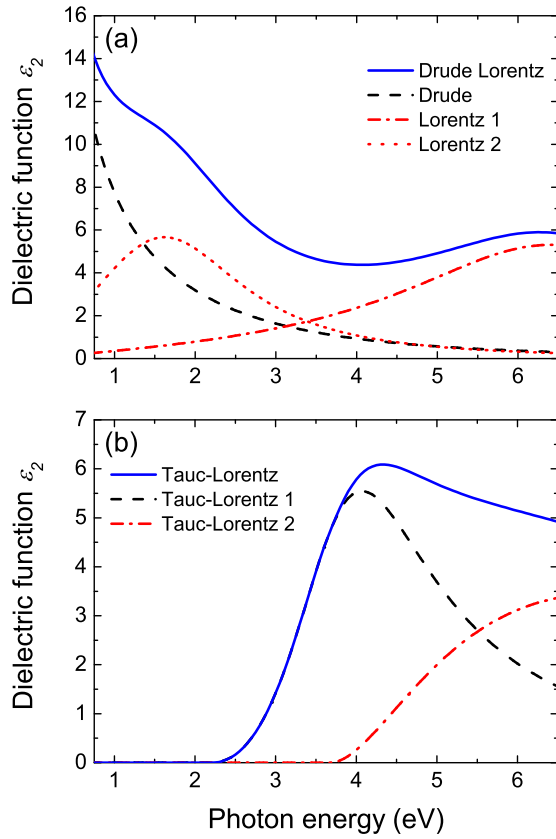


Figure 2.2: The imaginary part (ϵ_2) of the dielectric function of (a) a conductive, cubic $\text{TaN}_{x,x \leq 1}$ film and (b) a semiconductive Ta_3N_5 film as deduced from spectroscopic ellipsometry measurements. The dielectric functions are parametrized using (a) a Drude and two Lorentz oscillators and (b) using two Tauc-Lorentz oscillators. The photon energy ranges from the near infrared (0.75 eV) to the ultraviolet (6.5 eV). The conductive $\text{TaN}_{x,x \leq 1}$ film was deposited using 10 s H_2 plasma in the ALD cycle, while the Ta_3N_5 film was deposited using 10 s NH_3 plasma.

resistivity is defined by the ratio of Drude fit parameters [21, 28],

$$\rho = \left(\frac{1}{\varepsilon_0} \right) \frac{\Gamma_D}{\omega_{\text{pu}}^2}, \quad (2.2)$$

where ε_0 is the permittivity of free space, the electrical resistivity can be unambiguously determined from SE measurements.

2. Semiconductive TaN_x films

The dielectric function of amorphous semiconductors and insulators is often described by the Tauc-Lorentz model [29–31]. When multiple transitions are possible in the material, additional Tauc-Lorentz oscillators can be added to the parametrization [32]. To model the high-resistive Ta₃N₅ phase, we used a double Tauc-Lorentz model with the imaginary part (ε_2) of the dielectric function given by:

$$\begin{aligned} \varepsilon_2(E) &= \sum_{j=1}^2 \frac{A_j E_{0j} \Gamma_j (E - E_{gj})^2}{(E^2 - E_{0j}^2)^2 + \Gamma_j^2 E^2} \frac{1}{E}, & E > E_{gj}, \\ &= 0, & E \leq E_{gj}. \end{aligned} \quad (2.3)$$

In Eq. 2.3, E_{gj} is the band gap, E_{0j} the peak transition energy, Γ_j the broadening parameter, and A_j represents the optical transition matrix elements [31]. The real part of the dielectric function (ε_1) can be obtained by the Kramers-Kronig integration of ε_2 [29]. The imaginary part of the dielectric function for a typical Ta₃N₅ film is shown in Fig. 2.2(b) and both Tauc-Lorentz oscillators are indicated. The first oscillator defines the position of the optical band gap of the Ta₃N₅ film, while the second oscillator accounts for absorption above the absorption edge, as was also reported for the modeling of Ta₂O₅ films [32, 33]. For a Ta₃N_{4.6} film that was deposited using a H₂-N₂ plasma, an additional Lorentz oscillator was required to account for absorption below the band gap as will be presented in Sec. IV D.

C. Typical SE results and comparison with *ex situ* film analysis

A typical example of the film thickness as a function of the number of ALD cycles as obtained from the SE measurements is shown in Fig. 2.3. Data are presented for both a conductive TaN_{*x,x*≤1} and highly-resistive Ta₃N₅ film. The ALD process was halted each time after a certain amount of

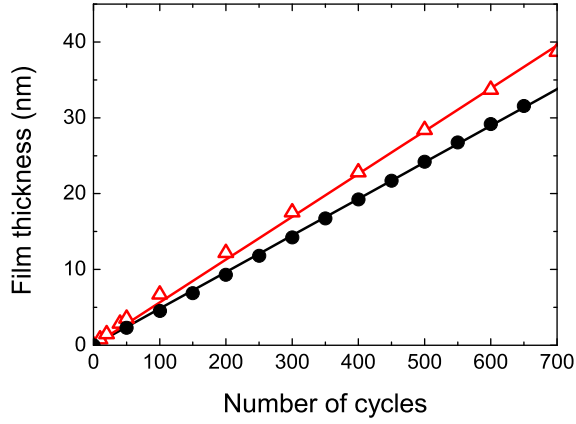


Figure 2.3: Film thickness as a function of number of remote plasma ALD cycles shown for the growth of cubic TaN_{*x,x* ≤ 1} (closed symbols) and Ta₃N₅ (open symbols) as deduced from *in situ* spectroscopic ellipsometry measurements. The solid lines are linear fits to the data. The cubic TaN_{*x,x* ≤ 1} film was deposited using 10 s of H₂ plasma in the ALD cycle, while the Ta₃N₅ film was deposited using 10 s of NH₃ plasma.

cycles to acquire SE data and to calculate the film thickness employing the appropriate parameterization. The linear growth behavior of the plasma-assisted ALD process can clearly be observed in Fig. 2.3 for both TaN_{*x*} phases. The final film thickness deduced from the SE modeling was found to be in good agreement with the thickness determined by XRR (see also Table 2.1). The growth rates were calculated from a linear fit to the data and resulted in 0.048 ± 0.005 nm/cycle and 0.056 ± 0.005 nm/cycle for the TaN_{*x,x* ≤ 1} and Ta₃N₅ films, respectively. Note that Fig. 2.3 also reveals that the thickness of the TaN_{*x*} films deposited from PDMAT precursor is immediately linear at the onset of growth. Therefore, a distinct nucleation delay was absent as was observed before during the plasma-assisted ALD of TiN using the metal-halide TiCl₄ precursor and a H₂-N₂ plasma [21].

Since data can be obtained after every cycle, *in situ* SE allows for a fast determination of the ALD saturation curves. For different ALD conditions (as set by the combination of precursor dosing, plasma exposure time, and substrate temperature), the growth rate for each condition was calculated from the increase in film thickness determined over 80 cycles by taking SE measurements after every 10 ALD cycles. By a systematic variation of the process parameters, the ALD saturation curves were determined from a single deposition run of one sample. Such saturation curves will

be discussed in Sec. IV, but here it is already mentioned that the growth rates were found to be similar to the growth rates determined from separate depositions of thick films (~ 30 nm) at constant process parameters.

The resistivity determined from the SE data using the Drude-Lorentz model can be compared to the resistivity determined by *ex situ* four-point probe (FPP) measurements. As the FPP yields the resistivity of the TaN_x films at room temperature, first the temperature coefficient of resistivity (TCR) of the TaN_x film was determined by *in situ* SE. The change in resistivity as monitored upon cooling down the substrate in the vacuum setup revealed a small TCR of -30 ± 30 ppm/K for the TaN_x films. Baba *et al.* reported a similar TCR value of -80 ± 30 ppm/K which was relatively independent of the TaN_x composition [34]. Consequently, within the experimental uncertainty, the resistivity obtained at deposition temperature by *in situ* SE can be directly compared to the room temperature resistivity obtained by *ex situ* FPP. It was found that resistivity values obtained by SE and FPP are in relatively good agreement with each other for plasma exposure times longer than 10 s (see Table 2.1). Only one data point (3 s H₂ plasma) showed a clear discrepancy but as will be discussed in Sec. IV C, the corresponding sample showed a deviating behavior compared to the rest of the sample set, possibly due to the presence of Ta–C bonds. The SE data for this particular sample were also difficult to fit with the Drude-Lorentz model. Finally, it can be concluded that the generally good agreement between the thickness and resistivity values as extracted from SE with the results of the *ex situ* film analysis validates the SE data interpretation and modeling employed.

IV TaN_x film growth and material properties

The TaN_x films were deposited by remote plasma ALD under various process conditions. In particular, the plasma exposure time, the plasma gas composition, and the deposition temperature were varied. Table 2.1 summarizes the process conditions and resulting material properties, i.e., film thickness, film composition, electrical resistivity, and mass density. In the following section, first the saturation in growth rate for the various ALD process parameters will be addressed and, subsequently, the material properties will be discussed. It will be shown that the TaN_x properties can be controlled by the plasma exposure time and by the plasma gas composition. Finally, the characterization of the ALD process by optical emission spectroscopy during the plasma step will be presented.

Table 2.1: Material properties of TaN_x films deposited at various plasma conditions, substrate temperatures, and plasma gas mixtures. *In situ* spectroscopic ellipsometry (SE), x-ray reflectometry (XRR), Rutherford backscattering spectroscopy (RBS), and four-point probe (FPP) were used to determine the material properties. The typical experimental errors are shown in each column; a dash means “not measured”.

Deposition conditions				Material properties								
Plasma condition (s)	PDMAT dosing (s)	Deposition temperature (°C)	Number of cycles	Thickness (nm)		Film composition		Mass density (g cm ⁻³)		Resistivity (μΩ cm)		
				SE	XRR	[N]/[Ta] (at.%)	[O] (at.%)	[C] (at.%)	RBS	XRR	SE	FPP
H ₂												
1	4	225	1400	36.9±0.5	—	—	—	—	—	7500±100	3.3×10 ⁴	—
3	4	225	700	26.4	—	0.76	15	10	9.1±0.5	1740	48±10 ^a	—
3	4	225	250	9.5	—	—	—	—	—	2600	3400±100	—
10	5	150	650	30.9	30.5±0.3	0.55	15	10	10.5	10.5±0.5	1000	1300
10	4	225	650	31.6	—	0.49	12	<2	10.4	12.0	950	1200
10	4	225	2000	91.1	93.9	—	—	—	—	11.4	600	700
10	5	250	700	35.6	35.0	0.73	14	17	10.8	11.3	580	650
30	8	225	500	28.1	—	0.45	7	12	12.1	—	390	380
H ₂ -N ₂												
5s (98:2)	4	225	1000	51.6	—	1.0	15	<2	8.9	—	3350	1.1×10 ⁴
10s (1:1)	4	225	1300	68.1	67.4	1.5	8	<2 ^b	9.8	10.9	—	≫5×10 ^{4c}
NH ₃												
10	5	225	900	49.0	49.6	—	—	—	—	9.4	—	≫5×10 ^{4c}

^aTypical error for this film.

^bElastic recoil detection revealed a H concentration of 9 at. %.

^cExceeding FPP measurement range.

A. Growth rate of remote plasma ALD process

The saturation of the growth rate per cycle as being typical for ALD is investigated by varying the process parameters, i.e., PDMAT dosing time, plasma exposure time, and deposition temperature. The results are presented in Fig. 2.4 for TaN_{x, x≤1} films deposited with a H₂ plasma. During the variation of the PDMAT dosing time, the H₂ plasma exposure time was set to 10 s and the deposition temperature was 225 °C. A clear saturation in growth rate as a function of precursor dosing is observed in Fig. 2.4(a) and the growth rate saturated at 0.045 ± 0.004 nm/cycle for PDMAT dosing times exceeding 3 s. As shown in Fig. 2.4(a), the data can be fitted with a single exponential function describing the expected saturation behavior during precursor absorption [35].

A similar experiment was carried out for the H₂ plasma exposure time: the PDMAT dosing time was set to 4 s and the temperature to 225 °C, while the plasma exposure time was varied. Figure 2.4(b) shows a so-called “soft” saturation in growth rate with H₂ plasma exposure time. The data points can be fitted using an exponential function with two time constants. The fast initial increase in growth rate can be attributed to the ligand removal from the surface, whereas the slow increase in growth rate (for plasma exposure time >3 s) can be related to a change in TaN_x composition (cf. Table 2.1) with increasing plasma exposure time. This effect will be discussed in more detail in the Sec. IV B.

Using a PDMAT dosing of 4 s and H₂ plasma exposure time of 10 s, the temperature dependence of the growth rate was studied for deposition temperatures in the range of 150 to 250 °C. Fig. 2.4(c) shows that the growth rate remained constant at 0.050 ± 0.004 nm/cycle within the temperature window studied.

The saturated growth rate per cycle can be compared to the results reported by Kim and coworkers obtained with a similar remote plasma ALD process [4, 36]. They calculated the growth rate (0.03 nm/cycle) from RBS measurements using the bulk mass density of cubic TaN (15.9 g cm⁻³) [37], which is expected to be a higher limit for thin TaN_x films deposited by ALD. Assuming a similar mass density for their films as obtained by our work (see Table 2.1) leads to growth rates per cycle for their experiments that are in good agreement with our results. Our data do however not show a decrease in growth rate for depositions below 200 °C as reported by Kim *et al.* [4]. This might be attributed to the shorter H₂ plasma exposure time of 5 s in their ALD process. The growth rate for our TaN_{x, x≤1} films is higher than the growth rate of 0.02 nm/cycle reported by Furuya

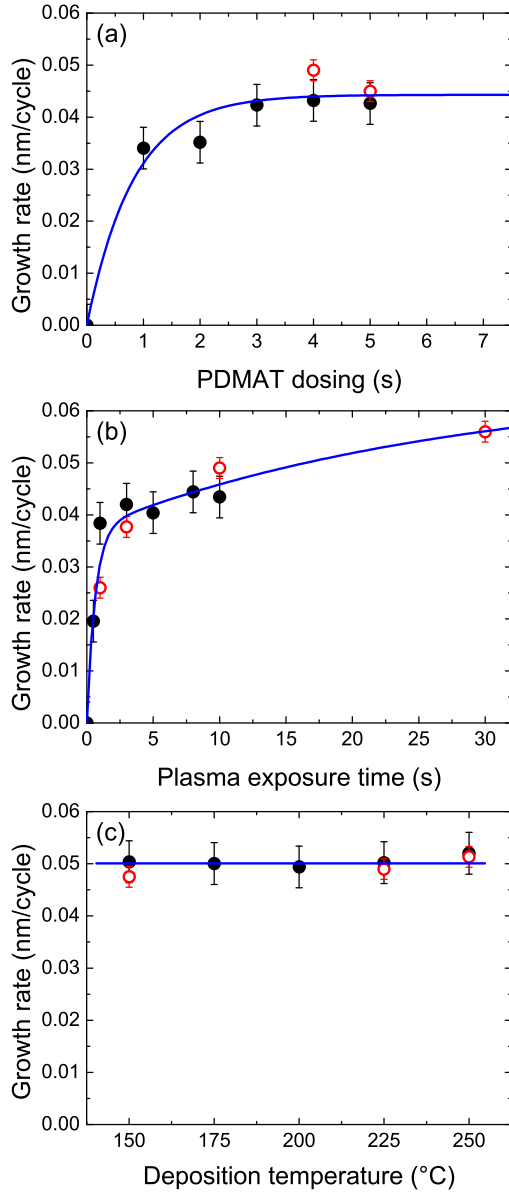


Figure 2.4: Growth rate per cycle of TaN_{*x*,*x* ≤ 1} films as a function of the ALD process parameters; (a) PDMAT dosing time, (b) H₂ plasma exposure time, and (c) deposition temperature. The growth rates are determined by *in situ* spectroscopic ellipsometry by varying the process parameters during one deposition run (closed symbols) and by the deposition of a thick film under constant process conditions (open symbols). The lines in (a) and (b) are exponential fits to the data.

et al., who used PDMAT in combination with a He–H₂ plasma [38]. In a plasma-assisted ALD process using TBTDET precursor and a direct H₂–Ar plasma, Park *et al.* reported a growth rate of 0.06 nm/cycle [9]. Ritala *et al.* reported a growth rate of 0.025 nm/cycle for conductive TaN_x films deposited in a thermal ALD process from TaCl₅ precursor and NH₃ using Zn as an additional reducing agent [10].

B. Influence of the deposition temperature

The influence of the deposition temperature on the material properties is studied for depositions at 150, 225, and 250 °C using 4 s PDMAT dosing and 10 s H₂ plasma exposure in the ALD cycle. As can be seen from Table 2.1, all films have a [N]/[Ta] ratio $x < 1$ with the film composition varying slightly with deposition temperature and x increasing from 0.55 at 150 °C to 0.73 at 250 °C. The main impurities in the film are oxygen and carbon. The O content remains approximately constant at ~14 at. % in the temperature range used. The C content does not show a clear trend with temperature; the low and high temperature depositions had a C content 10 at. %, while the 225 °C deposition resulted in a film with a C content below the detection limit (<2 at. %) of the RBS. Despite the impurity content, the TaN_x films have a high mass density that slightly increased with deposition temperature to 11.3 g cm⁻³. Furthermore, it is observed from SE and FPP measurements that the electrical resistivity decreases for higher deposition temperatures.

The effect of deposition temperature on the microstructure of the TaN_x films is presented in Fig. 2.5. The microstructure was determined by grazing incidence x-ray diffraction for TaN_x films deposited at the aforementioned temperatures. The diffraction spectra show peaks similar to those of a diffraction spectrum of a cubic TaN powder sample indicating that cubic TaN_x films were deposited for deposition temperatures between 150 and 250 °C. Examining the intensities of the diffraction peaks, the films tend to have a small preference for growth along the (200) direction for all deposition temperatures. Figure 2.5 also shows the diffraction spectra of a 91 nm thick TaN_x film deposited at 225 °C and it is clear that the (200) growth direction becomes more preferred for this thicker film. Park *et al.* also reported the growth of cubic TaN_x films by plasma-assisted ALD and observed that the relative intensity of the (200) direction depends on the plasma exposure time in their ALD process [9].

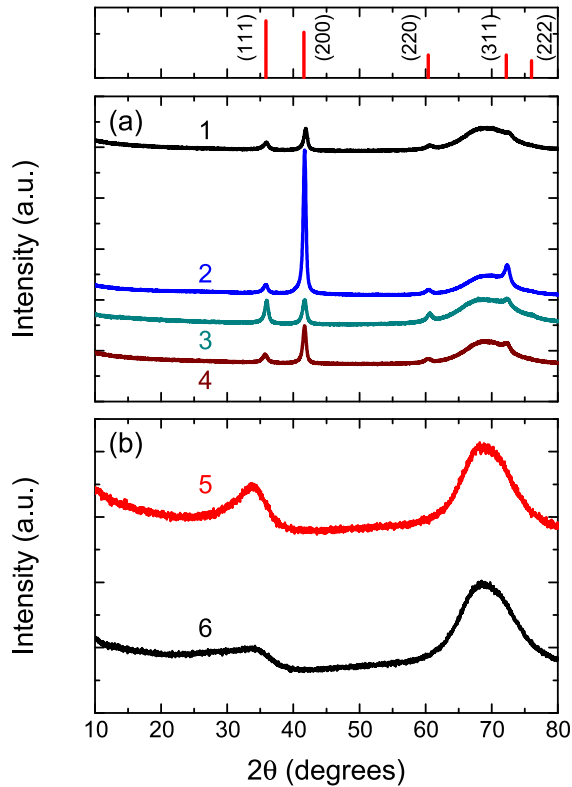


Figure 2.5: Grazing incidence x-ray diffraction spectra of TaN_x films deposited at different substrate temperatures and using different plasma compositions. (a) Cubic TaN_{x, x ≤ 1} films deposited using 10 s H₂ plasma exposure: 1) 31 nm at 150 °C, 2) 94 nm at 225 °C, 3) 30 nm at 225 °C, and 4) 35 nm at 250 °C. (b) Amorphous Ta₃N₅-like films: 5) 68 nm at 225 °C using 10 s H₂-N₂ (1:1) plasma exposure and 6) 49 nm at 225 °C using 10 s NH₃ plasma exposure. The broad peak between 60° and 80° originates from the *c*-Si substrate. The vertical lines in the top graph indicate the typical diffraction spectrum of a cubic TaN powder sample. The data lines are offset vertically for clarity.

C. Influence of the plasma exposure time

The influence of plasma exposure time on the film composition and electrical properties was studied for cubic, low-resistivity TaN_{*x,x*≤1} films that were deposited employing different H₂ plasma exposure times (1, 3, 10, and 30 s) in the plasma-assisted ALD cycle. Table 2.1 shows that the [N]/[Ta] ratio as determined by RBS measurements decreases for longer H₂ plasma exposure times and indicates that the TaN_{*x,x*≤1} films become more Ta-rich ($x = 0.45$ for 30 s H₂ plasma). The O content of the films decreased with plasma exposure time (7 at. % O for 30 s H₂ plasma), while the C content was approximately 10 at. % (except for the 10 s H₂ plasma deposited film for which the RBS measurement was explicitly verified). The mass density of the films as determined by RBS increased with plasma exposure time and a density of 12.1 g cm⁻³ was obtained for the film deposited using 30 s H₂ plasma in the ALD cycle. The mass density of 12.1 g cm⁻³ is the highest reported for an ALD process of TaN_{*x*} to date, but it is still somewhat lower than the cubic TaN bulk mass density of 15.9 g cm⁻³ [37]. Although still relatively high, the impurity content for the TaN_{*x,x*≤1} films is lower than the O and C content of 14–15 at. % reported by Kim *et al.* [4] and the C content of 20 at. % reported by Park *et al.* [9]. The C content in the films originates from the PDMAT ligands and could not effectively be reduced by prolonged plasma exposure time as indicated by our experiments. Showing a different trend than the N and O content with H₂ plasma exposure time, the constant C content could be an indication of a re-deposition process involving ligand surface reaction products dissociated by the plasma after being released from the surface. The O content in the films can originate from several sources. The O content can be caused by a slightly oxidized precursor in the bubbler due to the precursor synthesis process or handling or due to small oxygen impurities in the Ar purge gas. It is also reported that the TaN_{*x,x*≤1} films are sensitive to post-process oxidation and the O content can result from exposure of the films to the ambient [39, 40].

The influence of the plasma exposure time on the film composition was also observed by the change in electrical resistivity of the films as determined by *in situ* SE (Eq. 2.2) and *ex situ* four-point probe measurements. Figure 2.6 shows the electrical resistivity of ~30 nm thick TaN_{*x*} films as a function of H₂ plasma exposure time. The electrical resistivity decreased when going to longer H₂ plasma exposure times in the ALD cycle. Using 30 s H₂ plasma in the ALD cycle resulted in a resistivity as low as 380 μΩ cm which is similar to the best values reported in the literature (350–400 μΩ cm) [4, 9]. Park *et al.* reported that the decrease in resistivity

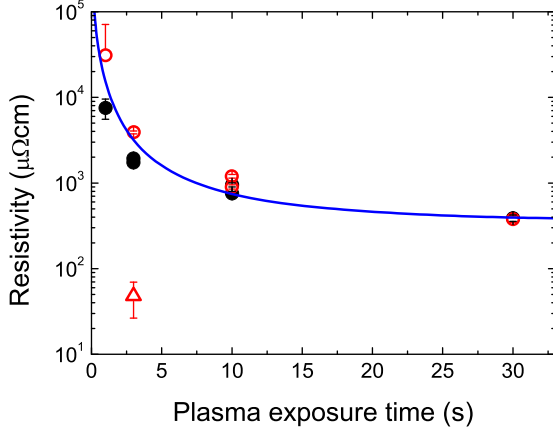


Figure 2.6: Resistivity of TaN_{*x,x*≤1} films with a ~30 nm thickness deposited by remote plasma ALD using different H₂ plasma exposure times within the cycle. The resistivity is determined from *in situ* SE (closed symbols) and *ex situ* FPP measurements (open symbols). The line serves as a guide to the eye. The low resistivity TaN_{*x,x*≤1} film deposited using 3 s H₂ plasma in the ALD cycle has been indicated separately (open triangle).

relates to an increase in mass density and degree of crystallization of the TaN_{*x*} films [9].

We note that one data point (3 s H₂ plasma) does not follow the general trend and the corresponding film was specifically investigated for its low resistivity (FPP: 48 μΩ cm). The resistivity of this film was stable and not affected by storage of the sample under ambient conditions, as observed from repetitive FPP measurements over a longer time span. X-ray photoelectron spectroscopy (XPS) revealed the presence of Ta–C bonds in the film, which could account for the low electrical resistivity. This very low resistivity value could not be returned from the Drude-Lorentz model which gave a poor fit, but the SE data analysis might require a more dedicated description to account for the highly conductive Ta–C bonding [41].

D. Influence of the plasma gas composition

The plasma gas composition is an additional parameter that can be used to tune the material composition of the TaN_{*x*} films. In the previous section it was shown that the use of a H₂ plasma in the ALD cycle resulted in the deposition of conductive TaN_{*x,x*≤1} films. Adding a small fraction of N₂ gas (2%) to the H₂ plasma resulted in a strong increase of the nitrogen content

in the film as shown in Table 2.1. This resulting film contained oxygen impurities (15 at. %), but the carbon content was below the detection limit of the RBS. The SE modeling and FPP measurements showed an increased electrical resistivity when admixing only 2% N₂ to the H₂ plasma and accordingly, a different conductive phase of TaN_x was deposited using this plasma condition. It was observed that this film contained negligible C impurities (<2 at. %). Using a higher N₂ fraction in a H₂-N₂ (1:1) plasma or using a NH₃ plasma in the ALD cycle resulted in a film composition close to the Ta₃N₅ phase. The H₂-N₂ deposited film had a negligible carbon content and 9 at. % of hydrogen as determined by elastic recoil detection. The films had a very high-resistivity that was out of the measurement range of the FPP. The XRR measurements showed that the mass density of these films is close to the bulk mass density of Ta₃N₅ of 9.9 g cm⁻³ [37]. Figure 2.5 shows the microstructure of these high-resistivity films. Both films are amorphous, although the H₂-N₂ plasma deposited film seems to contain some nanocrystalline fraction. The microstructure of the film deposited with the NH₃ plasma was in good agreement with the powder spectrum of amorphous Ta₃N₅ [42]. For several thermal ALD processes of Ta₃N₅ films reported in the literature, also the amorphous crystal structure was observed [4, 9, 20, 43]. It is obvious from aforementioned results that (a small fraction of) N-containing plasmas (H₂-N₂ or NH₃) strongly influences the conductivity properties of the TaN_x films and strongly reduces the C content.

The change in film composition (see Table 2.1) and TaN_x phase when varying the plasma conditions can also be observed by *in situ* SE when studying the dielectric functions of the deposited films. Figure 2.7 shows the imaginary part (ϵ_2) of the dielectric function of the TaN_x films for the various plasma conditions used. Admixing little N₂ to the plasma increased the film resistivity, which is clearly visible from the diminishing of the Drude absorption in the infrared part of the spectrum. This conductive film could still be parametrized by the Drude-Lorentz model. However, for the film deposited using a H₂-N₂ (1:1) plasma this was no longer the case. The dielectric function of this film required a double Tauc-Lorentz parametrization, which was extended with an additional Lorentz oscillator to account for small absorption below the band gap of ~1.9 eV. The film deposited with the NH₃ plasma shows negligible absorption below the band gap of ~2.5 eV and could be modeled by the double Tauc-Lorentz model. The optical band gap of the Ta₃N₅ films is in the range of 2.1–2.5 eV as reported in the literature [20, 44].

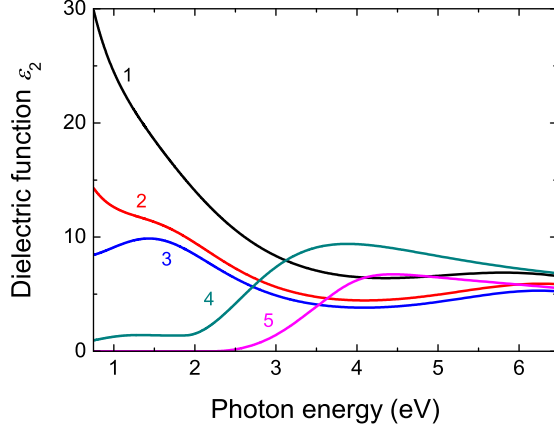


Figure 2.7: The imaginary part (ε_2) of the dielectric function of TaN_x films deposited under various plasma conditions in the ALD cycle and as determined by *in situ* spectroscopic ellipsometry: 1) 30 s H₂ plasma ($x = 0.44$), 2) 10 s H₂ plasma ($x = 0.49$), 3) 5 s H₂-N₂ (98:2) plasma ($x = 1.0$), 4) 10 s H₂-N₂ (1:1) plasma ($x = 1.55$), and 5) 10 s NH₃ plasma ($x = 1.67$). The ratio $x = [\text{N}]/[\text{Ta}]$ of the TaN_x films was determined by RBS analysis.

E. Remote plasma ALD studied by OES

The saturation in ALD growth rate with precursor dosing and plasma exposure time can also be studied by a careful examination of the plasma emission using optical emission spectroscopy (OES) during the ALD cycle. The plasma emission signal combines contributions from the plasma gas excitation and the interaction of the plasma with the reactor wall leading to possible plasma excitation of (fragmented) surface reactions products. The OES measurements were carried out with the substrate and chamber walls heated to 150 °C to ensure that all surfaces contribute in a similar way to the ALD reaction. As a result the film growth is representative for TaN_x growth at 150 °C (Table 2.1).

An emission spectrum of a steady-state H₂ plasma under non-ALD conditions, but as typically used in the plasma-assisted ALD cycle of TaN_x is shown in Fig. 2.8(a). Clearly the atomic hydrogen emission from the Balmer series, H_α (656.5 nm) and H_β (485.6 nm), indicates the presence of H radicals. Molecular hydrogen emission from the $d^3\Pi_u \rightarrow a^3\Sigma_g$ transition, the so-called Fulcher bands (590–640 nm), indicates excited H₂.

The emission spectrum recorded for the H₂ plasma during the plasma-assisted ALD cycle appeared to be slightly different when compared to the

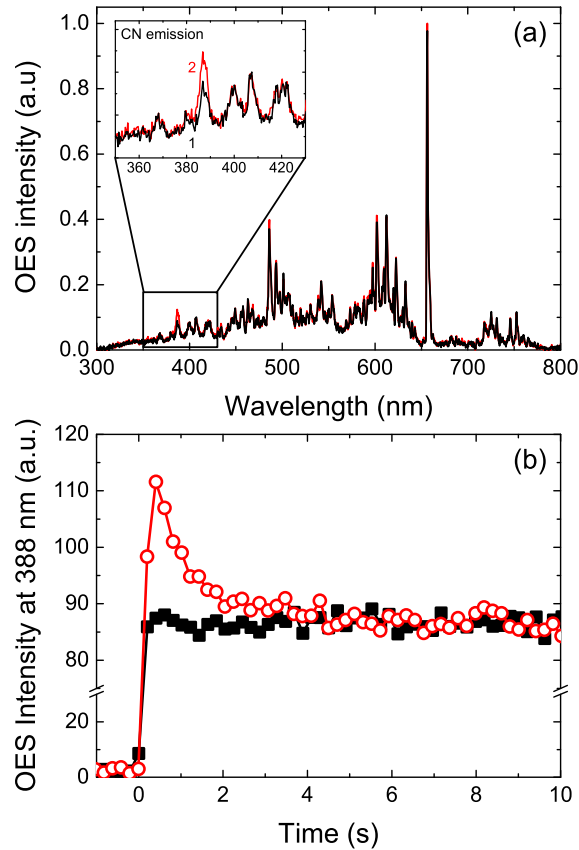


Figure 2.8: Optical emission spectroscopy (OES) during remote plasma ALD: (a) emission from 1) a regular H₂ plasma and 2) a H₂ plasma ignited after a preceding PDMAT dose as recorded in the first 400 ms after the plasma strike. The inset shows a magnification of the region around 400 nm. (b) Time-resolved OES at 388 nm during the H₂ plasma step for an ALD cycle with (open symbols) and without (closed symbols) PDMAT dosing. During the OES measurements the chamber was wall-heated to 150 °C.

emission spectrum of the H₂ plasma under non-ALD conditions. Careful examination of the plasma emission recorded during the first 400 ms after the plasma strike in the ALD cycle, showed an extra emission peak at 388 nm [Fig. 2.8(a)]. This additional emission peak decayed within the plasma exposure step and after a certain time the plasma emission spectrum was similar to that of a H₂ plasma under non-ALD conditions. To further elucidate, Fig. 2.8(b) shows the intensity of the emission at 388 nm during the 10 s of H₂ plasma exposure in the ALD cycle. In this figure, the emission at 388 nm is monitored with and without PDMAT dosing in the ALD cycle to isolate the effect of PDMAT. The figure shows that a certain level of emission at 388 nm was always observed in the H₂ plasma caused by the broad emission of H₂ molecules [Fig. 2.8(a)]. However, an increased emission level was present after PDMAT dosing in the ALD cycle, and can be attributed to the dimethylamino ligand removal from the surface by the plasma species. The increased emission level at 388 nm reveals therefore information on the dynamics of the reaction. The emission at 388 nm can be assigned to excited C≡N species (Violet system $B^2\Sigma^-X^2\Sigma$) [45], which can be created in the plasma by excitation reactions involving the dimethylamino ligand species. The presence of C≡N emission during H₂ plasma ALD of TaN_x strongly suggests that Ta–N bonds of the adsorbed PDMAT species are broken by the incoming H radicals, which appears to be an essential step in reducing the oxidation state of the adsorbed Ta atoms in order to deposit a conductive TaN_x film. Furthermore, the time decay of the intensity of the C≡N emission can be directly related to the self-limiting surface reactions during the plasma step and suggests virtually complete removal of the dimethylamino ligands from the surface after ~6 s of H₂ plasma exposure at a deposition temperature of 150 °C (and in good agreement with Fig. 2.4(b) for a pure H₂ plasma).

Since the C≡N emission in the plasma originates from the plasma reaction with the surface dimethylamino groups, the amount of C≡N emission that is detected by OES during the plasma step yields information on the amount of PDMAT adsorbed during the precursor step, i.e., the amount of dimethylamino groups on the surface. Therefore, the intensity of C≡N emission in the plasma can also be used to determine whether the PDMAT dosing was sufficient to react with all the available TaN_x surface groups after the plasma exposure. In order to quantify the amount of C≡N emission during the plasma step, the emission is integrated over the first 10 s of the plasma exposure in successive experiments in which the amount of PDMAT dosing was varied. The data are presented for a H₂–N₂ (98:2)

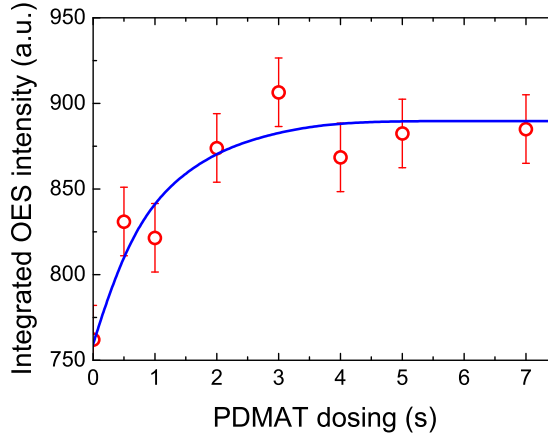


Figure 2.9: The time-integrated intensity of the OES signal during the plasma step plotted as a function of the PDMAT dosing time in the ALD cycle. The OES signal at 388 nm is integrated over the 10 s H₂-N₂ (98:2) plasma exposure time in the ALD cycle. The line serves as a guide to the eye.

plasma which was generally more stable upon plasma strike than a pure H₂ plasma. In Fig. 2.9, the integrated emission is shown as a function of the PDMAT dosing time in the ALD cycle. It is evident that the integrated C≡N emission becomes constant for PDMAT dosing times larger than 3 s. The OES result is in excellent agreement with the SE measurements shown in Fig. 2.4(a) for a pure H₂ plasma. These experiments thereby corroborate the interpretation of the emission spectrum, despite the slightly different deposition temperature and plasma conditions used.

V Conclusions

We have reported on the plasma-assisted ALD process of TaN_x films using metal-organic Ta[N(CH₃)₂]₅ precursor under various remote plasma operating conditions. The versatility of the plasma-assisted ALD process was demonstrated by the level of control of the atomic composition, microstructure, mass density, and electrical properties of the TaN_x films by the plasma condition (H₂, H₂-N₂, and NH₃) applied in the ALD cycle. It was shown that conductive, cubic TaN_x films could be deposited for substrate temperatures in the range of 150 to 250 °C using a H₂ plasma in the plasma-assisted ALD process. Furthermore, it was shown the electrical resistivity and mass density of the TaN_x films could be controlled by the

H₂ plasma exposure time in the ALD cycle. Admixing a small fraction of N₂ to the H₂ plasma resulted in an increase in resistivity of the TaN_x film, while highly-resistive, amorphous Ta₃N₅ films were deposited when under N-rich plasma conditions [H₂-N₂ (1:1) or NH₃]. *In situ* spectroscopic ellipsometry was used to distinguish the different TaN_x phases during growth. Different parametrizations were implemented to follow the clear transition in dielectric function and corresponding phase composition from conductive TaN_{x,x≤1} to semiconductive Ta₃N₅ films. Monitoring the magnitude of the Drude absorption in the dielectric function during growth turned out to be an *in situ*, sensitive measure of the resistivity of the TaN_{x,x≤1} films. By optical emission spectroscopy, the plasma emission signal during the plasma step was examined. It was shown that the emission spectrum revealed information on the ALD reaction itself due to plasma excitation of the (fragmented) surface reaction products in the plasma. This emission signal was particularly useful to determine the saturation of both ALD half reactions by means of monitoring the time-decay and the intensity of a carefully selected emission line.

In summary, an excellent control of the TaN_x material properties by the plasma-assisted ALD process was possible. For application of this process in 3D structures with high aspect-ratios, it remains an open question to what extent the conductive properties of a TaN_x film deposited on the sidewall of a 3D structure will vary with the depth in the structure. Because the impinging H radical flux at the top is substantially higher than at the bottom of the structure, this might cause a change in the material properties throughout the 3D structure. These and other issues with respect to the application of the TaN_x films will be addressed in future work.

Acknowledgments

Dr. M. Creatore is acknowledged for performing the XPS measurements at the Chemistry Department of Eindhoven University of Technology. The RBS analysis was carried out by Dr. Y. Tamminga, Dr. P. C. Zalm, and T. Dao, and the XRD measurements by F. Bakker and Dr. H. Wondergem (all Philips Research Eindhoven). M. J. F. van de Sande, J. F. C. Jansen, J. J. A. Zeebregts, A. B. M. Hüsken, and H. M. M. de Jong are thanked for their skillful technical assistance. This work was supported by the Dutch Technology Foundation STW and part of the work took place within the “INNOVia” project financed by SenterNovem, an agency of

the Netherlands Ministry of Economic Affairs. The research of one of the authors (W.M.M.K.) has been made possible by a fellowship from the Royal Netherlands Academy of Arts and Sciences (KNAW).

Bibliography

- [1] M. S. Akbar, S. Gopalan, H.-J. Cho, K. Onishi, R. Choi, R. Nieh, C. S. Kang, Y. H. Kim, J. Han, S. Krishnan, and J. C. Lee, *Appl. Phys. Lett.* **82**, 1757 (2003).
- [2] S.-J. Ding, Y.-J. Huang, Y. Li, D. W. Zhang, C. Zhu, and M.-F. Li, *J. Vac. Sci. Technol. B* **24**, 2518 (2006).
- [3] K. Holloway, P. M. Fryer, C. Cabral, Jr., J. M. E. Harper, P. J. Bailey, and K. H. Kelleher, *J. Appl. Phys.* **71**, 5433 (1992).
- [4] H. Kim, C. Detavenier, O. van der Straten, S. M. Rossnagel, A. J. Kellock, and D.-G. Park, *J. Appl. Phys.* **98**, 014308 (2005).
- [5] S. M. Rossnagel and H. Kim, *J. Vac. Sci. Technol. B* **21**, 2550 (2003).
- [6] D. Edelstein, C. Uzoh, C. Cabral, Jr., P. DeHaven, P. Buchwalter, A. Simon, E. Cooney, S. Malhotra, D. Klaus, H. Rathore, B. Agarwala, and D. Nguyen, in *Proceedings of the IEEE 2001 International Interconnect Technology Conference*, 9 (2001).
- [7] O. van der Straten, Y. Zhu, K. Dunn, E. T. Eisenbraun, and A. E. Kaloyeros, *J. Mater. Res.* **19**, 447 (2004).
- [8] S. M. Rossnagel and H. Kim, in *Proceedings of the IEEE 2001 International Interconnect Technology Conference*, 3 (2001).
- [9] J.-S. Park, H.-S. Park, and S.-W. Kang, *J. Electrochem. Soc.* **149**, C28 (2002).
- [10] M. Ritala, P. Kalsi, D. Riihelä, K. Kukli, M. Leskelä, and J. Jokinen, *Chem. Mater.* **11**, 1712 (1999).
- [11] T. Suntola, *Mater. Sci. Rep.* **4**, 261 (1989).
- [12] M. Ritala and M. Leskelä, *Handbook of Thin Film Materials*, volume 1, Academic, San Diego, CA (2001).
- [13] H. Kim, *J. Vac. Sci. Technol. B* **21**, 2231 (2003).
- [14] C. Stampfl and A. J. Freeman, *Phys. Rev. B* **71**, 024111 (2005).
- [15] J.-S. Park, M. J. Lee, C. S. Lee, and S.-W. Kang, *Electrochem. Solid-State Lett.* **4**, C17 (2001).

- [16] J. W. Hong, K. I. Choi, Y. K. Lee, S. G. Park, S. W. Lee, J. M. Lee, S. B. Kang, G. H. Choi, S. T. Kim, U.-I. Chung, and J. T. Moon, in *Proceedings of the IEEE 2004 International Interconnect Technology Conference*, 9 (2004).
- [17] J. Liu, J. Bao, M. Scharnberg, W. C. Kim, P. S. Ho, and R. Laxman, *J. Vac. Sci. Technol. A* **23**, 1107 (2005).
- [18] H.-S. Chung, J.-D. Kwon, and S. W. Kang, *J. Electrochem. Soc.* **153**, C751 (2006).
- [19] Y. Travaly, J. Schuhmacher, A. M. Hoyas, M. V. Hove, K. Maex, T. Abell, V. Sutcliffe, and A. M. Jonas, *J. Appl. Phys.* **97**, 84316 (2005).
- [20] R. Sreenivasan, T. Sugawara, K. C. Saraswat, and P. C. McIntyre, *Appl. Phys. Lett.* **90**, 102101 (2007).
- [21] E. Langereis, S. B. S. Heil, M. C. M. van de Sanden, and W. M. M. Kessels, *J. Appl. Phys.* **100**, 023534 (2006).
- [22] S. M. Aouadi and M. Debessai, *J. Vac. Sci. Technol. A* **22**, 1975 (2004).
- [23] J. Mistrik, K. Takahashi, R. Antos, M. Aoyama, T. Yamaguchi, Y. Anma, Y. Fukuda, M. B. Takeyama, A. Noya, Z.-T. Jiang, S. M. Thurgate, and G. V. Riessen, *Thin Solid Films* **455-456**, 473 (2004).
- [24] S. B. S. Heil, P. Kudlacek, E. Langereis, R. Engeln, M. C. M. van de Sanden, and W. M. M. Kessels, *Appl. Phys. Lett.* **89**, 131505 (2006).
- [25] S. B. S. Heil, E. Langereis, F. Roozeboom, M. C. M. van de Sanden, and W. M. M. Kessels, *J. Electrochem. Soc.* **153**, G956 (2006).
- [26] L. Doolittle, *Nucl. Instr. and Meth. in Phys. Res. B* **9**, 344 (1985).
- [27] J. A. Woollam Co., Inc., 650 J Street, Suite 39, Lincoln, NE 68508, USA (<http://www.jawoollam.com>).
- [28] P. Patsalas and S. Logothetidis, *J. Appl. Phys.* **93**, 989 (2003).
- [29] G. E. Jellison, Jr. and F. A. Modine, *Appl. Phys. Lett.* **69**, 371 (1996).

- [30] G. E. Jellison, Jr., V. I. Merkulov, A. A. Poretzky, D. B. Geohegan, G. Eres, D. H. Lowndes, and J. B. Caughman, *Thin Solid Films* **377-378**, 68 (2000).
- [31] B. von Blanckenhagen, D. Tonova, and J. Ullmann, *Appl. Opt.* **41**, 3137 (2002).
- [32] H. Chen and W. Z. Shen, *Eur. Phys. J. B* **43**, 503 (2005).
- [33] N. V. Nguyen, C. A. Richter, Y. J. Cho, G. B. Alers, and L. A. Stirling, *Appl. Phys. Lett.* **77**, 3012 (2000).
- [34] K. Baba and R. Hatada, *Surf. Coat. Technol.* **84**, 429 (1996).
- [35] R. L. Puurunen, *J. Appl. Phys.* **97**, 121301 (2005).
- [36] W. J. Maeng, S.-J. Park, and H. Kim, *J. Vac. Sci. Technol. B* **24**, 2276 (2006).
- [37] International Centre for Diffraction Data Powder Diffraction File No. 2 (PDF-2), 2006 (<http://www.icdd.com>).
- [38] A. Furuya, H. Tsuda, and S. Ogawa, *J. Vac. Sci. Technol. B* **23**, 979 (2005).
- [39] C. S. Kang, H. Cho, Y. H. Kim, R. Choi, K. Onishi, A. Shahriar, and J. C. Lee, *J. Vac. Sci. Technol. B* **21**, 2026 (2003).
- [40] H. Kim, A. J. Kellock, and S. M. Rossnagel, *J. Appl. Phys.* **92**, 7080 (2002).
- [41] F. A. Modine, R. W. Major, T. W. Haywood, G. R. Gruzalski, and D. Y. Smith, *Phys. Rev. B* **29**, 836 (1984).
- [42] S. J. Henderson and A. L. Hector, *J. Solid-State Chem.* **179**, 3518 (2006).
- [43] Y. Y. Wu, A. Kohn, and M. Eizenberg, *J. Appl. Phys.* **95**, 6167 (2004).
- [44] H. J. Coyne and R. N. Tauber, *J. Appl. Phys.* **39**, 5585 (1968).
- [45] R. W. B. Pearse and A. G. Gaydon, *The identification of molecular spectra*, Chapman and Hall, London (1976).

Chapter 3

Plasma-assisted atomic layer deposition of Al_2O_3 moisture permeation barriers on polymers*

Abstract

Thin Al_2O_3 films of different thicknesses (10–40 nm) were deposited by plasma-assisted atomic layer deposition on substrates of poly(2,6-ethylene naphthalate) (PEN) and the water vapor transmission rate (WVTR) values were measured by means of the calcium test. The permeation barrier properties improved with decreasing substrate temperature and a good WVTR of $5 \times 10^{-3} \text{ g m}^{-2} \text{ day}^{-1}$ ($\text{WVTR}_{\text{PEN}} = 0.5 \text{ g m}^{-2} \text{ day}^{-1}$) was measured for a 20 nm thick Al_2O_3 film deposited at room temperature using short purging times. Such ultrathin, low-temperature deposited, high-quality moisture permeation barriers are an essential requirement for the implementation of polymeric substrates in flexible electronics and displays applications.

*Published as: E. Langereis, M. Creatore, S. B. S Heil, M. C. M. van de Sanden, and W. M. M. Kessels, *Appl. Phys. Lett.* **89**, 081915 (2006).

Successful application of flexible organic light emitting diodes (F-OLEDs) requires excellent moisture permeation barriers to minimize the degradation of the OLED device [1, 2]. Transparent moisture permeation barriers with an estimated water vapor transmission rate (WVTR) as low as $10^{-6} \text{ g m}^{-2} \text{ day}^{-1}$ need to be deposited [1, 3]. Low deposition temperatures are required below the glass transition temperature of polymers and there is a strong preference for room temperature (RT) deposition because of process simplicity and compatibility with the OLED manufacturing process [4, 5]. Because the moisture permeation properties of a single layer barrier are eventually limited by the defect density of the layer [6], the deposition of multilayer structures is expected to be the path towards the WVTR requirements mentioned above [7–9]. The multilayer structures will become most effective when the individual layers themselves have excellent permeation properties.

The atomic layer deposition (ALD) technique is known to produce densely-packed, virtually defect-free, highly uniform and conformal films and can therefore be used to deposit high-quality single layer permeation barriers [4, 10, 11]. Groner *et al.* reported good permeation barrier properties ($\text{WVTR} = 1 \times 10^{-3} \text{ g m}^{-2} \text{ day}^{-1}$) of very thin (10–25 nm) Al₂O₃ films deposited from sequential trimethylaluminum (TMA) and water vapor exposures. However, they limited their deposition to a temperature of 120 °C to have a short ALD cycle time (60 seconds at 120 °C) [11]. They also showed ALD of Al₂O₃ films at 33 °C, but this required 180s of purging time to remove the residual water vapor, resulting in a total cycle time of 203s [12].

The plasma-assisted ALD technique has the same growth characteristics as thermal ALD, but the use of O₂ plasma radicals in the process enables deposition at room temperature without requiring long purging times. Furthermore, when admixing N₂ gas to the O₂ plasma, also N-doped Al₂O₃ can easily be deposited by plasma-assisted ALD, which has been investigated previously for its permeation barrier properties [13].

In this letter, we show the ability of plasma-assisted ALD in obtaining good Al₂O₃ moisture permeation barriers films at low substrate temperature (RT–100 °C) on poly(2,6-ethylene naphthalate) (PEN) substrates using short cycle times. A good WVTR of $5 \times 10^{-3} \text{ g m}^{-2} \text{ day}^{-1}$ is obtained for a 20 nm thick film deposited at room temperature with a cycle time of 17s.

Thin Al₂O₃ films were deposited in a home-built deposition reactor by plasma-assisted ALD from sequentially exposing the substrate to TMA

Table 3.1: Properties of ~ 30 nm thick Al_2O_3 films deposited at different temperatures on native oxide covered *c*-Si substrates using two different TMA dosing conditions in the plasma-assisted ALD cycle. The growth rate is determined from *in situ* SE, the mass density and film composition are determined from RBS. The first row gives the typical absolute errors on the results.

TMA dosing	Deposition temperature (°C)	Growth rate (nm/cycle)	Mass density (g cm ⁻³)	Composition Al ₂ O _x
Undersaturated	25	0.12±0.005	3.0±0.1	3.60±0.05
	50	0.11	2.9	3.40
	100	0.11	2.8	3.40
	200	0.097	2.9	3.34
Saturated	70	0.17	2.9	3.20
	200	0.13	3.0	3.14

vapor and a remote O₂ plasma. The deposition chamber was continuously purged by O₂ resulting in a pressure of 7.5 mTorr. The plasma-assisted ALD cycle, used at all deposition temperatures consisted of multiple TMA dosing (1 s each) injected from a trapped volume, 5 s purge, 2 s O₂ plasma, and 5 s purge. The plasma was created in a remote inductively coupled plasma (ICP) source operated on the O₂ background gas. The depositions were carried from RT up to 200 °C on *c*-Si substrates and up to 100 °C on PEN (DuPont Teijin Films, glass transition temperature $T_g = 121$ °C). Prior to deposition, the PEN substrates were ultrasonically cleaned in ethanol and were heated overnight at 70 °C in the reaction chamber at a base pressure of 10⁻⁶ Torr to remove residual water in the polymer. The moisture permeation barrier properties of the films were determined by means of the calcium test [14], in which the change in transparency of a 100 nm thick Ca film was monitored in a controlled environment ($T = 21$ °C and 60% relative humidity) to determine the WVTR of the film.

The plasma-assisted ALD Al_2O_3 films were characterized on *c*-Si wafers and the results are reported in Table 3.1. Two different TMA doses were used, i.e., undersaturated dosing (1 TMA dose) and saturated dosing (5 TMA doses), providing information about the influence of the chemical composition of the Al_2O_3 film on the barrier properties. During deposition, the Al_2O_3 thickness was determined by *in situ* spectroscopic ellipsom-

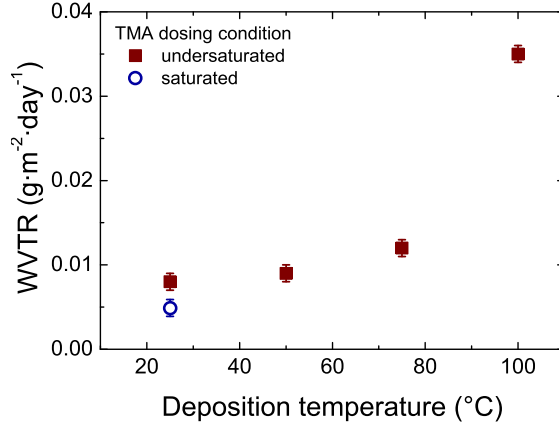


Figure 3.1: Water vapor transmission rate (WVTR) of 20 nm thick plasma-assisted ALD Al_2O_3 films on PEN as a function of deposition temperature with undersaturated and saturated TMA dosing conditions.

etry (SE). As expected, the growth rate of the saturated plasma-assisted ALD growth is higher compared to undersaturated TMA dosing conditions. The growth rate increased for decreasing substrate temperatures, as reported previously for ALD of Al_2O_3 [15, 16]. Rutherford backscattering spectroscopy (RBS) showed that the mass density of the Al_2O_3 films was virtually independent of deposition temperature, yielding an average value of $2.9 \pm 0.2 \text{ g cm}^{-3}$. All the deposited Al_2O_3 films were oxygen-rich and the amount of oxygen in the film increased for decreasing deposition temperature, however the saturated growth condition resulted in a limited excess of oxygen in the film. Elastic recoil detection showed that the films deposited by undersaturated and saturated TMA dosing contained 4 and 2 at. % H for the deposition at 200 °C, respectively. The hydrogen content increased at lower temperature up to 12 at. % for undersaturated deposition at RT and indicates the presence of additional hydroxyl groups in the films.

RBS and x-ray photoelectron spectroscopy on a relatively thick Al_2O_3 film (500 cycles) deposited by undersaturated TMA dosing at 100 °C, showed the same chemical composition on *c*-Si and PEN substrates, i.e., the [O]/[Al] ratio was 1.7. These results indicate that the bulk material properties of the film deposited by plasma-assisted ALD are not affected by the substrate material used.

Figure 3.1 shows the WVTR of 20 nm thin Al_2O_3 film as a function of deposition temperature in the range RT–100 °C. The WVTR is found

to improve for films deposited at lower temperatures and the saturated growth condition yields slightly better results. The trend with temperature is different than reported for thermal ALD Al_2O_3 films prepared by TMA and H_2O by Park *et al.* who observed that the barrier properties deteriorated for lower deposition temperatures (80°C) [4]. The reason for the improvement of the WVTR for plasma-assisted ALD barriers is yet unknown but it can possibly be related to the observed increase in hydroxyl content in the Al_2O_3 films deposited at low temperatures (cf. Table 3.1). It has been reported that the high polarizability of the (Al–)OH bonds of the film could obstruct water vapor permeation through the layer by means of H-bonding with water vapor [17], although H_2O dissociation at reactive hydrophilic sites is also suggested to occur [13]. The mismatch of the coefficient of thermal expansion of Al_2O_3 and PEN might be another explanation as it can lead to stress generation at the interface when the sample is brought to RT after deposition at elevated temperature and, therefore, induce deterioration of the barrier properties. This effect, for which no morphological evidence is available yet, could be related to the difference in initial growth on the polymer surface between plasma-assisted and thermal ALD. Thermal ALD films are hypothesized to nucleate inside the polymer matrix, whereas a more discrete interface could be present for plasma-assisted ALD as the O_2 plasma can create additional functional groups (e.g., OH) on the polymer surface during the early stages of growth.

By adding N_2 gas into the O_2 plasma ($[\text{N}_2]/[\text{O}_2] = 3:2$), N-doped (~ 1 at. % N) stoichiometric Al_2O_3 was deposited and the nitrogen content in the film could be controlled by changing the plasma composition. The moisture permeation properties were briefly investigated for a deposition carried out at room temperature, resulting in a WVTR of $0.009 \text{ g m}^{-2} \text{ day}^{-1}$ for a 20 nm thick film and did not show improved permeation barrier properties compared to the Al_2O_3 films [13]. Preliminary investigation on AlN films deposited by plasma-assisted ALD at room temperature using a $\text{N}_2\text{--H}_2$ (3:2) plasma in the cycle showed negligible barrier properties.

The WVTR of the Al_2O_3 films as a function of thickness for deposition at RT is shown in Fig. 3.2. It is observed that a 10 nm thick Al_2O_3 film already shows very good barrier properties. The WVTR saturates for films thicker than 20 nm to the value of $5 \times 10^{-3} \text{ g m}^{-2} \text{ day}^{-1}$, which is good for a single layer barrier, especially in comparison to the $0.40 \text{ g m}^{-2} \text{ day}^{-1}$ for a magnetron sputtered 34 nm thick AlO_x film [18] and

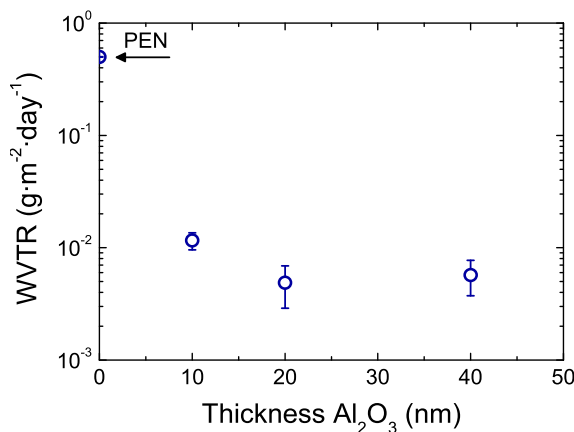


Figure 3.2: Water vapor transmission rate (WVTR) of plasma-assisted ALD Al_2O_3 films on PEN as a function of film thickness. The films are deposited at room temperature with saturated TMA dosing conditions.

to the $0.045 \text{ g m}^{-2} \text{ day}^{-1}$ reported for plasma-enhanced chemical vapor deposited (PE-CVD) SiN_x films with a thickness of 130 nm [19]. Similarly, for the thermal ALD process using TMA and H_2O , Park *et al.* reported a WVTR of $0.062 \text{ g m}^{-2} \text{ day}^{-1}$ for a polyethersulfone (PES) film coated on both sides with 30 nm Al_2O_3 film deposited 90°C [4]. On the other hand, the obtained WVTR values for deposition at RT were in the same order as the results reported by Groner *et al.* by ALD at 120°C [11]. The improvement of barrier properties with respect to films deposited by PE-CVD can be related to the uniform and conformal ALD growth of the barrier layer on the polymer surface, which is porous, defective, and not particle-free. A saturation of the barrier properties with film thickness is, however, still observed. Plausible explanations are that the Al_2O_3 films are not completely pinhole-free or that “defects” on the polymer surface are not conformally “sealed” by the ALD film.

In summary, we have shown the feasibility of plasma-assisted ALD Al_2O_3 films at room temperature using short purging times in the order of seconds. The barrier properties of the Al_2O_3 films improved for lower deposition temperatures, which is promising from a manufacturing perspective of polymer substrates and for encapsulation of F-OLEDs at room temperature preventing device degradation [20]. Saturation in barrier properties was observed for increasing film thickness, which suggests that the mechanism of water vapor permeation through the barrier/polymer is still defect-controlled. The room temperature plasma-assisted ALD of 20 nm

thick Al₂O₃ on PEN resulted in a good moisture permeation barrier resulting in a WVTR of $5 \times 10^{-3} \text{ g m}^{-2} \text{ day}^{-1}$. In future experiments, the water and oxygen permeation mechanism will be further investigated focusing on the role of defects, nanoscale morphology and the influence of the polymer substrate.

Note added in proof: After submission of this paper, Carcia *et al.* reported an excellent WVTR $< 10^{-5} \text{ g m}^{-2} \text{ day}^{-1}$ for a 25 nm thick Al₂O₃ film deposited by thermal ALD on PEN [21]. This experiment shows the potential of single layer barriers that can be obtained by ALD. Appropriate substrate cleaning and handling minimizing the amount of particles on the polymer surface is believed to be one of the key aspects in obtaining these superior barrier properties, as already observed in the case of plasma-deposited (and sputtered) layers. For the experiments reported in the present work, no special care of substrate cleaning and handling was taken other than described in the text.

The authors would like to thank J. L. van Hemmen and TNO Science & Technology for the calcium test measurements, Y. Tamminga and T. Dao from Philips Research Eindhoven for the RBS analysis. The Dutch Technology Foundation STW is acknowledged for their financial support. The research of one of the authors (W.M.M.K.) has been made possible by a fellowship of the Royal Netherlands Academy of Arts and Sciences (KNAW).

Bibliography

- [1] J. S. Lewis and M. S. Weaver, *IEEE J. Sel. Top. Quantum Electron.* **10**, 45 (2004).
- [2] J. N. Bardsley, *IEEE J. Sel. Top. Quantum Electron.* **10**, 3 (2004).
- [3] F. J. van Assche, R. T. Vangheluwe, J. W. C. Maes, W. S. Mischke, M. D. Bijker, F. C. Dings, M. F. J. Evers, W. M. M. Kessels, and M. C. M. van de Sanden, *SID Int. Symp. Digest Tech. Papers* **35**, 695 (2004).
- [4] S.-H. K. Park, J. Oh, C.-S. Hwang, J.-I. Lee, Y. S. Yang, and H. Y. Chu, *Electrochem. Solid-State Lett.* **8**, H21 (2005).
- [5] S. J. Yun, Y.-W. Ko, and J. W. Lim, *Appl. Phys. Lett.* **85**, 4896 (2005).
- [6] A. S. da Silva Sobrinho, G. Czeremuszkin, M. Latrèche, and M. R. Wertheimer, *J. Vac. Sci. Technol. A* **18**, 149 (2000).
- [7] G. L. Graff, R. E. Williford, and P. E. Burrows, *J. Appl. Phys.* **96**, 1840 (2004).
- [8] P. E. Burrows, G. L. Graff, M. E. Gross, P. M. Martin, M. K. Shi, M. Hall, E. Mast, C. Bonham, W. Bennett, and M. B. Sullivan, *Displays* **22**, 65 (2001).
- [9] M. S. Weaver, L. A. Michalski, K. Rajan, M. A. Rothman, J. A. Silvernail, P. E. Burrows, G. L. Graff, M. E. Gross, P. M. Martin, M. Hall, E. Mast, C. Bonham, W. Bennett, and M. Zumhoff, *Appl. Phys. Lett.* **81**, 2929 (2002).
- [10] A. P. Ghosh, L. J. Gerenser, C. M. Jarman, and J. E. Fornalik, *Appl. Phys. Lett.* **86**, 223503 (2005).
- [11] M. D. Groner, S. M. George, R. S. McLean, and F. Carcia, *Appl. Phys. Lett.* **88**, 051907 (2006).
- [12] M. D. Groner, F. H. Fabreguette, J. W. Elam, and S. M. George, *Chem. Mater.* **16**, 639 (2004).
- [13] A. G. Erlat, B. M. Henry, C. R. M. Grovenor, A. G. D. Briggs, R. J. Carter, and Y. Tsukahara, *J. Phys. Chem. B* **108**, 883 (2004).

-
- [14] P. C. P. Bouten, G. Nisato, P. J. Slikkerveer, H. F. van Tongeren, H. E. Itzhak, and P. van der Sluis, US Patent No. 6,993,956 (7 February 2002).
- [15] A. W. Ott, J. W. Klaus, J. M. Johnson, and S. M. George, *Thin Solid Films* **292**, 135 (1997).
- [16] A. Niskanen, K. Arstila, M. Ritala, and M. Leskelä, *J. Electrochem. Soc.* **152**, F90 (2005).
- [17] W. H. Koo, S. M. Jeong, S. H. Choi, W. J. Kim, H. K. Baik, S. M. Lee, and S. J. Lee, *J. Phys. Chem. B* **109**, 11354 (2005).
- [18] B. M. Henry, F. Dinelli, K.-Y. Zhao, C. R. M. Grovenor, O. V. Kolosov, G. A. D. Briggs, A. P. Roberts, R. S. Kumar, and R. P. Howson, *Thin Solid Films* **355-356**, 500 (1999).
- [19] M. Creatore, V. I. T. A. Lohmann, C. G. Klaasse Bos, A. C. M. Hamelink, M. M. Koetse, H. F. M. Schoo, and M. C. M. van de Sanden, in *Proceedings of the 48th Annual SVC Technical Conference and Smart Materials Symposium, Co, 23 - 28 April 2005*, 163, Society of Vacuum Coaters, Albuquerque, NM (2005).
- [20] K. Tsukagoshi, J. Tanabe, I. Yagi, K. Shigeto, K. Yanagisawa, and Y. Aoyagi, *J. Appl. Phys.* **99**, 064506 (2006).
- [21] P. F. Carcia, R. S. McLean, M. H. Reilly, M. D. Groner, and S. M. George, *Appl. Phys. Lett.* **89**, 031915 (2006).

Chapter 4

Surface chemistry of plasma-assisted atomic layer deposition of Al_2O_3 studied by infrared spectroscopy*

Abstract

The surface groups created during plasma-assisted atomic layer deposition (ALD) of Al_2O_3 were studied by infrared spectroscopy. For temperatures in the range of 25–150 °C, $-\text{CH}_3$ and $-\text{OH}$ were unveiled as dominant surface groups after the $\text{Al}(\text{CH}_3)_3$ precursor and O_2 plasma half-cycles, respectively. At lower temperatures more $-\text{OH}$ and C-related impurities were found to be incorporated in the Al_2O_3 film, but the impurity level could be reduced by prolonging the plasma exposure. The results demonstrate that $-\text{OH}$ surface groups rule the surface chemistry of the Al_2O_3 process and likely that of plasma-assisted ALD of metal oxides from organometallic precursors in general.

*Published as: E. Langereis, J. Keijmel, M. C. M. van de Sanden, and W. M. M. Kessels, *Appl. Phys. Lett.* **92**, 231904 (2008).

Atomic layer deposition (ALD) is the method of choice for the deposition of ultrathin and conformal high-*k* metal oxide films as required in next-generation memory and transistor devices. To extend the applications of ALD, processes using alternative oxidant sources, such as O₃ and O₂ plasma, are actively researched. Using these oxidant sources, additional reactivity is supplied to the surface chemistry and this potentially allows for deposition at lower temperatures (<150 °C) without compromising film quality [1–3].

In order to fully exploit the benefits of the ALD technique, a fundamental understanding of the underlying surface chemistry is of vital importance. To this end the ALD process of Al₂O₃ has been studied in great detail, since it shares generic features to equivalent metal oxide ALD processes. The conventional, thermal ALD process of Al₂O₃ using Al(CH₃)₃ precursor and H₂O was found to be ruled by the formation of –CH₃ and –OH surface groups after the precursor and oxidant half-cycles, respectively, with the formation of volatile CH₄ in both half-reactions [4–6]. In the O₃-based ALD process, the formation of –CH₃ surface groups and volatile CH₄ after Al(CH₃)₃ adsorption were found to be similar to the H₂O-based process. During the O₃ half-cycle, however, the formation of CH₄ and C₂H₄ have been reported [1, 2] and it is still debated whether –OH or formate [–O(–O)CH] groups are the dominant surface species produced by the O₃ reactions [2, 7]. In our previous work on plasma-assisted ALD of Al₂O₃, we observed the formation of CH₄ after Al(CH₃)₃ adsorption, while mainly CO, CO₂, and H₂O were formed in the O₂ plasma half-cycle through combustionlike surface reactions [3, 8]. The surface chemistry during this plasma-assisted ALD process could not be fully resolved yet, because no measurements on the surface groups were available.

Despite the different oxidant sources employed, it is intriguing to note that the dependence of growth per cycle on the deposition temperature is quite similar for the different oxidant sources for ALD of Al₂O₃, as shown in Fig. 4.1 for H₂O [2, 9–13], O₃ [2, 13], and O₂ plasma [9]. For temperatures >100 °C, the growth per cycle of Al₂O₃ monotonically decreases with increasing deposition temperature for all three oxidant sources and the differences are relatively small. Only below 100 °C, the growth per cycle significantly differs which has been attributed to difficulties to achieve saturation when dosing H₂O [9, 10]. For the H₂O-based process, the decrease in growth per cycle with increasing temperature has been related to the thermal stability of the –OH surface groups which are involved in the Al(CH₃)₃ chemisorption reactions [5, 10]. The O₂ plasma-based process

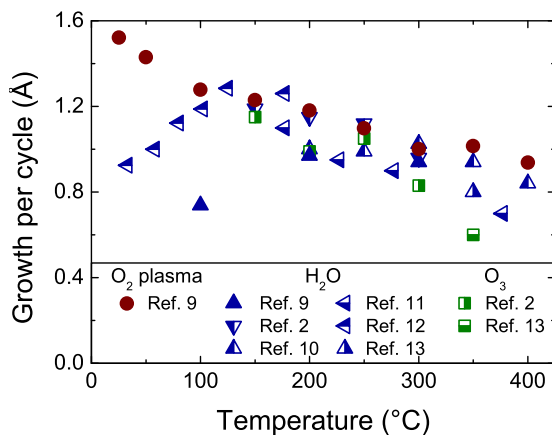


Figure 4.1: Literature data on the growth per cycle of Al_2O_3 as a function of deposition temperature for ALD processes using $\text{Al}(\text{CH}_3)_3$ as precursor and H_2O , O_3 , or O_2 plasma as oxidant source. The data presented were corrected for differences in mass density and represent the growth per cycle of a film with a mass density of 3.0 g cm^{-3} as typically reported for ALD Al_2O_3 films.

shows a similar decrease but for the complete temperature range (25–400 °C). This resemblance might indicate some similarities between the surface groups involved in plasma-assisted and thermal ALD of Al_2O_3 . To better understand the dependence of the growth per cycle on the deposition temperature, however, insight into the surface chemistry of plasma-assisted ALD of Al_2O_3 is necessary.

The primary objective of this letter is to elucidate the surface chemistry of plasma-assisted ALD of Al_2O_3 through detection of the surface groups generated in the half-cycles by means of transmission infrared spectroscopy measurements. The main result of this study is the observation that $-\text{CH}_3$ and $-\text{OH}$ surface groups are predominantly formed after the $\text{Al}(\text{CH}_3)_3$ and O_2 plasma half-cycles, respectively. This observation implies that $-\text{OH}$ surface groups rule the surface chemistry during plasma-assisted ALD of Al_2O_3 similar to the H_2O -based process. Also the influence of the deposition temperature (25–150 °C), the incorporation of impurities, and a direct comparison with the thermal ALD process at 150 °C are addressed. The results will facilitate the design of improved low temperature (<150 °C) ALD processes and it is expected that they have generic implications for plasma-assisted ALD processes of other metal oxide films.

Plasma-assisted and thermal ALD processes of Al_2O_3 were studied in a wall-heated reactor equipped with an O_2 -operated inductively coupled

plasma source and bubblers with Al(CH₃)₃ (99.9999%, Akzo Nobel) and H₂O (Ultrapur[®], >99.9999%, Merck). The cycles consisted typically of 25 ms of Al(CH₃)₃ dosing followed by 2 s O₂ plasma exposure or 2×240 ms H₂O dosing in the plasma-assisted and thermal ALD process, respectively. The Al₂O₃ films were deposited onto KBr flats that also served as infrared viewports in the reactor. It was verified that the growth per cycle and Al₂O₃ film quality were similar to results obtained on substrates positioned on the substrate holder [9, 14]. In between the ALD half-reactions, transmission infrared spectra (2×256 scans) were collected by an infrared interferometer (Bruker, Tensor 27) with an external liquid-N₂ cooled HgCdTe detector (Bruker, D313). The absorbance spectra were averaged over 40 ALD cycles to reduce the noise level to $\sim 5 \times 10^{-6}$.

The surface species created during the plasma-assisted ALD half-cycles of Al₂O₃ were studied at a deposition temperature of 150 °C and were directly compared to the results of the thermal ALD process carried out at the same temperature. From qualitative comparison of the differential vibrational spectra shown in Fig. 4.2(a), it is clear that the same types of surface species are created in both ALD processes. After the Al(CH₃)₃ precursor adsorption, –CH₃ surface groups appear as observed in stretching (asymmetric ~ 2937 cm⁻¹, symmetric ~ 2896 cm⁻¹, and bending overtone ~ 2831 cm⁻¹), deformation (~ 1208 cm⁻¹), and rocking (~ 750 cm⁻¹) modes, while –OH surface groups disappear as observed in the broad stretching (3750–2770 cm⁻¹) mode [4, 5, 15]. This broad –OH stretching feature originates from various types of –OH groups on the Al₂O₃ surface, ranging from unassociated –OH (3800–3700 cm⁻¹) to associated –OH (3700–2700 cm⁻¹) modes [5, 16–18]. For both ALD processes, the differential spectra clearly show that –OH surface groups are created after the reaction of the O₂ plasma and the H₂O oxidant with the –CH₃ surface groups.

For the O₂ plasma-based process, the influence of deposition temperature on the surface groups was studied for films deposited at 25, 100, and 150 °C, as shown in Fig. 4.2(b). From the similarities in the differential vibrational spectra, it is concluded that the surface chemistry at lower temperatures also proceeds predominantly via the formation of –CH₃ and –OH surface species. At lower temperatures, the amount of –OH surface groups created by the O₂ plasma strongly increased and a broadening of the –OH stretching modes was observed. The broadening at lower deposition temperatures can be attributed to the dipole interaction (in particular, hydrogen-bonding) between the densely-packed –OH surface groups.

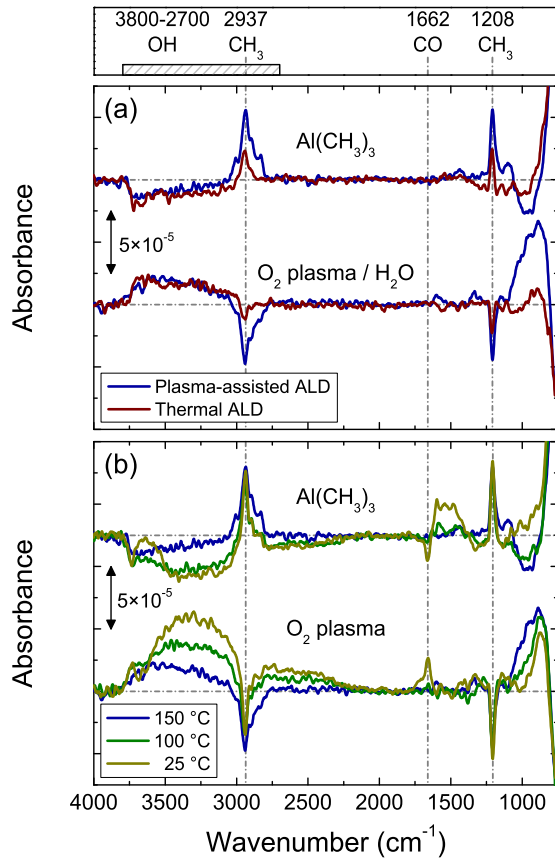


Figure 4.2: Differential infrared spectra after the $\text{Al}(\text{CH}_3)_3$ precursor and oxidation half-cycles showing appearance and disappearance (with respect to the baseline) of surface groups in the two ALD half-reactions. (a) Comparison between the surface groups involved in plasma-assisted and thermal ALD of Al_2O_3 at a deposition temperature of 150 °C. (b) Surface groups involved in plasma-assisted ALD at deposition temperatures of 25, 100, and 150 °C. The peak positions of the $-\text{CH}_3$ groups, $-\text{OH}$ groups, and $\text{C}=\text{O}$ impurities are indicated.

Moreover, the presence of physisorbed H₂O on the Al₂O₃ surface can also be of influence [19, 20]. In addition, an unassigned broad feature around $\sim 900\text{ cm}^{-1}$ is observed for the films deposited by plasma-assisted ALD. The feature is most likely not related to the broad Al–O phonon mode ($\sim 954\text{ cm}^{-1}$ in Ref. [15]), since its magnitude increased with increasing temperature opposite to the trend observed for the growth per cycle of the Al₂O₃ films (Fig. 4.1).

Insight into the type and relative amount of impurities incorporated into the Al₂O₃ films can be deduced from a differential spectrum obtained after a full ALD cycle (i.e., basically adding the differential spectra for the two half-cycles). From such differential spectra, it is concluded that –OH groups were incorporated in the Al₂O₃ bulk with the amount of –OH incorporated increasing when going to lower deposition temperatures. This observation is in line with previous reports [5, 9, 14], as well as with the compositional data of Al₂O₃ films deposited in the temperature range studied, i.e., $x = [\text{O}]/[\text{Al}] = 1.6$ with $\sim 4\text{ at. \% H}$ at $150\text{ }^\circ\text{C}$, $x = 1.7$ with $\sim 7\text{ at. \% H}$ at $100\text{ }^\circ\text{C}$, and $x = 2.1$ with $\sim 15\text{ at. \% H}$ at $25\text{ }^\circ\text{C}$ (all using 2 s O₂ plasma exposure) [9]. From the spectra, no evidence is found for the incorporation of –CH_{*x*} groups into the bulk Al₂O₃ film at the studied temperatures. Interestingly for the film deposited at $25\text{ }^\circ\text{C}$, carbon-related impurities appeared ($\sim 1662\text{ cm}^{-1}$) after the O₂ plasma step, which changed into a broad feature ($1600\text{--}1450\text{ cm}^{-1}$) after the Al(CH₃)₃ dosing. The peaks observed can be attributed to impurities containing C=O or COO bonds indicating incomplete removal of the carbon from the surface during the 2 s O₂ plasma step at $25\text{ }^\circ\text{C}$. Incorporation of these surface features into the Al₂O₃ bulk after Al(CH₃)₃ precursor adsorption is expected to account for the shift and broadening of the peak. The appearance of these C=O/COO bonds is most likely characteristic for the strong oxidation power of the O₂ plasma and these bonds can be interpreted as intermediate reaction states in the combustionlike reaction from the –CH₃ covered surface to the –OH covered surface after the O₂ plasma exposure. This hypothesis is corroborated by the fact that the magnitude of the C-related absorbance could be reduced by using a longer O₂ plasma step in the ALD cycle. Furthermore, in our previous work, compositional data on the Al₂O₃ films deposited at $25\text{ }^\circ\text{C}$ revealed that the amount of O, C, and H impurities was substantially reduced when using 4 s (instead of 2 s) of O₂ plasma exposure [9].

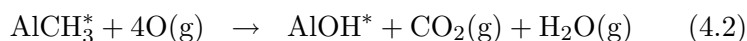
From the quantitative amount of surface groups observed, in principle, conclusions can be drawn regarding the ALD surface chemistry at the

different temperatures. For example, the increase in $-OH$ surface groups involved in plasma-assisted ALD when going to lower temperatures can be related to the increase in growth per cycle. However, care must be taken in such interpretation, since residual H_2O (either being remnants of the excessive H_2O dosing during thermal ALD or of the H_2O reaction by-products created during plasma-assisted ALD [3]) is difficult to completely purge out of the reactor, especially at the low temperatures employed. Residual H_2O can lead to $-CH_3$ consumption and $-OH$ formation during the purge time and (relatively long) infrared measurement time following the $Al(CH_3)_3$ precursor half-cycle. Evidence for this effect was found by comparing infrared measurements consecutively acquired during the purge time. Therefore, differences in the experiment with respect to conditions and timing can partly account for the different amount of $-CH_3$ groups observed in thermal and plasma-assisted ALD at $150^\circ C$ [Fig. 4.2(a)].

Notwithstanding this influence of residual H_2O and other effects related to the experiment, the increase in $-OH$ surface groups when going to lower temperature is remarkable compared to the virtually temperature independent amount of $-CH_3$ surface groups [Fig. 4.2(b)]. When linked to the increase in growth per cycle (Fig. 4.1), these observations support a more pronounced bifunctional adsorption of the precursor when going to lower temperatures, as was also reported for thermal ALD [21]. Upon bifunctional adsorption, the $Al(CH_3)_3$ molecule splits off two $-CH_3$ ligands consuming two $-OH$ surface groups and, thereby, releasing two CH_4 molecules. Consequently, after bifunctional adsorption only one $-CH_3$ surface group remains per adsorbed $Al(CH_3)_3$ compared to two $-CH_3$ surface groups remaining after monofunctional adsorption; a process that becomes more important at higher temperatures when the amount of $-OH$ surface groups becomes relatively low [21]. In this respect, the virtually constant amount of $-CH_3$ surface groups observed in the infrared spectra in Fig. 4.2(b) combined with the increase in growth per cycle confirms that a larger fraction of the $Al(CH_3)_3$ molecules bifunctionally adsorbs when going to lower temperatures.

In summary, the surface species created during the half-cycles of plasma-assisted ALD of Al_2O_3 were measured by transmission infrared spectroscopy. Combining the results with gas phase products previously reported [3], it was established that the surface chemistry of plasma-assisted ALD of Al_2O_3 is ruled by the formation of $-OH$ surface groups in the combustion-like reactions between $-CH_3$ surface groups and the O_2 plasma species. Therefore the following surface reactions are proposed for plasma-assisted

ALD of Al₂O₃:



where the asterisks designate the surface species and only the case of monofunctional adsorption is considered for simplicity. Moreover, the amount of –OH groups involved in the surface reactions increased for lower deposition temperatures which can be related to the higher growth per cycle at these temperatures. It was also demonstrated that the high reactivity delivered by the O₂ plasma allows for film deposition at temperatures down to room temperature, but under these conditions a longer plasma exposure time was required to complete the surface reactions and reduce the impurity content of the Al₂O₃ films. Tuning the plasma reactivity in the ALD process is thus key in obtaining high quality films at low deposition temperatures. Because combustionlike reactions of organic surface ligands by O₂ plasma species have been reported for more plasma-assisted ALD processes [22], it is expected that the surface chemistry discussed is generic for plasma-assisted ALD processes of high-*k* metal oxides using (similar) metal-organic precursors and O₂ plasma.

The authors thank Dr. A. C. R. Pipino for fruitful discussions. The Dutch Technology Foundation STW is acknowledged for their financial support.

Bibliography

- [1] G. Prechtl, A. Kersch, G. Schulze Icking-Konert, W. Jacobs, T. Hecht, H. Boubekeur, and U. Schröder, in *Proceedings of the IEEE 2003 International Electron Devices Meeting*, 9.6.1 (2003).
- [2] S. D. Elliot, G. Scarel, C. Wiemer, M. Fanciulli, and G. Pavia, *Chem. Mater.* **18**, 3764 (2006).
- [3] S. B. S. Heil, P. Kudlacek, E. Langereis, R. Engeln, M. C. M. van de Sanden, and W. M. M. Kessels, *Appl. Phys. Lett.* **89**, 131505 (2006).
- [4] C. Soto and W. T. Tysoe, *J. Vac. Sci. Technol. A* **9**, 2686 (1991).
- [5] A. C. Dillon, A. W. Ott, J. D. Way, and S. M. George, *Surf. Sci.* **322**, 230 (1995).
- [6] M. D. Halls, K. Raghavachari, M. M. Frank, and Y. J. Chabal, *Phys. Rev. B* **68**, 161302 (2003).
- [7] D. N. Goldstein and S. M. George, *Proceedings of 6th International Conference on Atomic Layer Deposition* (American Vacuum Society, New York, 2006); J. A. McCormick, A. W. Weimer, and S. M. George, *Proceedings of 7th International Conference on Atomic Layer Deposition* (American Vacuum Society, New York, 2007).
- [8] S. B. S. Heil, J. L. van Hemmen, M. C. M. van de Sanden, and W. M. M. Kessels, *J. Appl. Phys.* **103**, 103302 (2008).
- [9] J. L. van Hemmen, S. B. S. Heil, J. H. Klootwijk, F. Roozeboom, C. J. Hodson, M. C. M. van de Sanden, and W. M. M. Kessels, *J. Electrochem. Soc.* **154**, G165 (2007).
- [10] R. Matero, A. Rahtu, M. Ritala, M. Leskelä, and T. Sajavaara, *Thin Solid Films* **368**, 1 (2000).
- [11] A. W. Ott, J. W. Klaus, J. M. Johnson, and S. M. George, *Thin Solid Films* **292**, 135 (1997).
- [12] M. D. Groner, F. H. Fabreguette, J. W. Elam, and S. M. George, *Chem. Mater.* **16**, 639 (2004).
- [13] S.-C. Ha, E. Choi, S.-H. Kim, and J. S. Roh, *Thin Solid Films* **476**, 252 (2005).

- [14] E. Langereis, M. Creatore, S. B. S. Heil, M. C. M. van de Sanden, and W. M. M. Kessels, *Appl. Phys. Lett.* **89**, 081915 (2006).
- [15] M. M. Frank, Y. J. Chabal, and G. D. Wilk, *Appl. Phys. Lett.* **82**, 4758 (2003).
- [16] J. B. Peri, *J. Phys. Chem.* **69**, 220 (1965).
- [17] H. Knözinger and R. Ratnasamy, *Catal. Rev.-Sci. Eng.* **17**, 31 (1978).
- [18] C. Morterra and G. Magnacca, *Cat. Today* **27**, 497 (1996).
- [19] H. A. Al-Abadleh and V. H. Grassian, *Langmuir* **19**, 341 (2003).
- [20] J. M. Roscoe and J. P. D. Abbatt, *J. Phys. Chem. A* **109**, 9028 (2005).
- [21] A. Rahtu, T. Alaranta, and M. Ritala, *Langmuir* **17**, 6506 (2001).
- [22] S. B. S. Heil, F. Roozeboom, M. C. M. van de Sanden, and W. M. M. Kessels, *J. Vac. Sci. Technol. A* **26**, 472 (2008).

Chapter 5

In situ spectroscopic ellipsometry as a versatile tool to study atomic layer deposition*

Abstract

The application of *in situ* spectroscopic ellipsometry (SE) during thin film synthesis by atomic layer deposition (ALD) is discussed. The versatility of this all-optical diagnostic is demonstrated by results obtained on Al_2O_3 , HfO_2 , Er_2O_3 , TiO_2 , Ta_2O_5 , TiN , and TaN_x films with thicknesses ranging from 0.1 to 100 nm. By acquiring SE data in between the ALD cycles and by analyzing the film thickness and the energy dispersion of the optical constants of the films, the layer-by-layer growth and material properties of the films can be studied in detail. The growth rate per cycle and the ALD saturation curves can be determined directly by monitoring the film thickness as a function of the number of cycles, while also the nucleation behavior of the films on various substrates and submonolayer surface changes during the ALD half-cycles can be probed. The energy dispersion relation provides information on the optical properties, the crystalline phase, and material composition of the films. For metallic films, electrical properties can be calculated from the Drude absorption yielding insight into the electrical resistivity and electron scattering effects in ultrathin films.

*Submitted for publication: E. Langereis, S. B. S. Heil, H. C. M. Knoops, W. Keuning, M. C. M. van de Sanden, and W. M. M. Kessels

I Introduction

The deposition of nanometer thick or ultrathin films with well-defined film properties has become of vital importance for present and future technology nodes in the semiconductor industry [1], while it is also essential for developments in the growing field of nanotechnology in general. Currently, atomic layer deposition (ALD) is considered one of the primary candidates for the deposition of ultrathin films with precise growth control. On the virtue of two self-limiting surface reactions and by the cycle-wise alternate exposure of the substrate surface to at least two volatile reactants, ALD provides layer-by-layer growth control, high uniformity, and excellent conformality on substrates with demanding topologies [2, 3]. The successful integration of such ultrathin films in industrial applications relies, however, not only on the development of methods to synthesize these ultrathin films, but also on the availability of accurate analytical or metrology techniques to determine the thickness and properties of these films. With the material properties of various ALD processes extensively being reported in the literature [2–6], the focus of this paper lies on the characterization of the ALD films by an *in situ* method that yields basic and fast understanding of ALD film growth and with the potential for online process control in industrial applications.

Ultrathin films are often characterized by means of *ex situ* diagnostics, such as transmission electron microscopy (TEM), x-ray reflectometry and diffraction (XRR and XRD), Rutherford backscattering spectroscopy (RBS), x-ray photoelectron spectroscopy (XPS), Auger electron spectroscopy (AES), four-point probe (FPP), and low and medium energy ion scattering (LEIS/MEIS). These techniques provide information on film thickness, microstructure, atomic composition, electrical resistivity, nucleation, and film closure of the ultrathin films. However, recently more emphasis has been put on *in situ* diagnostics for online process monitoring and for control of the deposition process at the atomic level. For ALD, one clear advantage of *in situ* monitoring can be illustrated by considering the determination of the film thickness and the growth rate per cycle. These are among the most relevant parameters of an ALD process. Generally the growth rate is determined by depositing one or a few films of various thicknesses and by dividing the final film thickness over the total number of ALD cycles used. In turn, this growth rate is employed to predict the amount of cycles required to deposit films with the thickness targeted. It has to be realized, however, that the growth rate is not necessarily constant during the complete deposition process and often varies with film thickness

Table 5.1: Overview of the ALD materials that were studied by *in situ* spectroscopic ellipsometry. The precursors and reactants used in the ALD processes are shown as well as the deposition temperature. The ALD temperature window studied is indicated for every material in between parentheses.

Material	Precursor gas	Reducing/Oxidizing agent	Temperature (°C)	Refs.
Al ₂ O ₃	Al(CH ₃) ₃ ^a	O ₂ plasma	100 (25–300)	[7–10]
HfO ₂	Hf[N(CH ₃)(C ₂ H ₅)] ₄ ^b	O ₂ plasma	290 (230–350)	[11]
Er ₂ O ₃	Er(thd) ₃ ^c	O ₂ plasma	300 (150–300)	
TiO ₂	Ti[OCH(CH ₃) ₂] ₄ ^d	O ₂ plasma	300 (25–300)	[12]
Ta ₂ O ₅	Ta[N(CH ₃) ₂] ₅ ^e	O ₂ plasma	225 (100–225)	[13]
TiN	TiCl ₄ ^f	H ₂ -N ₂ (10:1) plasma	400 (100–400)	[11, 14, 15]
TaN _{x,x≤1}	Ta[N(CH ₃) ₂] ₅ ^e	H ₂ plasma	225 (150–250)	[16]
Ta ₃ N ₅	Ta[N(CH ₃) ₂] ₅ ^e	NH ₃ plasma	225 (150–250)	[16]

^aTrimethylaluminum (TMA)

^bTetrakis(ethylmethyamido)hafnium (TEMAH)

^cErbium(2,2,6,6-tetramethyl-3,5-heptanedionate)₃ (Er(thd)₃)

^dTitaniumisopropoxide (TTIP)

^ePentakis(dimethylamino)tantalum (PDMAT)

^fTitaniumchloride

for ultrathin films. For example due to nucleation effects, the film growth can initially be inhibited or accelerated such that it can take a considerable amount of cycles before the thickness increases linearly with the number of ALD cycles (i.e., a constant growth rate per cycle). In order to accurately predict the film thickness targeted, the nucleation behavior should, therefore, be established in detail on the various substrates and under the different conditions employed. Obviously, the growth behavior of a certain ALD process can be determined much easier and faster by acquiring *in situ* data on the film thickness during the deposition process. Similar arguments hold for the determination of ALD saturation curves, investigation of the half-cycles, and the measurement of optical, structural, and even electrical properties of the films.

Spectroscopic ellipsometry (SE) is an optical technique renowned for determination of the film thickness and the optical constants over a wide photon energy range and it is commonly applied *in situ* to study film growth by physical and chemical vapor deposition techniques [17, 18]. It is a non-intrusive diagnostic that can be applied on-substrate to study the film growth on various materials relevant for ALD, including wafer-like

substrates (e.g., Si, Ge, GaAs) and metallic and polymeric foils, etc. The sensitivity of SE is, in principle, sufficient to detect changes of the nominal thickness of surface layers equivalent to 0.01 monolayer [17, 19]. The latter makes SE particularly suited for studies of ALD growth of ultrathin films with submonolayer growth control. The most important requirements to employ *in situ* SE during ALD is optical access on the reactor and the deposition on optically flat substrates that allow for specular reflection of the ellipsometer light.

In this paper, several merits of the application of *in situ* spectroscopic ellipsometry for studying thin film synthesis by ALD are discussed. The versatility of SE will be demonstrated by typical results obtained for (plasma-assisted) ALD of Al_2O_3 , HfO_2 , Er_2O_3 , TiO_2 , Ta_2O_5 , TiN, and TaN_x films (cf. Table 5.1). It will be shown that:

- i. From the increase in film thickness monitored as a function of a number of cycles the growth rate per cycle can be calculated *during* the ALD process;
- ii. The ALD saturation curves can be obtained in a *single* deposition run by determination of the growth rate per cycle under various process conditions;
- iii. The nucleation behavior of the films on various substrates can be studied by acquiring data after every ALD cycle during initial film growth;
- iv. Submonolayer level changes after precursor and reactant steps can be probed by acquiring data after every ALD half-cycle;
- v. Optical film properties, such as refractive index, extinction coefficient, and optical band gap, can be obtained from the energy dispersion of the optical constants;
- vi. For particular materials, insight into crystalline phase and composition of the films can be derived from the “shape” of the energy dispersion;
- vii. From the Drude absorption by conduction electrons in metallic films electrical properties can be calculated such as electrical resistivity, electron mean free path, and conduction electron density; and
- viii. Insight into aspects relevant for ultrathin metallic films such as electron-impurity scattering and size effects can be obtained from ellipsometry data.

The remainder of the paper is organized as follows: In Sec. II, the principle of spectroscopic ellipsometry and the measurement procedure during ALD film growth are briefly discussed. Subsequently, in Sec. III the optical parametrizations employed to describe the energy dispersion of the optical constants of several materials are presented. In Sec. IV, several examples relevant to ALD and ultrathin film growth are discussed to clearly illustrate the merits of *in situ* SE. Finally, the conclusions of this work are summarized in Sec. V.

II Spectroscopic ellipsometry

A. Basics of spectroscopic ellipsometry

Ellipsometry is based on the measurement of the change in polarization of a light beam upon reflection from a surface [17]. Therefore an ellipsometer system basically consists of a light source and a detector unit. With the light source and a set of optical components, such as polarizers and retarders, the polarization of the incoming light on a surface is defined. In turn, the polarization of the reflected light is determined by another polarizer in combination with the detector, either a photodiode, diode-array or photomultiplier tube. Various ellipsometer systems are (commercially) available with many variations in the configuration of polarizers and retarders, each having their specific merits as discussed extensively in the literature [17, 19].

The ellipsometry data can be expressed in terms of the amplitude ratio Ψ and phase angle Δ . These parameters are related to the complex Fresnel reflection coefficients via the complex ellipsometric parameter ρ :

$$\rho = \frac{R_p}{R_s} = \tan\Psi e^{i\Delta}, \quad (5.1)$$

where R_p and R_s are the complex Fresnel reflection coefficient for *p*- and *s*-polarized light, respectively. In spectroscopic ellipsometry (SE), the polarization change is determined for a set of wavelengths in a certain photon energy range. From the ellipsometric data obtained, the film thickness and the dispersion relation of the optical constants over the photon energy range can be deduced. The optical constants can be expressed in the refractive index n and extinction coefficient k , but they are often represented in terms of the real (ε_1) and imaginary (ε_2) part of the complex dielectric function ε . The latter are related through the definitions $\varepsilon_1 = n^2 - k^2$ and $\varepsilon_2 = 2nk$ with the additional requirement that the real and imaginary part

of the dielectric function are Kramers-Kronig consistent [17]. From the optical constants, several material properties of thin films can be derived such as the optical band gap of dielectric materials or the conductive properties of metal nitrides. This will be discussed in more detail in Secs. III and IV.

The raw data obtained from the measurements contain the change in polarization caused by the interaction of the light with the (multi-layered) sample and are often expressed in the parameters Ψ_{exp} and Δ_{exp} or the pseudo-dielectric function $\langle \varepsilon \rangle_{\text{exp}}$, which are related via [17]:

$$\langle \varepsilon \rangle = \langle \varepsilon_1 \rangle + i\langle \varepsilon_2 \rangle = \sin^2(\phi) \left[1 + \left(\frac{1 - \rho}{1 + \rho} \right)^2 \tan^2(\phi) \right], \quad (5.2)$$

where the angle of incidence is given by ϕ and the quantity ρ is defined by Eq. 5.1. For semi-infinite (or opaque) bulk samples where a surface oxide layer or surface roughness can be neglected, the pseudo-dielectric function is per definition equal to the dielectric function of the material of the sample. In that case, the dielectric function of the opaque film can be directly obtained from the ellipsometric parameters via Eq. 5.2. In other cases the sample is treated as a multi-layered sample and the dielectric function of each layer can be extracted through model-based analysis of the data, as will be discussed below.

B. *In situ* data acquisition

In order to monitor the ALD process *in situ*, the reactor must be equipped with two optical access ports. Generally fused silica optical windows (transparency range $\sim 180\text{--}2000\text{ nm}$) are well-suited to transmit the SE light beam. Film deposition on these optical windows has to be prevented and, therefore, protective gate valves are preferably present between the reactor chamber and these windows. In Fig. 5.1(a), a typical configuration of ellipsometer light source and detector on an ALD reactor is schematically represented. Figure 5.1(b) shows a photograph of a ALD reactor equipped with *in situ* SE. The angle of incidence of the light beam ($0 < \phi < 90^\circ$ with respect to the normal of the substrate) is generally restricted to a fixed angle by reactor design with an optimal sensitivity for the SE measurements when the angle of incidence is close to the Brewster angle of the substrate (e.g., for silicon-based substrates $\sim 75^\circ$) [17]. Obviously, the spot size of the light beam on the substrate increases with increasing angle of incidence limiting the minimal substrate size and defining the measurement area.

Before the start of the ALD process, the optical response of the substrate is determined to facilitate the optical modeling of the ALD film in

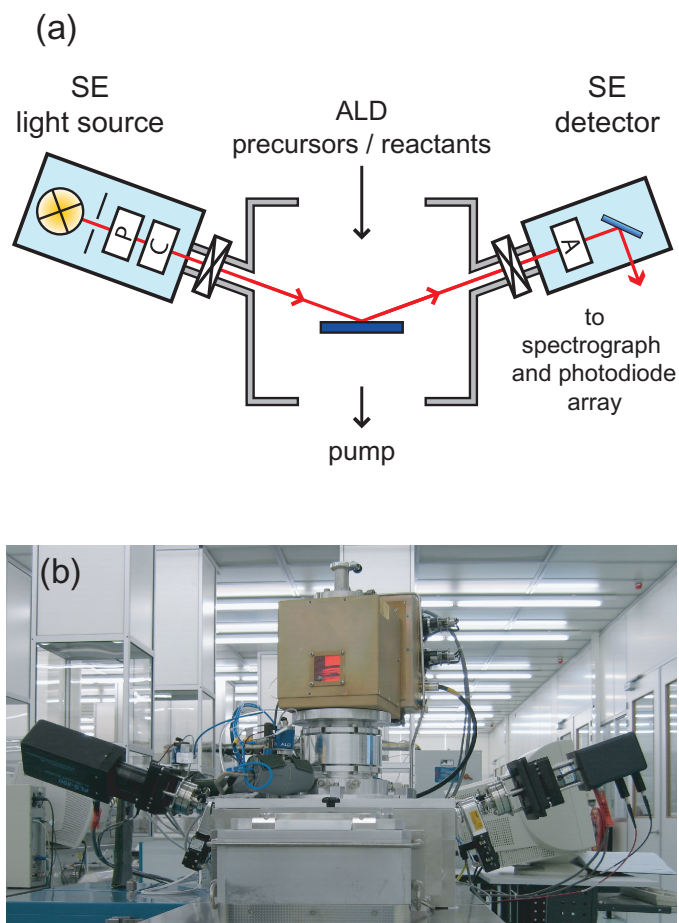


Figure 5.1: Experimental configuration of *in situ* spectroscopic ellipsometry (SE) on an ALD reactor. (a) Schematic representation with a rotating compensator ellipsometer and gate valves to protect the optical view ports. The SE light source with lamp, fixed polarizer (P), and rotating compensator (C), and the SE detector with fixed analyzer (A) and fiber coupling to the spectrograph are indicated. (b) Photograph of a J.A. Woollam, Inc., M2000 spectroscopic ellipsometer fitted on an Oxford Instruments FlexAL™ ALD reactor.

a later stage. Subsequently, the SE gate valves are closed and a number of ALD cycles is carried out before acquiring new SE data. It is obvious that the cyclic ALD process with a step-wise increase in film thickness allows for sensitive SE measurements, because the deposition process is intrinsically halted after every ALD cycle. The data acquisition time can, therefore, be taken as long as necessary for a sufficient high signal-to-noise ratio. After the SE measurement, the gate valves are closed and the deposition process is continued. Typically cycle-by-cycle data is acquired to address the nucleation behavior of the ALD films on a substrate material, while data acquisition after every 10–100 cycles is used to study the ALD growth in the linear “bulk” growth regime.

C. Optical modeling

Physical information on the sample can be extracted through model-based analysis of the experimental data. In general a multilayer model is built, where each layer is characterized by a certain thickness and optical dispersion relation. Ellipsometry software is used to calculate the optical response of all the layers combined into the ellipsometric parameters Ψ_{mod} and Δ_{mod} of the model. The extent to which the model describes the experimental data, i.e., the quality of the model, is expressed by the difference between the simulated and experimental data, often defined by the mean squared error (MSE) of the model [19]:

$$\text{MSE} = \sqrt{\frac{1}{2N - M} \sum_{i=1}^N \left[\left(\frac{\Psi_i^{\text{exp}} - \Psi_i^{\text{mod}}}{\sigma_{\Psi,i}^{\text{exp}}} \right)^2 + \left(\frac{\Delta_i^{\text{exp}} - \Delta_i^{\text{mod}}}{\sigma_{\Delta,i}^{\text{exp}}} \right)^2 \right]}, \quad (5.3)$$

where N is the number of measured wavelengths in the photon energy range, M is the number of fit parameters in the model, and $\sigma_{\Psi,i}^{\text{exp}}$ and $\sigma_{\Delta,i}^{\text{exp}}$ are the standard deviations of the experimental data points at a certain photon energy. After manually selecting fit parameters, the software fitting routine aims to minimize the MSE by using an iterative Levenberg-Marquardt algorithm.

Most of the ALD film depositions are simulated by a two-layer model, i.e., the substrate and the ALD film, and only additional layers are added when the model requires more complexity, such as due to the formation of an interfacial layer or due the development of surface roughness during the ALD process. Basic assumptions of the models used are that the substrate optical properties are not changed during deposition and that the ALD film has a sharp interface with the substrate. For most ALD processes,

the films deposited have a small surface roughness [typically <0.2 nm as determined by atomic force microscopy (AFM)] and a surface roughness layer can be omitted in the optical models.

The optical modeling starts with describing the optical response of the substrate that was determined before the start of deposition to clearly distinguish the substrate from the ALD film in the data modeling. When wafer-like substrates are used, such as Si, Ge, GaAs wafers (as is the case in this paper), these substrates can be considered semi-infinite because they are optically thick (>200 μm). When these substrates are native oxide covered, this means that after defining the thickness and dielectric function of the native oxide, the dielectric function of the substrate can be obtained via a wavelength point-to-point exact numerical inversion of the experimental data. As a consequence, the model perfectly describes the optical response of the substrate prior to film growth. For some plasma-assisted ALD processes where the plasma exposure is known to slightly affect the substrate (e.g., by oxidation or nitridation), the substrate is often first pre-exposed to the plasma used in the ALD process. In this way, the plasma effect on the substrate is isolated from the ALD film growth and the substrate modeling can be adjusted to take the substrate modification into account. Subsequently in the data analysis of the ALD films, the change in ellipsometry data with deposition cycles can be completely assigned to changes in the thickness and optical properties of the growing ALD film.

In general two approaches can be followed to extract film parameters from the SE data obtained for the ALD films: (i) The film thickness can be extracted by assuming a certain dispersion relationship of the optical constants while simultaneously also optimizing the model parameters and, hence, the dispersion relation of the material concerned; (ii) The dispersion of the optical constants can be extracted by a point-to-point numerical inversion when information on the film thickness is available from another technique or when an educated guess can be used as a starting point. In the latter case, the method of direct numerical inversion can be applied iteratively to extract both the film thickness and the dielectric function of the material from the pseudo-dielectric function of the sample [17, 20]. This method works best when a sharp optical feature is present in the dielectric function of the substrate material in the energy range probed, such as, e.g., the critical points in the dielectric function of silicon. Assuming that the substrate properties are not affected by the deposition, trial spectra of ε_1 and ε_2 are obtained by a wavelength point-to-point exact numerical inversion using trial thicknesses. This procedure is repeated for several trial

thicknesses. Finally, the correct film thickness can be determined from the criterion that the resulting ε_1 and ε_2 spectra should be smooth and free of unphysical artifacts such as strange (oscillatory) features. Furthermore, the ε_1 and ε_2 spectra obtained must be Kramers-Kronig consistent, which implies that they can be described by an optical parameterization as discussed in Sec. III.

The other approach to extract the dispersion relation is to start with a pre-defined dispersion relationship for the ALD film, for example based on the film modeling obtained in previous work or based on an theoretical oscillator model. This dispersion relation is, in turn, used to determine the film thickness and to optimize the model parameters in an iterative process. In the literature, good starting conditions for the dispersion relations can be found from several ellipsometry studies available for all kind of materials which are mostly deposited by physical or chemical vapor deposition processes. Typical examples are a Cauchy relationship and a Tauc-Lorentz oscillator model for transparent and semi-transparent materials, respectively (see Sec. III) [21, 22].

A combination of both approaches is convenient for films that have a non-absorbing region in their dielectric function. The film thickness can accurately be determined employing a standard Cauchy relation (see Sec. III) to describe the dispersion in the non-absorbing region. The dispersion of the optical constants in the total photon energy range is subsequently obtained via a direct numerical inversion using the as-determined film thickness. For further analysis, an optical model can be built afterwards to parametrize the dispersion relation.

The model parameters of the ALD films are best optimized for films that have bulk-like material properties and are typically obtained for films with a thickness larger than ~ 25 nm. The parameters determined can be used as starting conditions to model the data obtained at earlier stages of the deposition and, if relevant, to study the change in material properties with film thickness. However within a good approximation, the model parameters can often be assumed constant with thickness. In addition, in most cases the film thickness does not critically depend on the model parameters and can therefore be accurately determined using the non-optimized fit parameters, as long as the dispersion of the optical constants is appropriate. This aspect makes the data analysis as a function of film thickness much less laborious. The change in film thickness with number of ALD cycles can be obtained by the model parameters optimized for the final thickness and by using the thickness as the only fit parameter [23].

III Parametrization of dielectric functions

In this section, the optical parametrizations used to describe the dielectric functions of several ALD films are discussed in more detail. The accuracy of the optical parametrizations is established by comparing their dielectric functions to the dielectric functions obtained by the method of direct numerical inversion. The typical dielectric functions in the photon energy range of 0.75–6.5 eV and the model parameters associated are shown in Fig 5.2 and Table 5.2, respectively. These can serve as a reference for future film analysis.

A. Aluminum oxide (Al_2O_3)

Crystalline aluminum oxide has an optical band gap of $E_{opt} \sim 8.8$ eV [24] and is, as a consequence, non-absorbing ($k = \varepsilon_2 = 0$) over the total photon energy measurement range of ellipsometers commonly applied. Therefore, a standard Cauchy relationship can be used to describe the dispersion of the refractive index n [21]:

$$n = A_n + \frac{B_n}{\lambda^2} + \frac{C_n}{\lambda^4}, \quad (5.4)$$

in which A_n , B_n , and C_n are the Cauchy fit parameters that are often represented for wavelength λ in micrometer units. Figure 5.2(a) shows the dispersion relation of a 109 nm thick amorphous Al_2O_3 film as determined from direct numerical inversion and as described by the Cauchy relation. The inversion data clearly shows that the extinction coefficient is indeed negligible small which validates the Cauchy model employed. It has been found that for thin films (<10 nm), the dispersion relation can be obtained using the film thickness and Cauchy parameters A_n and B_n as fit parameters. For thicker films also the parameter C_n is required to improve the fit to the data, which indicates that another high-energy oscillator starts influencing the shape of the dielectric function. The refractive index of the ALD Al_2O_3 films is 1.63 ± 0.02 at 1.96 eV, which is in the range of 1.6–1.7 reported for bulk-like Al_2O_3 films [25, 26].

B. Hafnium oxide (HfO_2)

HfO_2 is a band gap material with an optical band gap around ~ 5.7 eV [24, 27, 28], which falls in the photon energy range of some of the ellipsometer systems. The dielectric function can be determined by the method described in Sec. II. First the film thickness can be extracted from the

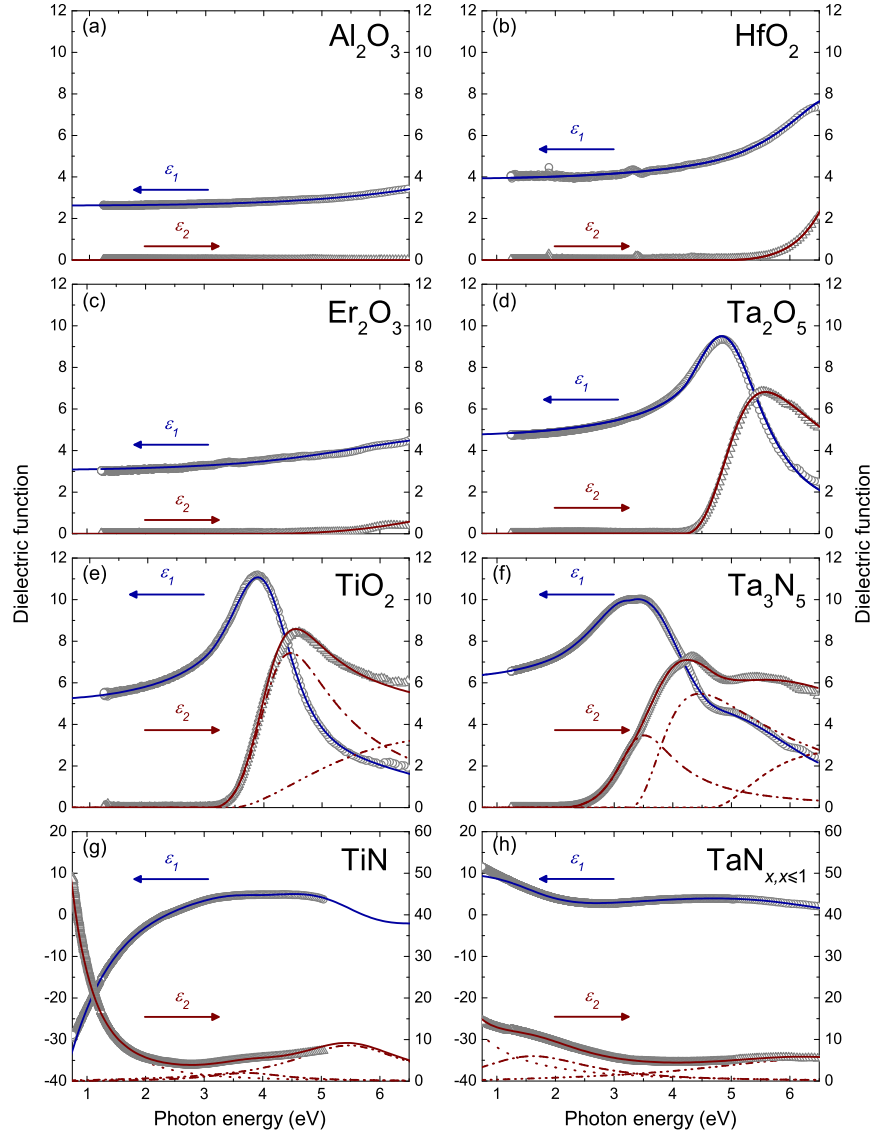


Figure 5.2: Real (ε_1) and imaginary (ε_2) part of the dielectric function as obtained by direct inversion (ε_1 = open circles, ε_2 = open triangles) and described by the optical parametrizations (ε_1 = solid blue line, ε_2 = solid brown line): (a) Al_2O_3 [Cauchy], (b) HfO_2 [Tauc-Lorentz], (c) Er_2O_3 [Tauc-Lorentz], (d) Ta_2O_5 [Tauc-Lorentz], (e) TiO_2 [Tauc-Lorentz], (f) Ta_3N_5 [Tauc-Lorentz], (g) TiN [Drude-Lorentz], and (h) conductive $\text{TaN}_{x,x \leq 1}$ [Drude-Lorentz]. The optical parametrizations used are indicated in between parentheses. The dotted/dashed lines indicate the separate contributions of the oscillators to the imaginary part of the dielectric function.

Table 5.2: Model parameters of the optical parametrizations used to describe the dielectric functions of the films deposited by ALD. The parametrizations employed are the Cauchy model [Al₂O₃], the Tauc-Lorentz oscillator model [HfO₂, Er₂O₃, Ta₂O₅, TiO₂ (two oscillators), and Ta₃N₅ (three oscillators)], and the Drude-Lorentz oscillator model [TiN and TaN_{*x,x*≤1}]. The refractive indices at 1.96 eV and the Tauc optical band gaps are also given.

ALD process		SE model parameters						Material properties	
Thickness (nm)	A_n	B_n (μm^2)	C_n (μm^4)	E_{0j} (eV)	Γ_j (eV)	E_{gj} (eV)	ε_∞	Refractive index	Band gap (eV)
Al ₂ O ₃	1.621±0.001	(2.6±0.1)·10 ⁻³	(2.04±0.05)·10 ⁻⁶					1.63±0.02	^a
HfO ₂	108±3	7.23±0.01	1.61±0.04	4.92±0.02	2.52±0.04			2.00±0.02	5.77±0.09
Er ₂ O ₃	19±2	7.7±0.2	4.1±0.3	4.0±0.1	1	205±10		1.78±0.02	4.8±0.2
Ta ₂ O ₅	320±9	4.98±0.03	1.77±0.08	4.21±0.01	2.37±0.05			2.23±0.02	4.26±0.05
TiO ₂	150±8 197±8	4.17±0.01 5.5±0.3	1.52±0.02 11±500	3.11±0.01 3.44±0.07	0.3±0.1			2.42±0.02	3.28±0.02
Ta ₃ N ₅	27±1 265±12 288±10	3.41±0.01 3.69±0.03 4.66±0.06	1.22±0.03 1.65±0.02 3.14±0.09	2.08±0.01 3.27±0.01 5±1000	1.61±0.03			2.68±0.02	2.45±0.02
	$\hbar\omega_{pu}$ (eV)	$\hbar\Gamma_D$ (eV)	f_i	$\hbar\omega_{0i}$ (eV)	$\hbar\tau_i$ (eV)	ε_∞			
TiN	7.22±0.05	0.86±0.05	0.8±0.2 3.5±0.3	3.8±0.1 5.6±0.1	1.6±0.1 2.3±0.3	3.0±0.1		1.30±0.02	
TaN _{<i>x,x</i>≤1}	5.5 ^b	3.40±0.06	6.8±0.2 3.49±0.06	2.00±0.01 6.75±0.03	2.51±0.05 4.62±0.09	2.22±0.05		2.70±0.02	

^a Exceeding the photon energy range (0.75–6.5 eV) of the ellipsometers used

^b Fixed parameter in Drude-Lorentz model

transparent part of the spectrum ($E < E_{opt}$) and this thickness can be used to obtain the dispersion of the optical constants by a direct numerical inversion over the total photon energy [Fig. 5.2(b)]. Subsequently, an oscillator model can be used to parametrize the imaginary part (ε_2) of the dielectric function. Although the absorption in the UV is still small and could be described by an Urbach absorption tail in combination with a Cauchy model [29], the dielectric function of the HfO₂ film can also be described by the Tauc-Lorentz oscillator model with one or more oscillators. The Tauc-Lorentz oscillator model was originally introduced by Jellison and Modine [22, 28] and is given by:

$$\begin{aligned}\varepsilon_2(E) &= \sum_{j=1}^n \frac{A_j E_{0j} \Gamma_j (E - E_{gj})^2}{(E^2 - E_{0j}^2)^2 + \Gamma_j^2 E^2} \frac{1}{E}, & E > E_{gj}, \\ &= 0, & E \leq E_{gj}.\end{aligned}\quad (5.5)$$

In Eq. 5.5, E_{gj} represents the band gap, E_{0j} is the peak transition energy, Γ_j is the broadening parameter, and A_j represents the optical transition matrix elements. The real part (ε_1) of the dielectric function can be obtained by the Kramers-Kronig integration of ε_2 [22], where the fitting parameter ε_∞ is included to compensate for the possible contribution of higher-energy transitions that are not taken into account by the Lorentz term. From the imaginary part of the dielectric function, the optical band gap (E_{opt}) can be deduced. Tauc *et al.* reported that the optical band gap can be found by plotting the parameter $\sqrt{\varepsilon_2 E^2}$ as a function of the photon energy [30]. In turn, the Tauc band gap is defined as the photon energy where the extrapolation of the linear part of this parameter intersects the line $\sqrt{\varepsilon_2 E^2} = 0$ [30, 31].

Figure 5.2(b) shows the dispersion relation as obtained by direct numerical inversion and as described by the Tauc-Lorentz oscillator model. The ALD HfO₂ film required only a single oscillator ($n = 1$ in Eq. 5.5) to parametrize the dielectric function. Additional Tauc-Lorentz oscillators can be used to account for crystalline fractions or higher energy transitions [28], but these additional oscillators appeared not necessary for the current HfO₂ film which was fully amorphous (as revealed by x-ray diffraction analysis). The model parameters listed in Table 5.2 are close to the values reported by Cho *et al.* and the small differences observed can be attributed to the fact the parameters are influenced by deposition temperature and the crystalline fraction observed in their films [28]. The small features around 1.9 eV, 3.4 eV, and 4.3 eV in the inversion data indicate that the film thickness assumed in the direct inversion analysis is very

close but not exactly equal to the real film thickness. Some of these small peaks originate from critical points in the dielectric function of the silicon substrate (around ~ 3.4 eV and ~ 4.4 eV [32]), as has also been reported by Cho *et al.* [28]. The small discrepancy in the inversion data might indicate that the substrate has slightly been affected during the ALD process, e.g., through the formation of some interfacial oxide on the H-terminated Si substrate used. This implies that the two-layer model used for the direct inversion has to be changed accordingly to obtain a perfectly smooth dielectric function. The optical Tauc band gap of the HfO₂ film is 5.77 ± 0.09 eV which is in excellent agreement with the literature value [24, 27, 28].

C. Erbium oxide (Er₂O₃)

Er₂O₃ has an optical band gap in the range of 4.8–7.5 eV and its dispersion of the optical constants has only recently been reported in the literature [33, 34]. Losurdo *et al.* used a Lorentzian oscillator to parametrize the dielectric function [34], but also a Tauc-Lorentz oscillator model can be chosen. Instead of using the commonly-applied parameter ε_∞ , the description of the dielectric function ε_1 can also be improved by including a high-energy, lossless pole $\varepsilon_p = A_p/(E_p^2 - E^2)$, which has an amplitude A_p and a peak position at energy $E_p = 11$ eV (i.e., far outside the SE photon energy range probed). The advantage of such a high-energy pole lies in the fact that the dielectric function ε_1 is offset by a Cauchy-shaped dispersion rather than the constant value ε_∞ , while the dielectric function ε_2 is not affected. The dielectric functions as obtained by direct numerical inversion and the Tauc-Lorentz oscillator model are shown in Fig. 5.2(c) and the model parameters are listed in Table 5.2. The dispersion in the dielectric function is in good agreement with the energy dispersion reported by Losurdo *et al.*, who reported that the optical constants of Er₂O₃ depended on deposition temperature and substrate material employed [33, 34]. The bandgap $E_{opt} = 4.8 \pm 0.2$ eV and the refractive index $n = 1.78 \pm 0.02$ are within the ranges of 4.8–7.5 eV and 1.5–2.1, respectively, reported in the literature [33, 34].

D. Tantalum oxide (Ta₂O₅)

Ta₂O₅ has an optical band gap of 3.8–4.4 eV depending on the crystalline phase of the film [35–38]. Similarly to HfO₂, a Cauchy model can be used to determine the film thickness from the transparent part of the photon spectrum and the dispersion relation over the total photon energy range can be

obtained by direct numerical inversion. Figure 5.2(d) shows the resulting dielectric function obtained by direct numerical inversion and the dielectric function as parametrized by the Tauc-Lorentz oscillator model. The amorphous Ta₂O₅ film required a single Tauc-Lorentz oscillator to parametrize the dielectric function. The optical band gap as determined from the imaginary part of the dielectric function was found to be $E_{opt} = 4.25 \pm 0.05$ eV. This value lies in the range of 4.2–4.4 eV reported for amorphous Ta₂O₅ films [37, 38]. The band gap of amorphous Ta₂O₅ films is typically higher than the range of 3.6–4.2 eV reported for crystalline Ta₂O₅ films [35–37].

E. Titanium oxide (TiO₂)

TiO₂ is a band gap material with an optical gap around 3.0–3.5 eV depending on its crystalline phase [39, 40]. The band gap of amorphous TiO₂ is somewhat lower than the 3.4 eV reported for anatase TiO₂ [40], but higher than the typical band gap of 3.0 eV for rutile TiO₂ [41, 42]. Again the film thickness can be determined using a Cauchy model to describe the transparent region and the resulting dielectric function from direct inversion is shown in Fig. 5.2(e). A double Tauc-Lorentz oscillator model has been used to describe the TiO₂ dielectric function and both oscillators are shown in Fig. 5.2(e). It is noted that most part of the second oscillator lies outside of the SE measurement range complicating the exact description of this oscillator. Although the broadening parameter of the second oscillator has a substantial uncertainty (Table 5.2), it does not critically influence the shape of the oscillator in the photon energy range probed. From the dielectric function it is deduced that the amorphous TiO₂ film has an optical band gap $E_{opt} = 3.28 \pm 0.02$ eV, which is in good agreement with the band gap of 3.27 eV reported by Zhang *et al.* [39].

F. Titanium nitride (TiN)

TiN is a conductive metal nitride and the film is absorbing in the full photon energy range of ellipsometer systems in the visible and near-infrared wavelength range. As a consequence, the film thickness can not be determined using a Cauchy model as was used for the (semi)-transparent oxides. However, the TiN film becomes opaque at a certain thickness (typically >60 nm) and the pseudo-dielectric function of thick films can be used to define the TiN dielectric function. The pseudo-dielectric function of a 65 nm thick TiN film with a negligible small surface roughness (~ 0.4 nm as determined by AFM measurements) can, therefore, be interpreted as the

TiN dielectric function. Subsequently, a Drude-Lorentz oscillator model can be built to parametrize the dielectric function as described below. For thinner TiN films, the film thickness can also be obtained by the method of direct inversion. On the other hand, also the Drude-Lorentz oscillator parameters of the opaque film can be used as starting conditions for an iterative fitting procedure to determine the thickness and the dielectric function of the thinner TiN films.

The intraband absorption by the free conduction electrons in the material can be described by an oscillator based on Drude theory [43]. This absorption is particularly evident when probed deep in the near-infrared energy range (e.g., down to 0.75 eV for the infrared-extended ellipsometer employed in this work). The interband absorption at higher photon energy can be accounted for by adding Lorentz oscillators to the optical parametrization. Following previous work [15, 44, 45], the dielectric function of TiN can be parametrized by the combination of one Drude and two Lorentz oscillators:

$$\varepsilon(\omega) = \varepsilon_\infty - \frac{\omega_{\text{pu}}^2}{\omega^2 - i\Gamma_D\omega} + \sum_{j=1}^2 \frac{f_j\omega_{0j}^2}{\omega_{0j}^2 - \omega^2 + i\gamma_j\omega}. \quad (5.6)$$

In Eq. 5.6, ε_∞ is equal or larger than unity to compensate for the contribution of higher-energy transitions that are not taken into account by the Lorentz terms. The Drude term is characterized by the unscreened plasma energy $\hbar\omega_{\text{pu}}$ and the damping factor Γ_D . The Lorentz oscillators are located at energy position $\hbar\omega_{0j}$, with strength f_j , and damping factor γ_j . For TiN, the two Lorentz oscillators account for interband absorptions around ~ 3.5 and ~ 5.2 eV [44, 46, 47].

In Fig. 5.2(g) the dielectric function of an 11.7 nm thick TiN film is shown as obtained by direct inversion and as described by the Drude-Lorentz oscillator model. It is clear from the overlap of the two approaches that the Drude-Lorentz oscillator model accurately describes the dispersion of the dielectric function of this thin TiN film.

From the Drude oscillator parameters, material parameters such as the conduction electron density (N_e), the mean free path (MFP) of the conduction electrons, and the electrical resistivity (ρ) can be calculated

according to Drude theory [15, 43, 45]:

$$N_e = \left(\frac{\varepsilon_0 m^*}{e^2} \right) \omega_{\text{pu}}^2, \quad (5.7)$$

$$\text{MFP} = \hbar \left[\frac{3\pi^2 \varepsilon_0}{(m^* e)^2} \right]^{1/3} \frac{\omega_{\text{pu}}^{2/3}}{\Gamma_D}, \quad (5.8)$$

$$\rho = \left(\frac{1}{\varepsilon_0} \right) \frac{\Gamma_D}{\omega_{\text{pu}}^2}, \quad (5.9)$$

where ε_0 is the permittivity of free space, m^* is the electron effective mass, e is the electron charge, and \hbar is Dirac's constant. For TiN films, the electron effective mass has been reported to be $m^* = 1.15m_e$, in which m_e is the electron rest mass [44]. When the number of conduction electrons per atom (Z) is known, also the mass density (ρ_m) can be calculated according to:

$$\rho_m = \left(\frac{\varepsilon_0 m^* A}{e^2 N_0 Z} \right) \omega_{\text{pu}}^2, \quad (5.10)$$

where A is the atomic mass of the material and N_0 is Avogadro's number. For TiN, the number of conduction electrons per atom was estimated to be $Z = 0.95$ [44].

G. Tantalum nitride (TaN_x)

Tantalum nitride (TaN_x) exists in various crystalline phases with different material properties that range, for example, from conductive, cubic TaN to semiconductive Ta_3N_5 [48]. The Ta_3N_5 phase has an optical band gap and the dielectric function of the ALD deposited Ta_3N_5 can be parametrized by three Tauc-Lorentz oscillators (see Fig. 5.2(f) and Table 5.2).¹ The conductive TaN_x phase can, similarly to TiN, be described by the Drude-Lorentz parametrization consisting of one Drude and two Lorentz oscillators [16], as is shown in Fig. 5.2(h).

The Drude absorption by the free electrons in the TaN_x film is not as pronounced as in the TiN film (cf. Fig. 5.2). This difference is a direct consequence of the higher electrical resistivity of TaN_x . In the TaN_x film, the two Lorentz oscillators account for interband absorptions around 2.2 eV and 6.4 eV. Due to the large Lorentz oscillator positioned at low

¹The model for Ta_3N_5 involves an additional oscillator compared to the model reported in our previous work (Ref. [16]). This third oscillator was found to significantly improve the fit of the dielectric function.

energy, the amplitude and broadening of the Drude oscillator could not unambiguously be determined for this film and, therefore, the Drude amplitude has been set as a fixed parameter. However, the ratio $\Gamma_D/\omega_{\text{pu}}^2$ of the Drude oscillator parameters has been found to be uniquely defined and can therefore accurately be determined. Since the electrical resistivity is defined by the ratio of the Drude oscillator parameters (Eq. 5.9), the electrical property of the TaN_x film can still be calculated from the dielectric function [16].

In Sec. IV, it will be shown that the different TaN_x phases, which can be deposited by variation of the plasma conditions during plasma-assisted ALD [16], can be optically distinguished from the *in situ* data by examination of their dielectric functions.

IV ALD film growth studied by *in situ* SE

A. Film thickness and ALD growth rate

The film thickness is among one of the most important parameters for the application of thin films in devices. In ALD, this thickness can be precisely controlled by selecting the appropriate number of ALD cycles. In this respect, monitoring the film thickness by an *in situ* technique allows to determine the film thickness at any stage during the ALD process. Moreover, such a technique provides the opportunity to control the process such that the film deposition can be actively stopped when the thickness targeted has been reached. Furthermore, from the change in film thickness with the number of cycles, the typical ALD growth rate per cycle can be calculated during film growth.

The film thickness as a function of ALD cycles as determined by *in situ* SE is shown in Fig. 5.3 for ALD processes of metal oxides (Al_2O_3 , TiO_2 , and Ta_2O_5) and metal nitrides (Ta_3N_5 , $\text{TaN}_{x,x\leq 1}$, and TiN). In these cases the data was typically acquired after every 10, 20 or 50 cycles. The final thickness deduced from the SE measurements was corroborated by thickness measurements by x-ray reflectometry. As generally expected for an ALD process, the film thickness increases linearly with the number of deposition cycles, although in some cases a (pronounced) film nucleation effect can occur (cf. Sec. III C). The growth rate, i.e., the amount of material deposited per cycle, can be obtained from linear regression analyses of the data for the linear region. For the data in Fig. 5.3 this resulted in growth rates of 0.118 ± 0.005 , 0.080 ± 0.005 , and 0.045 ± 0.005 nm/cycle for the Al_2O_3 , Ta_2O_5 , and TiO_2 films, respectively, and growth rates

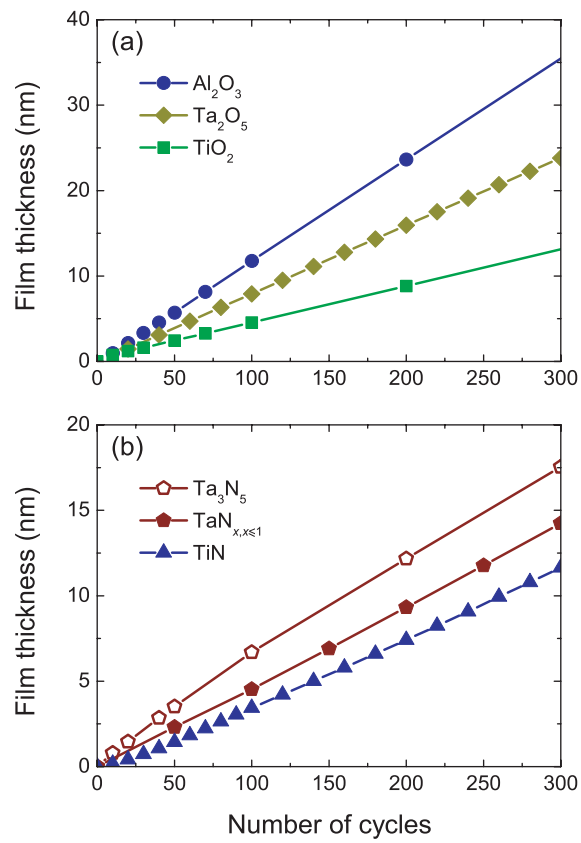


Figure 5.3: Thickness of (a) the metal oxide films: Al_2O_3 , Ta_2O_5 , and TiO_2 and (b) the metal nitride films: Ta_3N_5 , $\text{TaN}_{x,x \leq 1}$, and TiN as a function of number of ALD cycles as determined from the *in situ* SE measurements.

of 0.054 ± 0.005 , 0.049 ± 0.005 , and 0.041 ± 0.005 nm/cycle for the Ta_3N_5 , $\text{TaN}_{x,x \leq 1}$, and TiN films, respectively. It is noted that the growth rates of ALD processes typically are (considerably) smaller than one monolayer ($\sim 2\text{--}3 \text{ \AA}$) per cycle. Among others, this can be related to the number of adsorption sites available on the surface and to steric hindrance effects during precursor adsorption.

In conclusion, compared to *ex situ* techniques that require a thickness series to determine the growth rate for a certain ALD condition, the *in situ* technique of SE provides immediate information on film thickness and growth rate by monitoring the ALD process directly.

B. ALD saturation curves

Another important aspect of ALD, especially during design and setup of new processes, is the self-limiting ALD surface chemistry. This self-limiting character implies that the growth rate becomes independent of the precursor and reactant dosages used in the ALD process, indicating that these dosages are sufficient to saturate both ALD half-reactions. This important aspect of ALD can be demonstrated by constructing the so-called ALD saturation curves in which the growth rate is plotted as a function of the ALD process parameter, such as the precursor and reactant dosages, the purge times in between both ALD half-cycles, and the deposition temperature. For example when using *ex situ* methods, this basically involves that for each ALD process parameter studied, (at least) two films of different thickness have to be deposited. Subsequently, the growth rate can be calculated by dividing the difference in thickness over the difference in cycles employed. In this way, the determination of the ALD saturation curves for the process parameters becomes, obviously, a laborious task when using *ex situ* methods.

The ability to extract the growth rate by a linear regression to the *in situ* data (cf. Fig. 5.3) allows for a fast determination of the ALD growth saturation in a *single* deposition run. This is demonstrated in Fig. 5.4 for ALD of TiN in which the influence of the plasma exposure time on the growth rate is determined. For an interval of only 60 cycles (corresponding to ~ 4 nm TiN), the change in film thickness with ALD cycles is monitored for a specific plasma exposure time and the growth rate is determined by a linear regression to the *in situ* data. To facilitate the data analysis, it was assumed that the film properties (and SE model parameters) did not vary much for the various process conditions employed. This implies that the change in thickness with cycles could be determined without optimizing all

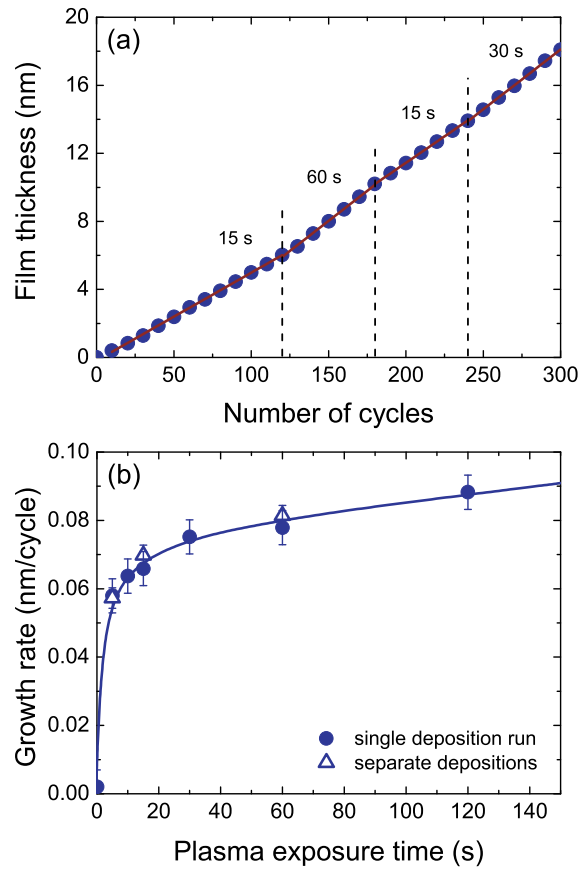


Figure 5.4: (a) The thickness of a TiN film as a function of number of ALD cycles as determined from the *in situ* SE measurements. The variation of plasma exposure time for the different intervals of ALD cycles is indicated. (b) The growth rate as a function of plasma exposure time. The growth rate is determined from a linear regression through the data points in Fig. 5.4(a). The growth rate calculated from thick films deposited separately under constant ALD conditions is also given. The line serves as guide to the eye.

parameters of the Drude-Lorentz model for each growth condition. This method is validated by the excellent agreement of this growth rate with the growth rate that has been calculated from a thick film (>30 nm) deposited under constant ALD conditions and for which all the Drude-Lorentz model parameters were optimized [Fig. 5.4(b)]. Subsequently, by a systematic variation of the plasma exposure time and determination of the growth rates from a linear regression as shown in Fig. 5.4(a), a plot of growth rate as a function of the plasma exposure time can be constructed as shown in Fig. 5.4(b). Note that the so-called “soft” saturation in growth rate with plasma exposure time observed in Fig. 5.4(b) is related to a change in film composition, as has been reported in previous work [11].

The results shown demonstrate that the determination of film thickness by SE is, in fact, very accurate. Moreover, the film thickness and growth rate can even be obtained using non-fully optimized model parameters making *in situ* SE a fast and reliable technique for determination of the ALD saturation curves.

C. Initial film growth

The initial growth of the ALD films has to be addressed to investigate the film nucleation behavior on various kinds of substrate materials. In general, it is observed that the nucleation can drastically be inhibited or accelerated during the first ALD cycles. Since the film nucleation is determined by the chemical reactivity of the volatile ALD precursors to the available adsorption sites on the substrate, it can strongly depend on the combination of the ALD process and the substrate material employed. In particular for the ultrathin films targeted by ALD, insight into the initial film growth is essential to estimate the actual film thickness after a certain amount of ALD cycles.

The film nucleation is often studied by sensitive (*ex situ*) diagnostics, such as x-ray photoelectron spectroscopy (XPS), Rutherford backscattering spectroscopy (RBS), and low energy ion scattering (LEIS). These techniques provide detailed insights into film thickness and film closure, but also on the kind of chemical bonding of the ALD film to the substrate [49–52]. In this section, it will be demonstrated that the nucleation behavior of the ALD film can also be studied by *in situ* SE by acquiring data after every ALD cycle. Similar to the approach in the previous section, the SE model parameters were kept constant and only the film thickness was fitted for the different cycles. In this respect, it is noted that the trend in initial film thickness was found to be virtually independent of the model

parameters employed, although the thickness values can (slightly) vary when adjusting the model parameters. The combination of *in situ* SE and ALD is, therefore, an excellent means to monitor the film nucleation on various substrate materials.

The nucleation behavior as a function of ALD cycles on various substrates (Al_2O_3 on Si, Ge, and GaAs substrates) and for several materials (TiN on SiO_2 and $\text{TaN}_{x,x\leq 1}$ on Si) is shown in Fig. 5.5. The native oxides of the Si, Ge, and GaAs substrates were removed by a wet etch in a 2% buffered HF solution (HF-last). The thermal SiO_2 substrate was prepared by the method of calcination [15], that resulted in a surface consisting of siloxane bridges with a small amount of surface hydroxyls ($0\text{--}0.5\text{ nm}^{-2}$ [53]). Figure 5.5(a) shows that the Al_2O_3 films nucleated immediately and the growth rate became constant at $0.10\pm 0.01\text{ nm/cycle}$ independent of the substrate material. This growth behavior corresponds to results reported in the literature where immediate growth of Al_2O_3 was reported on various substrates, such as H-terminated Si [54], polyethylene terephthalate (PET) polymer [55], and wool [56]. On careful examination of Fig. 5.5(a), a slight accelerated Al_2O_3 growth is observed for the first 4 cycles, but this can probably be attributed to some (additional) oxide layer formation by the O_2 plasma exposure during the process. The formation of such an interfacial oxide layer was also observed by Ha *et al.* [54]. Since the interfacial layer can not be distinguished optically from the Al_2O_3 film due to the minimal optical contrast, the plotted Al_2O_3 thickness, in fact, represents the sum of both layers and that accounts for the accelerated growth observed.

Figure 5.5(b) shows the nucleation behavior of the plasma-assisted ALD process of TiN and TaN films. The ALD growth of TaN_x from $\text{Ta}[\text{N}(\text{CH}_3)_2]_5$ and an H_2 plasma on an H-terminated Si substrate does not show any growth incubation and the growth is linear with ALD cycles from the start. From this observation it is concluded that this metal-organic precursor readily reacts with the surface groups of the H-terminated Si substrate, since no interfacial layer formation by the H_2 plasma is expected for this Si substrate. A completely different nucleation behavior is observed for ALD of TiN from TiCl_4 and a $\text{H}_2\text{--N}_2$ plasma on a thermally grown SiO_2 surface. A distinct incubation period is observed and the growth starts only after ~ 20 ALD cycles. The film thickness becomes linear with the number of cycles only after ~ 50 cycles. This behavior is consistent with the inability of the TiCl_4 precursor to react with the siloxane bridges mainly present on the thermal SiO_2 substrate. The slow nucleation is

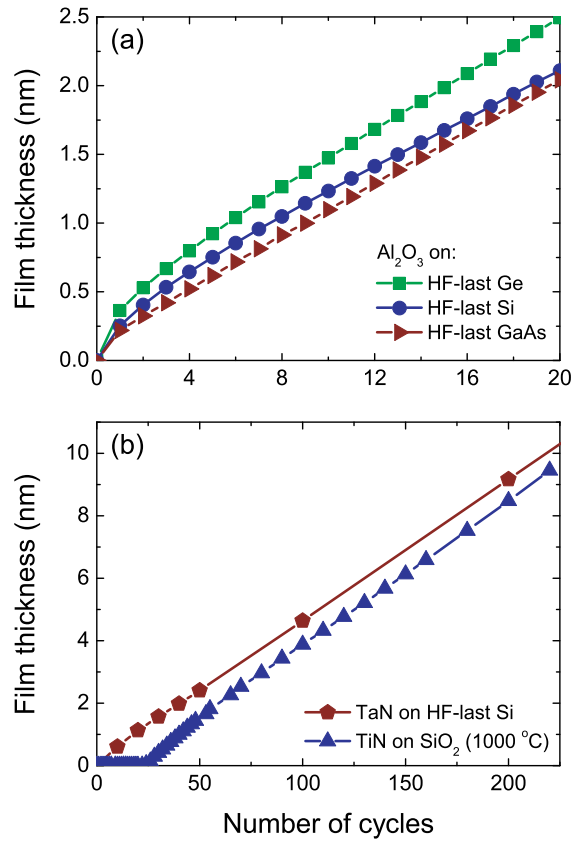


Figure 5.5: The film thickness as a function of number of ALD cycles as determined from cycle-by-cycle data. (a) ALD growth of Al_2O_3 films on GaAs, Ge, and Si substrates treated by a HF wet etch prior to deposition. (b) ALD growth of TiN and TaN films. The TiN film was deposited on a Si substrate covered by SiO_2 prepared by thermal oxidation at 1000 °C and the TaN was deposited on a Si substrate treated by a HF wet etch prior to deposition. The typical uncertainty in the film thickness is 0.3 nm.

caused by the limited surface density of defect sites and OH groups on which the TiCl_4 can nucleate to start film growth [15]. For other experiments on thermal SiO_2 wafers, the TiN nucleation behavior as deduced from SE measurements was found to be in good agreement with the growth curve as determined by *ex situ* XPS and RBS analysis on films deposited with 5, 20, 40, and 80 cycles. The TiN film nucleation on H-terminated Si substrates was also monitored by *in situ* SE [15]. In that case, SE revealed that first an interfacial SiN_x layer was formed due to the $\text{H}_2\text{-N}_2$ plasma exposure used in the ALD process, as also supported by additional XPS and RBS analysis. In line with the fact that the metal-halide TiCl_4 precursor does not react with the silicon-hydrides surface groups [57], it was observed that the TiN film nucleated on the ($-\text{NH}_x$) surface groups of the SiN_x layer rather than on the silicon-hydrides surface groups of the starting substrate.

D. ALD half-cycle reactions

The sub-monolayer sensitivity of SE can be used to probe the repetitive changes of surface groups during the ALD cycle. This can be demonstrated for the plasma-assisted ALD processes of Al_2O_3 and Er_2O_3 using the $\text{Al}(\text{CH}_3)_3$ and $\text{Er}(\text{thd})_3$ precursors, respectively, in combination with an O_2 plasma (cf. Table 5.1). For this purpose, a ~ 18 nm thick Er_2O_3 – Al_2O_3 nanolaminate film was deposited by continuously alternating 5 ALD cycles of Er_2O_3 (corresponding to ~ 1 Å thickness) with 3 ALD cycles of Al_2O_3 (corresponding to ~ 3 Å thickness). The film growth was monitored by acquiring SE data in between the self-limiting ALD half-reactions, i.e., after the precursor dosing and after the O_2 plasma exposure. Some results obtained during several cycles of Er_2O_3 and Al_2O_3 ALD are shown in Fig. 5.6.

Addressing first the results for Al_2O_3 , Fig. 5.6(a) and (b) show the ellipsometric parameters Ψ and Δ during 3 cycles of Al_2O_3 (i.e., 424–426 cycles), where half-integers and full-integers represent data acquired after the precursor dosing and plasma exposure, respectively. The saw tooth-like features observed in these parameters indicate a repetitive growth behavior in each cycle, which is in line with the expected repetitive change of surface groups within the ALD cycles. The overall increase (decrease) in Ψ (Δ) with the number of full ALD cycles is, in turn, an indication of ALD film growth in which the thickness increases step-by-step. It is obvious that the change in Ψ and Δ per cycle depends on the photon energy probed (i.e., $E = 3.0$ eV in Fig. 5.6).

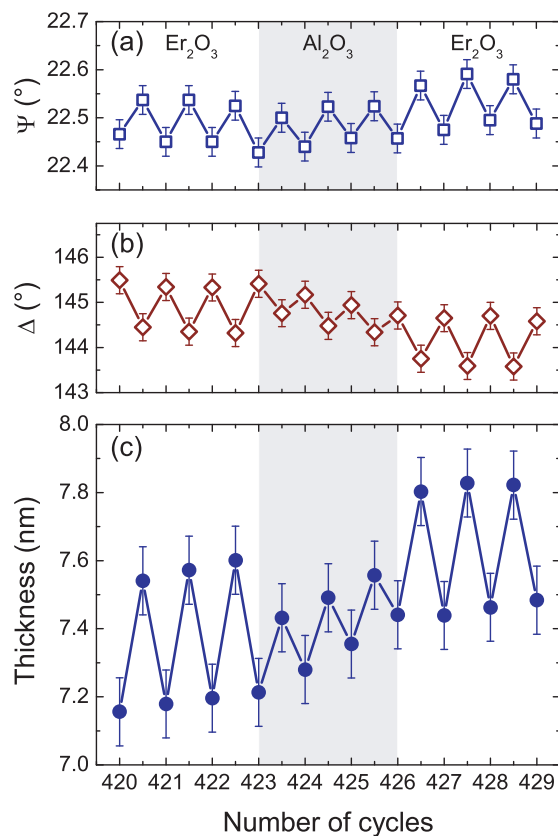


Figure 5.6: Half-cycles monitored during ALD of Er₂O₃ and Al₂O₃. The half-integer and full-integer data points represent measurements after the precursor dosing (Er(thd)₃ for Er₂O₃ and Al(CH₃)₃ for Al₂O₃) and after the O₂ plasma step, respectively. (a) The change in the amplitude ratio Ψ and (b) the phase angle Δ depicted for a photon energy of 3.0 eV as a function of number of ALD cycles. (c) Change in the “apparent” thickness of the Er₂O₃–Al₂O₃ nanolaminate film with the number of ALD cycles as calculated from a Cauchy model.

In order to better understand the effect of ALD half-cycles on the ellipsometric parameters, the *apparent* film thickness [Fig. 5.6(c)] is calculated by using a Cauchy parametrization to describe the dielectric function of the $\text{Er}_2\text{O}_3\text{-Al}_2\text{O}_3$ nanolaminate film. Strictly speaking the dielectric function of the surface layers present after precursor and plasma half-cycles are expected to differ from the bulk dielectric function. However, no separate surface layer is added to the model, because such a layer can not easily be distinguished unambiguously from the bulk due to the minimal thickness of the surface layer. The changes in apparent thickness after the precursor and O_2 plasma steps are therefore a combination of a physical change in film thickness and a change of optical properties of the surface layer. Consequently, the magnitude of the changes in apparent thickness in Fig. 5.6(c) are only an approximation of the real changes in physical thickness. After the precursor half-cycle (i.e., cycles 423.5, 424.5, and 425.5 in Fig. 5.6), the $\sim 2 \text{ \AA}$ increase in apparent thickness can be related to the chemisorption of the $\text{Al}(\text{CH}_3)_3$ precursor on the $-\text{OH}$ surface groups present (as established in Ref. [9]). After the O_2 plasma step (i.e., cycles 424, 425, and 426 in Fig. 5.6), the $-\text{CH}_3$ surface groups are removed resulting in $\sim 1 \text{ \AA}$ decrease in apparent thickness. At this point the surface is again terminated with $-\text{OH}$ groups similar to the start of the ALD cycle, albeit with an additional submonolayer of Al_2O_3 deposited in the cycle. The decrease in apparent thickness after the O_2 plasma step can most probably be attributed for a large part to the exchange of the smaller $-\text{OH}$ surface groups with larger $-\text{CH}_3$ surface groups. The increase in thickness per full ALD cycle, i.e., $0.010 \pm 0.01 \text{ nm/cycle}$, corresponds well to the growth rate reported in our previous work [7–9].

Because the changes in apparent thickness are a combination of a physical change in film thickness and a change of optical properties of the surface layer, the change in *physical* thickness per half-cycle is probably even larger than the change in apparent thickness for the case of ALD of Al_2O_3 . The refractive index of the layer of $-\text{CH}_3$ surface groups is probably smaller than the refractive index of the layer of $-\text{OH}$ surface groups as can be deduced from an experiment in chemical synthesis: the refractive index of an alcohol decreased after exchanging the $-\text{OH}$ end group with a $-\text{CH}_3$ end group forming an alkane [58].

The sensitivity of SE to probe changes in surface groups during the ALD half-cycles can be further illustrated by examining the change in the ellipsometric parameters and apparent thickness during the Er_2O_3 ALD process (i.e., 420–423 cycles and 427–429 cycles in Fig. 5.6). Fig-

ure 5.6 shows that the changes in Ψ , Δ , and apparent thickness during ALD of Er_2O_3 are much larger compared to the changes in these parameters during ALD of Al_2O_3 . With the notion that the thd-ligands [i.e., $-\text{OCC}(\text{CH}_3)_3\text{CHCOC}(\text{CH}_3)_3$] of the $\text{Er}(\text{thd})_3$ precursor are much larger than the $-\text{CH}_3$ ligands of the $\text{Al}(\text{CH}_3)_3$ precursor, the magnitude of the changes in Ψ , Δ , and apparent thickness can obviously be related to the size of the adsorbed ligands. The latter is even more apparent when realizing that the number of Er atoms that adsorb per cycle, as expressed by the growth rate of $0.018 \pm 0.004 \text{ nm/cycle}$, is far lower than the number of Al atoms deposited per cycle. This implies that the optical response caused by the *smaller* amount of *larger* ligands at the surface during ALD of Er_2O_3 exceeds the optical response caused by the *larger* amount of *smaller* $-\text{CH}_3$ ligands at the surface during ALD of Al_2O_3 .

In line with these results, the combination between ALD and *in situ* SE might open up a new route to determine the dielectric function of surface layers of chemical species (e.g., the Al–OH or Al– CH_3 surface layers relevant to ALD of Al_2O_3). Using the method of direct inversion, the thickness and dielectric function of the surface layer can in principle be deduced from the half-cycle SE data. Furthermore, since the same surface layer will be present after another full ALD cycle, the dielectric function of the surface layer can be “averaged” over multiple ALD cycles and total film thickness values to improve the accuracy of the dielectric function obtained.

E. Electron-impurity scattering in ALD films

Insight into the electrical properties of conductive films can be derived from the dielectric function by adopting the Drude parameterization (Sec. III). Therefore, monitoring the ALD film growth by *in situ* SE provides the opportunity to investigate the influence of ALD process conditions, such as deposition temperature and plasma exposure time, on the electrical film properties obtained. This can be demonstrated for the ALD process of TiN films, where the dielectric function can be parametrized by a Drude-Lorentz oscillator model as described in Sec. III. To investigate the influence of deposition temperature on the electrical resistivity, the electron mean free path, and the conduction electron density, TiN films were deposited by plasma-assisted ALD at substrate temperatures between 100 and 400 °C [15].

The electrical resistivity was calculated from the *in situ* SE data using Eq. 5.9. In order to make a correct comparison with the resistivity

determined by *ex situ* four-point probe (FPP) measurements carried out at room temperature, the *in situ* SE resistivity values obtained at the deposition temperature were corrected for temperature-dependent electron-phonon scattering. Therefore, the change in TiN dielectric function with substrate temperature was also monitored by *in situ* SE to determine the intrinsic temperature coefficient of resistivity [15]. Using this coefficient, the resistivity values obtained at deposition temperature were recalculated to values representing room temperature resistivity values.

Figure 5.7(a) shows the room temperature values of the electrical resistivity of TiN as a function of the deposition temperature for the plasma-assisted ALD process. The resistivity values obtained by *in situ* SE and *ex situ* FPP were in good agreement, especially for films deposited at substrate temperatures above 200 °C. Both techniques show that the resistivity of the TiN films increases for depositions at lower temperatures. This effect can be related to the increase in chlorine impurity content of the films, as was determined by Rutherford backscattering spectroscopy (RBS) and shown in the inset of Fig. 5.7(a). In addition, the discrepancy between the resistivity values determined by *in situ* SE and *ex situ* FPP at low temperatures can also be related to the impurity content. The higher impurity content and the related lower film density can make the films more susceptible to post-deposition oxidation when the films are exposed to air. This directly affects the *ex situ* measurements.

The trend in the resistivity observed in Fig. 5.7(a) can further be understood by considering the fact that the electrical resistivity depends both on the electron MFP and the electron density. These parameters can also be calculated from the *in situ* SE data (i.e., Eqs. 5.7 and 5.8). Figure 5.7(b) shows that the electron MFP decreases with decreasing deposition temperature, while the conduction electron density remains virtually constant. The observed increase in resistivity for lower deposition temperature in Fig. 5.7(a) can therefore be attributed to the decrease in electron MFP. Since the grain size (typically >6 nm as measured for a 45 nm thick TiN film by x-ray diffraction) is expected to be larger than the electron MFP for the thin TiN films [15], it can be concluded that scattering of electrons on the chlorine impurities is the main cause for the increase in resistivity at lower deposition temperatures. These results demonstrate that *in situ* SE provides an accurate means to investigate electrical properties of conductive films and their dependence on the deposition conditions.

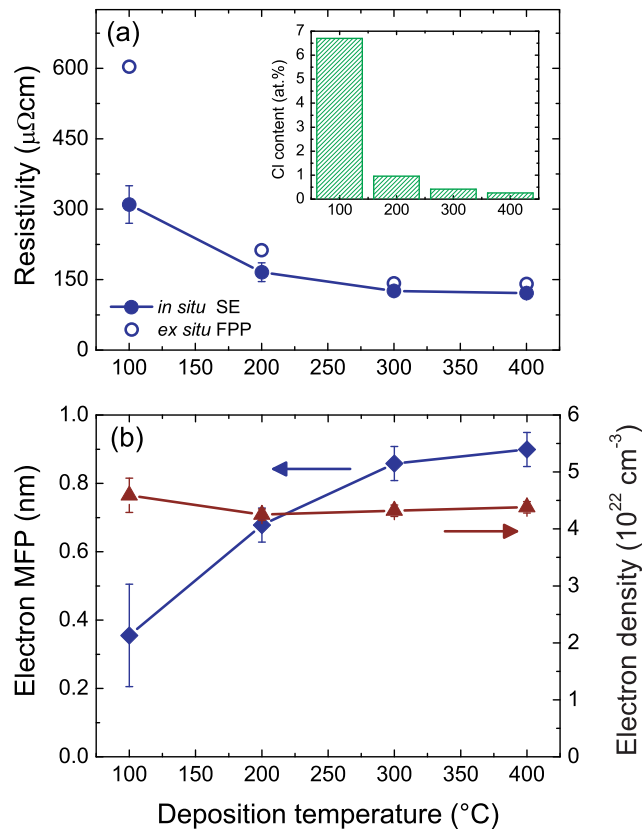


Figure 5.7: (a) The electrical resistivity, (b) the electron mean free path (MFP), and the electron density of ALD TiN films as a function of the deposition temperature. The data have been extracted from the *in situ* SE measurements. The resistivity is compared to the values obtained by *ex situ* four-point probe (FPP) measurements. The chlorine content of the films as determined by Rutherford backscattering spectroscopy is shown in the inset.

F. Size effects in conductive ALD films

Another aspect relevant for the application of ultrathin ALD films is the change of material properties with the film thickness, so-called (finite) size effects [59, 60]. Rather than fitting only the thickness for the data acquired at different ALD cycles, the influence of film thickness on the electrical properties of a TiN film was studied by optimizing all fit parameters of the Drude-Lorentz oscillator model for various film thicknesses (2–65 nm). The electrical properties deduced were corrected to values representing room temperature, similar to the procedure described in the previous section.

The electrical resistivity, the electron density, and the electron MFP are shown in Fig. 5.8 as a function of the thickness of the TiN film. The electrical resistivity of the TiN film in Fig. 5.8(a) increases monotonously with decreasing film thickness. This increase in the resistivity can largely be attributed to the decrease in the electron MFP, while the electron density remains almost constant down to a film thickness of 5 nm [Fig. 5.8(b)].

In order to obtain insight into the scaling behavior of the resistivity with the film thickness, the excess resistivity $\rho_s = \rho - \rho_0$ was calculated by subtraction of the bulk resistivity of the TiN film [$\rho_0 = 68 \mu\Omega \text{ cm}$ as estimated from Fig. 5.8(a)]. As shown in the inset of Fig. 5.8(a), the excess resistivity follows a power law $\rho_s \propto d^{-a}$ with film thickness d . The best fit to the data results in a coefficient $a = 1.1 \pm 0.1$, which indicates that the excess resistivity is inversely proportional to the film thickness. This scaling behavior is reported in several theoretical models, such as the grain boundary scattering model proposed by Mayadas and Shatzkes [61], the model on surface scattering of conduction electrons based on the work of Fuchs and Sondheimer [59, 62], and the combination of these two models as more recently proposed by Steinhögl *et al.* [60, 63]. From the scaling behavior, it is concluded that quantum size effects (with a scaling coefficient $a = 2$ as reported in Ref. [64]) do not play a role yet for the thickness range examined. The size effects observed in Fig. 5.8 can, therefore, be the result of several electron scattering effects. Due to the reduced dimensions of the film, a more pronounced contribution of electron-sidewall scattering is effectively decreasing the electron MFP in ultrathin films. In addition, it was reported that the amount of chlorine impurities in the TiN film was relatively higher for thinner films because of the higher chlorine concentration at the buried interface and the top surface of the film [14]. This increase in chlorine impurities results in an increased contribution from electron-impurity scattering in the film, which is also reducing the electron MFP.

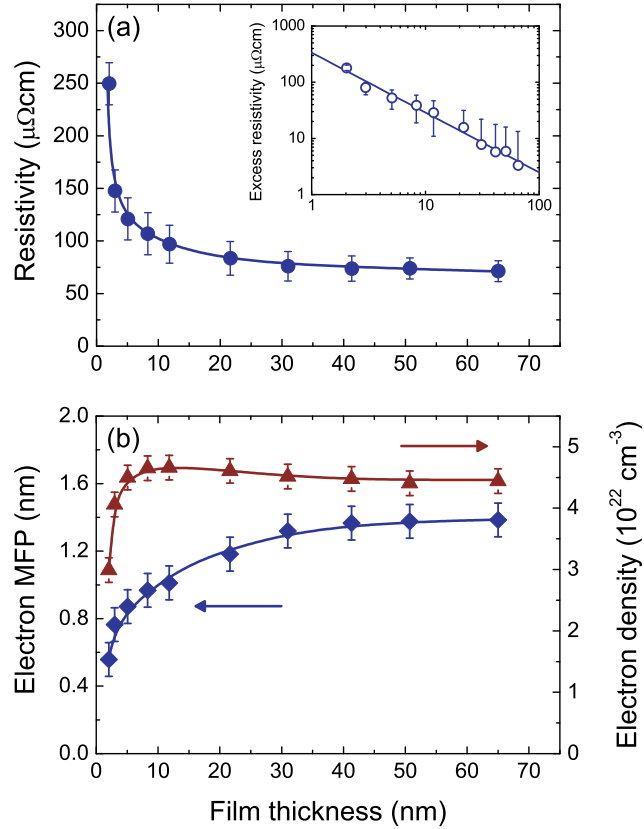


Figure 5.8: (a) The electrical resistivity, (b) the electron mean free path (MFP), and the electron density of an ALD TiN film as a function of the film thickness. The data have been extracted from *in situ* SE measurements. The excess resistivity $\rho_s = \rho - \rho_0$, i.e., the resistivity after subtraction of the bulk resistivity $\rho_0 = 68\ \mu\Omega\text{cm}$, as a function of the thickness is shown in the inset. The line in the inset is a linear regression to the data; the other lines serve as guides to the eye.

Overall, it is evident that size effects can be investigated by acquiring *in situ* SE data during the ALD film growth. In particular for highly conductive metal films (i.e., a high mass density and a large electron MFP resulting in a pronounced Drude absorption), it is expected that the combination of the layer-by-layer ALD growth and the sensitivity of *in situ* SE can provide an excellent means to elucidate the role of the thickness on the electrical properties in ultrathin metal films.

G. Distinction of TaN_x phases

Tantalum nitride (TaN_x) can exist in different crystalline phases and in our earlier work, it was shown that the TaN_x phase and film properties can be tailored by the plasma step in the remote plasma ALD process [16]. Conductive, cubic TaN_x films can be deposited when using a H_2 plasma and the plasma exposure time in the ALD cycle can be used to tune the electrical resistivity. Admixing N_2 to the H_2 plasma or using a NH_3 plasma results in the deposition of N-rich TaN_x or Ta_3N_5 films. In this section, the dielectric functions of these different TaN_x films are compared and it will be shown that the different TaN_x phases can be distinguished by SE.

Figure 5.9 shows the imaginary part (ε_2) of the dielectric functions of the TaN_x films that were deposited using different plasma conditions in the ALD cycle. The dielectric functions are extracted from the SE data by point-to-point direct inversion using the thickness values obtained by fitting the data first with a model in which the optical dispersion was parameterized. As already discussed in Sec. III, the conductive films can be described adequately by the Drude-Lorentz oscillator model. The figure clearly shows that the $\text{TaN}_{0.45}$ film deposited with the 30 s H_2 plasma exposure time has a stronger Drude absorption than the $\text{TaN}_{0.49}$ film deposited with 10 s H_2 plasma exposure time. This translates into a lower electrical resistivity of the $\text{TaN}_{0.45}$ film ($\sim 3.9 \times 10^2 \mu\Omega \text{ cm}$) compared to the $\text{TaN}_{0.49}$ film ($\sim 1.2 \times 10^3 \mu\Omega \text{ cm}$), as corroborated by four-point probe measurements. Admixing little N_2 (2%) to the H_2 plasma, strongly reduces the magnitude of the Drude absorption in the film and the two Lorentz oscillators become clearly visible. The resulting $\text{TaN}_{1.0}$ film is still somewhat conducting ($\sim 1.1 \times 10^4 \mu\Omega \text{ cm}$). On the other hand, the dielectric function of the $\text{Ta}_3\text{N}_{4.7}$ film deposited using a $\text{H}_2\text{-N}_2$ (1:1) plasma clearly differs in shape and is best described by the Tauc-Lorentz oscillator model. For this film, an additional Lorentz oscillator is added to the parameterization to account for the small absorption below the band gap. The dielectric function of the Ta_3N_5 film deposited using a NH_3 plasma clearly shows an

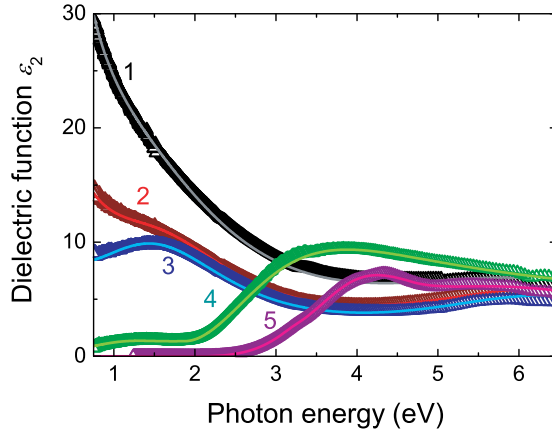


Figure 5.9: The imaginary part of the dielectric function ε_2 (open symbols) of several TaN_x films as obtained from direct inversion of the ellipsometric data. The films were deposited under various plasma conditions in the ALD cycle and were described by different parametrizations (solid lines) as indicated in between parentheses: 1) 30 s H_2 plasma [Drude-Lorentz, $x = 0.44$], 2) 10 s H_2 plasma [Drude-Lorentz, $x = 0.49$], 3) 5 s $\text{H}_2\text{-N}_2$ (98:2) plasma [Drude-Lorentz, $x = 1.0$], 4) 10 s $\text{H}_2\text{-N}_2$ (1:1) plasma [Tauc-Lorentz with an additional Lorentz oscillator, $x = 1.55$], and 5) 10 s NH_3 plasma [Tauc-Lorentz, $x = 1.67$]. The ratio $x = [\text{N}]/[\text{Ta}]$ of the TaN_x films was determined from Rutherford backscattering spectroscopy measurements on the films.

optical band gap and is best described by a Tauc-Lorentz model composed of three oscillators. The optical band gap for the Ta_3N_5 film is calculated from the dielectric function ε_2 yielding a value of 2.45 ± 0.02 eV. This band gap is within the range of 2.1–2.5 eV reported by Coyne and Tauber [65], while it is slightly higher than the more recent value of 2.08 eV reported by Fang *et al.* [66] and Henderson *et al.* [67]. It has also been reported that oxygen impurities present in the films result in an increase in band gap [66, 67], which could suggest that the Ta_3N_5 film might contain a non-negligible level of oxygen impurities. From the above, it is evident that by monitoring the dielectric functions by *in situ* SE, the change in film composition and crystalline phase can already be probed during the ALD process when the film is still being deposited.

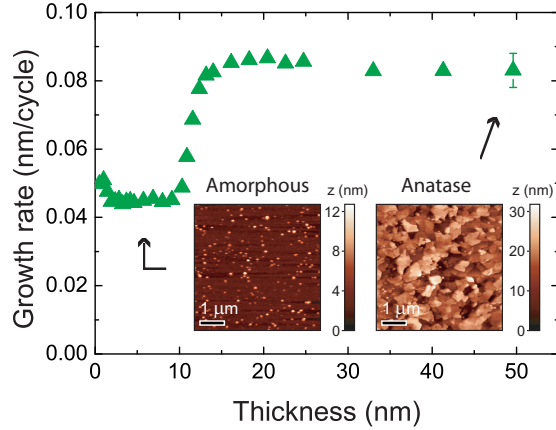


Figure 5.10: The growth rate as a function of the film thickness during plasma-assisted ALD of TiO_2 at 300°C . The AFM micrographs show the typical surface morphology of amorphous and anatase TiO_2 films (note the difference in roughness scale). The typical uncertainty in the growth rate is indicated for the 50 nm thick film.

H. Amorphous-crystalline phase transition during ALD of TiO_2

In the (plasma-assisted) ALD process of TiO_2 films, the crystalline phase of the TiO_2 film can be controlled by the deposition temperature; at low temperatures ($<200^\circ\text{C}$) the TiO_2 is generally amorphous, while at higher temperatures also anatase TiO_2 can be obtained. However, besides the temperature also the film thickness is of influence in this respect [12, 68] as will be shown by *in situ* SE for a TiO_2 film deposited at a substrate temperature of 300°C .

The thickness of an amorphous or anatase TiO_2 film can be determined by using a Cauchy model to describe the transparent part of the dielectric function ($<3.3\text{ eV}$). Subsequently, the growth rate at a certain film thickness can be determined by dividing the increase in film thickness over the amount of cycles carried out between the two *in situ* SE measurements. Figure 5.10 shows the growth rate for a TiO_2 film synthesized by plasma-assisted ALD at 300°C as a function of the film thickness. As is clear from this figure, the growth rate remains constant ($0.045 \pm 0.002\text{ nm/cycle}$) up to a film thickness of $\sim 10\text{ nm}$. At that point in thickness, a transition occurs after which the growth rate stabilizes at $0.084 \pm 0.004\text{ nm/cycle}$. Combined to the results obtained by with x-ray diffraction (XRD), atomic force mi-

croscopy (AFM), and transmission electron microscopy (TEM), it can be concluded that the transition indicates a change in TiO₂ microstructure. During the first ~ 10 nm of growth, an amorphous and smooth TiO₂ film (root mean square roughness < 1 nm, inset of Fig. 5.10) is deposited while the film finally ends up anatase with a rough faceted surface (root mean square roughness > 5 nm, inset of Fig. 5.10) [12].

The transition in growth rate was found by analyzing only the transparent part of the dielectric function of the amorphous and anatase TiO₂. Extracting the dielectric function of the anatase TiO₂ over the full photon energy range is not very straightforward from the current data set. The reason is that a rather thick surface roughness layer has to be taken into account while insufficient information on the optical thickness and the dielectric function of the surface roughness layer is available or can be extracted from the SE data acquired. From the data and some optical modeling it can, however, be concluded that the optical band gap of anatase TiO₂ was slightly higher than the band gap of amorphous TiO₂ as expected. Furthermore, it is evident that the transition from amorphous to anatase TiO₂ during the ALD process can almost instantly be detected by *in situ* SE.

V Conclusions

The use of *in situ* spectroscopic ellipsometry (SE) during a variety of atomic layer deposition (ALD) processes was exemplified in this work, clearly demonstrating the merits of the combination of *in situ* SE and ALD. *In situ* SE yields accurate information on the film thickness and the growth rate per cycle and it was shown that this information can be used to determine ALD saturation curves, to study initial film growth (nucleation effects), and even to probe half-cycles with a submonolayer sensitivity with respect to the surface chemical species. These aspects are all very relevant for ALD film growth, both in terms of fundamental understanding and in terms of process optimization and control. Additionally, it was shown that *in situ* SE yields also important information on the material properties *during* the ALD process when the film is still being deposited. Besides the optical properties such as the refractive index and the optical band gap, also insight into the electrical properties of conductive (metal nitride) films can be obtained non-intrusively. The latter aspect can be used to study the influence of film thickness and ALD growth condition (e.g., the setting of precursor/reactant dosing, deposition temperature, etc) on the

electrical properties of the films. Furthermore, the crystalline phase of the thin film materials can be established from the *in situ* SE measurements and phase transitions can even be probed during the ALD growth process.

As is generally valid for ellipsometry measurements, the validity and the accuracy of the information extracted from the measurements depends critically on the interpretation of the data in terms of optical modeling. Corroboration of the results by other (*ex situ*) techniques is therefore key, especially when addressing absolute values of physical quantities. The situation is mitigated when mainly addressing specific trends in the data such that *in situ* SE is particularly useful during ALD film growth for process monitoring and control. The value of SE in monitoring the film growth has recently been recognized by ALD tool manufacturers and has led to the development of commercial ALD reactors with integrated *in situ* spectroscopic ellipsometry capability. It is, therefore, anticipated that *in situ* SE has a bright application prospect in the field of ALD.

Finally we want to note that *in situ* SE cannot only be used to study, optimize and design ALD processes. The combination of *in situ* SE and ALD is also very powerful for fundamental studies of physical and chemical effects related to ultrathin films. The precise growth control and the relatively high level of understanding of the surface chemistry associated with ALD can, e.g., be exploited in studies of the optical properties of surface layers of chemical species or in studies of (quantum) size effects in ultrathin semiconductor and metal films.

VI Experimental

The *in situ* SE measurements described in this paper were carried out by J.A. Woollam, Inc., M2000 rotating compensator ellipsometers [69]. Rotating compensator ellipsometers, with the configuration “light source – polarizer – rotating compensator – sample – analyzer – spectrograph – detector” [cf. Fig. 5.1(a)], combine accurate and fast determination of the ellipsometry data over the complete range of ellipsometric angles ($\Psi = 0 - 90^\circ$, $\Delta = 0 - 360^\circ$). Two ellipsometers, with each a different photon energy range, were employed. The M2000U visible and near-infrared extended (0.75–5.0 eV) ellipsometer was proven particularly powerful to study metallic films due to the Drude absorption by conduction electrons. The M2000D visible and ultra-violet extended (1.2–6.5 eV) ellipsometer was particularly suited to study (high) band gap materials. To obtain a high signal-to-noise ratio, the SE data were typically averaged over 200 to 400 measurements

(leading to a measurement time of 25 s and 45 s) for the M2000U and M2000D ellipsometers, respectively. The acquisition and analysis of the ellipsometry data including optical modeling were carried out using the WVASE32 software from J.A. Woollam, Inc. [69]. In this software, the option was used to combine data obtained on different ellipsometers (e.g., *in situ* data with *ex situ* data obtained at the final film thickness) in order to evaluate the dielectric function of the ALD films over the total photon energy range available by the two ellipsometer systems (i.e., 0.75–6.5 eV as used for Fig. 5.2).

The ALD films (cf. Table 5.1) were deposited in a home-built plasma-assisted ALD reactor [14, 15] and on the FlexALTM ALD reactor of Oxford Instruments [11, 70]. The FlexALTM ALD reactor equipped with *in situ* SE is shown in Fig. 5.1(b). The angle of incidence defined by the optical view ports was fixed to 68 degrees with respect to the normal of the substrate, close to the Brewster angle of $\sim 75^\circ$ for the silicon-based substrates typically used. The beam path from light source to detector is approximately ~ 1 m and the beam spot size on the substrate was ~ 5 mm in diameter.

Acknowledgments

Part of the work was carried out in collaboration with J. L. van Hemmen and M. Bouman (Eindhoven University of Technology) and C. J. Hodson (Oxford Instruments Plasma Technology, United Kingdom). Dr. T. Wagner (L.O.T. Oriel, Germany) is kindly acknowledged for the product support on the ellipsometry systems. M. J. F. van de Sande, J. F. C. Jansen, and J. J. A. Zeebregts are thanked for their skillful technical assistance. This research is financially supported by the Dutch Technology Foundation STW. The research of one of the authors (W.M.M.K.) was made possible by a fellowship from the Royal Netherlands Academy of Arts and Sciences (KNAW).

Bibliography

- [1] International Technology Roadmap for Semiconductors, 2007 (<http://public.itrs.net>).
- [2] M. Leskelä and M. Ritala, *Thin Solid Films* **409**, 138 (2002).
- [3] R. L. Puurunen, *J. Appl. Phys.* **97**, 121301 (2005).
- [4] T. Suntola, *Mater. Sci. Rep.* **4**, 261 (1989).
- [5] S. M. George, A. W. Ott, and J. W. Klaus, *J. Phys. Chem.* **100**, 13121 (1996).
- [6] M. Ritala and M. Leskelä, *Handbook of Thin Film Materials*, volume 1, Academic, San Diego, CA (2001).
- [7] J. L. van Hemmen, S. B. S. Heil, J. H. Klootwijk, F. Roozeboom, C. J. Hodson, M. C. M. van de Sanden, and W. M. M. Kessels, *J. Electrochem. Soc.* **154**, G165 (2007).
- [8] E. Langereis, M. Creatore, S. B. S. Heil, M. C. M. van de Sanden, and W. M. M. Kessels, *Appl. Phys. Lett.* **89**, 081915 (2006).
- [9] E. Langereis, J. Keijmel, M. C. M. van de Sanden, and W. M. M. Kessels, *Appl. Phys. Lett.* **92**, 231904 (2008).
- [10] S. B. S. Heil, P. Kudlacek, E. Langereis, R. Engeln, M. C. M. van de Sanden, and W. M. M. Kessels, *Appl. Phys. Lett.* **89**, 131505 (2006).
- [11] S. B. S. Heil, J. L. van Hemmen, C. J. Hodson, N. Singh, J. H. Klootwijk, F. Roozeboom, M. C. M. van de Sanden, and W. M. M. Kessels, *J. Vac. Sci. Technol. A* **25**, 1357 (2007).
- [12] W. Keuning, J. L. van Hemmen, O. Muraza, E. Rebrov, M. C. M. van de Sanden, and W. M. M. Kessels, *in preparation for publication*.
- [13] S. B. S. Heil, F. Roozeboom, M. C. M. van de Sanden, and W. M. M. Kessels, *J. Vac. Sci. Technol. A* **26**, 472 (2008).
- [14] S. B. S. Heil, E. Langereis, F. Roozeboom, M. C. M. van de Sanden, and W. M. M. Kessels, *J. Electrochem. Soc.* **153**, G956 (2006).
- [15] E. Langereis, S. B. S. Heil, M. C. M. van de Sanden, and W. M. M. Kessels, *J. Appl. Phys.* **100**, 023534 (2006).

- [16] E. Langereis, H. C. M. Knoop, A. J. M. Mackus, F. Roozeboom, M. C. M. van de Sanden, and W. M. M. Kessels, *J. Appl. Phys.* **102**, 083517 (2007).
- [17] H. G. Tompkins and E. A. Irene, *Handbook of Ellipsometry*, William Andrews, Inc., New York (2005).
- [18] H. Fujiwara, *Spectroscopic Ellipsometry: Principles and Applications*, John Wiley & Sons, Ltd., West Sussex, England (2007).
- [19] J. A. Woollam, B. Johs, C. M. Herzinger, J. Hilfiker, R. Synowicki, and C. L. Bungay, *Critical Reviews of Optical Science and Technology, Optical Metrology*, volume CR72, SPIE Publishing, Bellingham, WA (1999).
- [20] H. Arwin and D. E. Aspnes, *Thin Solid Films* **113**, 101 (1984).
- [21] H. G. Tompkins and W. A. McGahan, *Spectroscopic Ellipsometry and Reflectometry*, John Wiley & Sons, Inc., New York (1999).
- [22] G. E. Jellison, Jr. and F. A. Modine, *Appl. Phys. Lett.* **69**, 371 (1996).
- [23] E. Langereis, S. B. S. Heil, M. C. M. van de Sanden, and W. M. M. Kessels, *Phys. Stat. Sol. C* **2**, 3958 (2005).
- [24] A. A. Demkov, L. R. C. Fonseca, E. Verret, J. Tomfohr, and O. F. Sankey, *Phys. Rev. B* **71**, 195306 (2005).
- [25] A. A. Lutich, M. B. Danailov, S. Volchek, V. A. Yakovtseva, V. A. Sokol, and S. V. Gaponenko, *Appl. Phys. B* **84**, 327 (2006).
- [26] M. Aguilar-Frutis, M. Garcia, C. Falcony, G. Plesch, and S. Jimenez-Sandoval, *Thin Solid Films* **389**, 200 (2001).
- [27] H. Takeuchi, D. Ha, and T.-J. King, *J. Vac. Sci. Technol. A* **22**, 1337 (2004).
- [28] Y. J. Cho, N. V. Nguyen, C. A. Richter, J. R. Ehrstein, B. H. Lee, and J. C. Lee, *Appl. Phys. Lett.* **80**, 1249 (2002).
- [29] O. Buiu, Y. Lu, I. Z. Mitrovic, S. Hall, P. Chalker, and R. J. Potter, *Thin Solid Films* **515**, 623 (2006).
- [30] J. Tauc, R. Grigorovici, and A. Vancu, *Phys. Stat. Sol. B* **15**, 627 (1966).

- [31] S. Knief and W. von Niessen, *Phys. Rev. B* **59**, 12940 (1999).
- [32] G. E. Jellison, Jr. and F. A. Modine, *Phys. Rev. B* **27**, 7466 (1983).
- [33] M. Losurdo, M. M. Giangregorio, P. Capezzuto, G. Bruno, R. G. Toro, G. Malandrino, I. L. Fragalà, L. Armelao, D. Barreca, E. Tondello, A. A. Suvorova, D. Yang, and E. A. Irene, *Adv. Funct. Mater.* **17**, 3607 (2007).
- [34] M. Losurdo, M. M. Giangregorio, P. Capezzuto, G. Bruno, G. Malandrino, I. L. Fragalà, L. Armelao, D. Barreca, and E. Tondello, *J. Electrochem. Soc.* **155**, G44 (2008).
- [35] N. V. Nguyen, C. A. Richter, Y. J. Cho, G. B. Alers, and L. A. Stirling, *Appl. Phys. Lett.* **77**, 3012 (2000).
- [36] D. Briand, G. Mondin, S. Jenny, P. D. van der Wal, S. Jeanneret, N. F. de Rooij, O. Banakh, and H. Keppner, *Thin Solid Films* **493**, 6 (2005).
- [37] E. P. Burte and N. Rausch, *J. Non-Cryst. Solids* **187**, 425 (1995).
- [38] T. Babeva, E. Atanassova, and J. Koprinarova, *Phys. Stat. Sol. A* **202**, 330 (2005).
- [39] M. Zhang, G. Lin, C. Dong, and L. W. Zhang, *Surf. Coat. Technol.* **201**, 7252 (2007).
- [40] H. Tang, F. Lévy, H. Berger, and P. E. Schmid, *Phys. Rev. B* **52**, 7771 (1995).
- [41] A. Amtout and R. Leonelli, *Phys. Rev. B* **51**, 6842 (1995).
- [42] S. Mo and W. Y. Ching, *Phys. Rev. B* **51**, 13023 (1995).
- [43] N. W. Ashcroft and N. D. Mermin, *Solid State Physics*, Saunders College, Orlando, FL (1976).
- [44] P. Patsalas and S. Logothetidis, *J. Appl. Phys.* **90**, 4725 (2001).
- [45] P. Patsalas and S. Logothetidis, *J. Appl. Phys.* **93**, 989 (2003).
- [46] K. Postava, M. Aoyama, and T. Yamaguchi, *Appl. Surf. Sci.* **175-176**, 270 (2001).

- [47] B. Karlsson, J.-E. Sundgren, and B.-O. Johansson, *Thin Solid Films* **87**, 181 (1982).
- [48] C. Stampfl and A. J. Freeman, *Phys. Rev. B* **71**, 024111 (2005).
- [49] A. Delabie, R. L. Puurunen, B. Brijs, M. Caymax, T. Conard, O. Richard, W. Vandervorst, C. Zhao, M. M. Heyns, M. Meuris, M. M. Viitanen, H. H. Brongersma, M. de Ridder, L. V. Goncharova, E. Garfunkel, T. Gustafsson, and W. Tsai, *J. Appl. Phys.* **97**, 64104 (2005).
- [50] S.-H. Kim, S. S. Oh, H.-M. Kim, D.-H. Kang, K.-B. Kim, W.-M. Li, S. Haukka, and M. Tuominen, *J. Electrochem. Soc.* **151**, C272 (2004).
- [51] R. L. Puurunen, *J. Appl. Phys.* **95**, 4777 (2004).
- [52] A. Satta, J. Schuhmacher, C. M. Whelan, W. Vandervorst, S. H. Brongersma, G. P. Beyer, K. Maex, A. Vantomme, M. M. Viitanen, H. H. Brongersma, and W. F. A. Besling, *J. Appl. Phys.* **92**, 7641 (2002).
- [53] L. T. Zhuravlev, *Colloids Surf. A: Physicochem. Eng. Aspects* **173**, 1 (2000).
- [54] S.-C. Ha, E. Choi, S.-H. Kim, and J. S. Roh, *Thin Solid Films* **476**, 252 (2005).
- [55] M. D. Groner, F. H. Fabreguette, J. W. Elam, and S. M. George, *Chem. Mater.* **16**, 639 (2004).
- [56] A. Niskanen, K. Arstila, M. Ritala, and M. Leskelä, *J. Electrochem. Soc.* **152**, F90 (2005).
- [57] G. C. Abeln, M. C. Hersam, D. S. Thompson, S.-T. Hwang, H. Choi, J. S. Moore, and J. W. Lyding, *J. Vac. Sci. Technol. B* **16**, 3874 (1998).
- [58] D. R. Lide, *Handbook of Chemistry and Physics*, CRC Press, Boca Raton, 85th edition edition (2005).
- [59] E. Sondheimer, *Adv. Phys.* **1**, 1 (1952).
- [60] W. Steinhögl, G. Schindler, G. Steinlesberger, M. Traving, and M. Engelhardt, *J. Appl. Phys.* **97**, 23706 (2005).

- [61] A. F. Mayadas and M. Shatzkes, Phys. Rev. B **1**, 1382 (1970).
- [62] K. Fuchs, Proc. Cambridge Philos. Soc. **34**, 100 (1938).
- [63] W. Steinhögl, G. Schindler, G. Steinlesberger, and M. Engelhardt, Phys. Rev. B **66**, 075414 (2002).
- [64] R. G. P. van der Kraan, J. F. Jongste, H. M. Jaeger, G. C. A. M. Janssen, and S. Radelaar, Phys. Rev. B **44**, 13140 (1991).
- [65] H. J. Coyne and R. N. Tauber, J. Appl. Phys. **39**, 5585 (1968).
- [66] C. M. Fang, E. Orhan, G. A. de Wijs, H. T. Hintzen, R. A. de Groot, R. Marchand, J.-Y. Saillard, and G. de With, J. Mater. Chem. **11**, 1248 (2001).
- [67] S. J. Henderson and A. L. Hector, J. Solid-State Chem. **179**, 3518 (2006).
- [68] D. R. G. Mitchell, G. Triani, D. J. Attard, K. S. Finnie, P. J. Evans, C. J. Barbé, and J. R. Bartlett, Smart. Mater. Structur. **15**, S57 (2006).
- [69] J. A. Woollam Co., Inc., 650 J Street, Suite 39, Lincoln, NE 68508, USA (<http://www.jawoollam.com>).
- [70] Oxford Instruments Plasma Technology, North End, Yatton BS49 4AP, United Kingdom (<http://www.oxford-instruments.com>).

Summary

Plasma-assisted atomic layer deposition an *in situ* diagnostic study

The method of atomic layer deposition (ALD) is considered one of the primary candidates for the uniform and conformal deposition of ultrathin films vital for the continuous miniaturization in the semiconductor industry and related high-technology markets. By the virtue of two self-limiting surface reactions, the ALD technique yields an ultimate control of film growth in the sense that a submonolayer of material is deposited per so-called ALD cycle. With established materials being at the verge of industrial implementation, efforts are continuously undertaken to optimize and develop new ALD configurations and processes. So far, the main emphasis within the field of ALD has been on the materials characterization of the films by means of *ex situ* analysis. The research described in this thesis aims at the development of the relatively new configuration of plasma-assisted ALD and at *in situ* diagnostics studies of the (plasma-assisted) ALD processes.

In plasma-assisted ALD, a plasma is used to activate the reactants in the gas phase in order to supply additional reactivity to the ALD chemistry. Plasma-assisted ALD is researched to provide benefits in the development of new ALD processes and materials. In particular, the opportunities to improve and tune the film properties, and to deposit films at reduced substrate temperatures have been addressed in this thesis. This work has been accompanied by studies using various *in situ* diagnostics, from which fundamental insight into the reaction mechanisms governing the ALD processes can be obtained. Moreover, *in situ* techniques provide the opportunity to monitor, optimize, and control the ALD process. In this work the use of *in situ* spectroscopic ellipsometry, transmission infrared spectroscopy, mass spectrometry, and optical emission spectroscopy has been demonstrated in studies of the plasma-assisted ALD processes of metal nitrides and metal oxides. The results of the film characterization obtained by these techniques have been corroborated and complemented by extensive *ex situ* analysis. In particular, the combination of *in situ* spectroscopic ellipsometry and the layer-by-layer ALD growth has been explored comprehensively. The merits of this *in situ* technique during ALD have been demonstrated by addressing various aspects relevant to ALD processes and materials.

A large part of the work has concentrated on the plasma-assisted ALD process of the metal nitrides TiN and TaN. The merits of plasma-assisted

ALD were observed in the deposition TiN films with excellent conductivity and low impurity content, even at low deposition temperatures. Furthermore, it was shown that by variation of the plasma condition in the ALD process of TaN, the film properties could be tailored from conductive, cubic $\text{TaN}_{x,x \leq 1}$ to semiconductive, amorphous Ta_3N_5 . These aspects were clearly demonstrated by *in situ* spectroscopic ellipsometry, where the transition in TaN_x phase could be distinguished by monitoring the energy dispersion in the optical constants. For the conductive films, the light absorption by free conduction electrons could be probed and that enabled extraction of the electrical film properties from the ellipsometry data. The latter was valuable to demonstrate electron-impurity scattering and finite size effects in TiN films. Furthermore, fundamental insight into the reaction mechanisms of plasma-assisted ALD process of TaN was obtained by detection of the volatile reaction by-products by mass spectrometry and optical emission spectroscopy.

The possibilities for plasma-assisted ALD to improve the material properties and to deposit at reduced temperatures have been demonstrated for the process of Al_2O_3 . The Al_2O_3 films were deposited at substrate temperatures down to room temperature and these films yielded good moisture permeation barrier properties as relevant for encapsulation purposes. The fundamental reaction mechanisms of this plasma-assisted ALD process were elucidated by transmission infrared spectroscopy in order to understand and further improve the film properties obtained at these reduced deposition temperatures. It was established that the surface chemistry is ruled by $-\text{CH}_3$ and $-\text{OH}$ surface groups created by the $\text{Al}(\text{CH}_3)_3$ precursor adsorption and the combustionlike reactions during the O_2 plasma step, respectively. Moreover, infrared spectroscopy provided insight into the influence of deposition temperature on the material properties. It was shown that by prolonging the plasma exposure, i.e., by supplying more plasma reactivity to the ALD process, the surface chemistry at low temperatures was enhanced and the impurity content in the Al_2O_3 was reduced.

In conclusion, the knowledge gained through the *in situ* diagnostic studies in this work is relevant to further develop the ALD technique. The insight obtained into the reaction mechanisms and the material properties of the ALD films in this work are particularly useful to further exploit the possibilities and opportunities of the plasma-assisted ALD technique in the synthesis of novel (complex) materials.

List of publications related to this work

***In situ* spectroscopic ellipsometry as a versatile tool to study atomic layer deposition**

E. Langereis, S. B. S. Heil, H. C. M. Knoops, W. Keuning, M. C. M. van de Sanden, and W. M. M. Kessels, submitted for publication; Chapter 5 of this thesis.

***In situ* infrared characterization during atomic layer deposition of lanthanum oxide**

J. Kwon, M. Dai, E. Langereis, M. D. Halls, Y. J. Chabal, and R. G. Gordon, submitted for publication.

Plasma-assisted ALD of Al₂O₃ at low temperatures: reaction mechanism and material properties

E. Langereis, M. Bouman, J. Keijmel, S. B. S. Heil, M. C. M. van de Sanden, and W. M. M. Kessels, ECS Transactions (2008).

Surface chemistry of plasma-assisted atomic layer deposition of Al₂O₃ studied by infrared spectroscopy

E. Langereis, J. Keijmel, M. C. M. van de Sanden, and W. M. M. Kessels, Appl. Phys. Lett. **92**, 231904 (2008); Chapter 4 of this thesis.

Synthesis and *in situ* characterization of low-resistivity TaN_x films by remote plasma atomic layer deposition

E. Langereis, H. C. M. Knoops, A. J. M. Mackus, F. Roozeboom, M. C. M. van de Sanden, and W. M. M. Kessels, J. Appl. Phys. **102**, 083517 (2007); Chapter 2 of this thesis.

Deposition of TiN and TaN by remote plasma ALD for diffusion barrier applications

H. C. M. Knoops, L. Baggetto, E. Langereis, M. C. M. van de Sanden, J. H. Klootwijk, F. Roozeboom, R. A. H. Niessen, P. H. L. Notten, and W. M. M. Kessels, ECS Transactions **11**, 45 (2007).

Low-temperature deposition of TiN by plasma-assisted atomic layer deposition

S. B. S. Heil, E. Langereis, F. Roozeboom, M. C. M. van de Sanden, and W. M. M. Kessels, J. Electrochem. Soc. **153**, G956 (2006).

Opportunities for plasma-assisted atomic layer deposition

W. M. M. Kessels, S. B. S. Heil, E. Langereis, J. L. van Hemmen, H. C. M. Knoops, W. Keuning, and M. C. M. van de Sanden, ECS Transactions **3**, 183 (2006).

***In situ* reaction mechanism studies of plasma-assisted atomic layer deposition of Al₂O₃**

S. B. S. Heil, P. Kudlacek, E. Langereis, R. Engeln, M. C. M. van de Sanden, and W. M. M. Kessels, Appl. Phys. Lett. **89**, 131505 (2006).

Plasma-assisted atomic layer deposition of Al₂O₃ moisture permeation barriers on polymers

E. Langereis, M. Creatore, S. B. S. Heil, M. C. M. van de Sanden, and W. M. M. Kessels, Appl. Phys. Lett. **89**, 081915 (2006); Chapter 3 of this thesis.

Ultralow surface recombination of *c*-Si substrates passivated by plasma-assisted atomic layer deposited Al₂O₃

B. Hoex, S. B. S. Heil, E. Langereis, M. C. M. van de Sanden, and W. M. M. Kessels, Appl. Phys. Lett. **89**, 042112 (2006).

***In situ* spectroscopic ellipsometry study on the growth of ultrathin TiN films by plasma-assisted atomic layer deposition**

E. Langereis, S. B. S. Heil, M. C. M. van de Sanden, and W. M. M. Kessels, J. Appl. Phys. **100**, 023534 (2006); Chapter 1 of this thesis.

Plasma-assisted atomic layer deposition of Al₂O₃ on polymers

E. Langereis, S. B. S. Heil, M. Creatore, M. C. M. van de Sanden, and W. M. M. Kessels, 49th Annual Technical Conference Proceedings of the Society of Vacuum Coaters, 19 (2006).

Plasma-assisted atomic layer deposition of TiN monitored by *in situ* spectroscopic ellipsometry

S. B. S. Heil, E. Langereis, A. Kemmeren, F. Roozeboom, M. C. M. van de Sanden, and W. M. M. Kessels, J. Vac. Sci. Technol. **23**, L5 (2005).

Initial growth and properties of atomic layer deposited TiN films studied by *in situ* spectroscopic ellipsometry

S. B. S. Heil, E. Langereis, F. Roozeboom, A. Kemmeren, N. P. Pham, P. M. Sarro, M. C. M. van de Sanden, and W. M. M. Kessels, Mater. Res. Soc. Symp. Proc. **863**, B6.4.1 (2005).

Initial growth and properties of atomic layer deposited TiN films studied by *in situ* spectroscopic ellipsometry

E. Langereis, S. B. S. Heil, M. C. M. van de Sanden, and W. M. M. Kessels, Phys. Stat. Sol. C **2**, 3958 (2005).

Acknowledgments

Het werk dat in dit proefschrift beschreven staat is uiteraard niet door mij alleen verricht en is tot stand gekomen door steun van velen. Aangezien het dankwoord van het proefschrift het meest gelezen onderdeel van het proefschrift schijnt te zijn, is de druk om niemand te vergeten enorm.

Allereerst wil ik Erwin en Richard bedanken, die ervoor gezorgd hebben dat ik een schitterende en vooral erg leerzame tijd heb gehad tijdens mijn promotie. Na al in een vroeg stadium ontdekt te zijn door Erwin tijdens het eerstejaars Natuurkunde practicum, heb ik de laatste 4 jaar gemerkt dat Erwin een enorm inspirerende begeleider is. Jouw enthousiasme voor de wetenschap en oog voor detail en structuur zijn van ongekennde waarde. Enorm dank daarvoor en nogmaals mijn excuses voor de noodzakelijke “weekendjes Langereis”. Richard, jouw bliksembezoeken vol goede ideeën en waardevolle suggesties zijn altijd een inspiratie. Bovendien hebben we vaak samen gestreden tegen onrecht op het voetbalveld en naderhand waren we het er altijd over eens dat het zeker niet aan ons lag... Samen met Adriana, Richard, Daan, Jeanne en Lianne hebben jullie een ongekennde groeps sfeer gecreeërd bij PMP. Bedankt daarvoor!

De laatste vier jaar zijn voorbij gevlogen en de uitdaging was dat ALD een nieuwe discipline in de vakgroep was. Samen met Stephan, die in het half jaar voor mijn start de ALD reactor operationeel gemaakt had, is het Eindhovense plasma-geassisteerde ALD process op de kaart gezet. In het begin hebben we veel en goed samengewerkt en uiteindelijk zijn we allebei een eigen richting opgegaan met twee proefschriften tot gevolg. Misschien lag de morele beloning voor het harde werk in de upgrade naar business class tijdens onze gezamenlijke vlucht naar Seoul!

Het experimentele werk werd ondersteund (“uitgevoerd”) door de verfrissende inbreng van stagiaires Alex, Edwin en Adrie, van afstudeerders Harm, Jeroen en Menno, en van toegevoegd onderzoekers Hans en Wytze. Alhoewel mijn technisch inzicht niet altijd op waarde geschat werd, mijn verzoeken vaak direct tot verrekkingen in de rug leidden of er gewoonweg woorden tekort schoten, was de technische ondersteuning door Jo, Ries en Janneke van onschatbare waarde. Ging er iets kapot of was er altijd iets met spoed nodig, dan werd dat in no-time geregeld. Dit proefschrift was er zonder jullie nooit geweest... of ja, zeker niet in vier jaar!

A special word of thanks to Min, Jinhee, and Yves for making my short stay at Rutgers University a very pleasant one. The hand-on experience on how to perform high-standard infrared spectroscopy, working day and even night as a team, skipping diner for science, and a lot of interesting discussions made my stay certainly something to remember.

Daarnaast wil ik Paul, Rens en Jan-Willem bedanken voor alle hulp die ik heb gekregen om dit proefschrift in de huidige vorm te krijgen. Onder het motto “Alles kan met Latex, maar even uitzoeken hoe” is het online proefschrift zowaar een interactief medium geworden!

Even belangrijk als een goede wetenschappelijk omgeving is een fijne werkplek. Na de cursussen anger-management door Peter V. en relaxed een proefschrift typen door Alquin, werd kamer Nc1.01 een toevluchtsoord door de inbreng van kamergenoten Terje, Onno en Vikram. De Belgische humor en bonbons, winkelen bij “Krudivat”, en 3D grafische designing... in twee woorden: *Super Schocker!* Maar ook de flash-bezoeken van mede-oprichter van SolTech en send-to-the-back technologieën Richard E., de diverse adviserende rollen van Joost en de inbreng van velen hebben een enorme inspiratie opgeleverd voor de noodzakelijke onzin des levens.

De koffiepauzes en de bezetting van de kantine tijdens lunch door de studenten, promovendi, post-docs en vaste staf liggen zeker aan de basis van de prettig werksfeer bij PMP. Een speciaal dankwoord aan de sportievelingen van het PEST voetbalteam voor de heroïsche overwinning (4-0!) op Spin 'm erin, warmlopen met Eugen, overschieten met Bram en het kampioenschap van de vierde klasse. Dat natuurkundigen wel degelijk kunnen voetballen bewees Bal op 't Dak dat jarenlang een hegemonie op tikkie-takkie voetbal had ondanks overschrijding van de leeftijdslimiet.

Naast het werk heb ik de afgelopen jaren mijn overige energie goed kwijt gekund. Ik wil mijn badmintonteam en voetbalteam bedanken voor de fijne sportieve sfeer en de steun toen bleek dat ik de achilleshiel was. De vele creatieve brainstormsessies met Suzy om het JVW programma in elkaar te zetten, waren daarnaast precies wat ik nodig had!

Een bijzonder woord van dank aan mijn familie en vrienden voor de steun en nodige afleiding de afgelopen tijd, zeker wanneer het soms allemaal wat te technisch leek te worden. In het bijzonder wil ik Thijs en Fanny, Jos en Agnes, mijn broers Joeri en Sander, Muriël en Lisa, en ouders George en Margreet bedanken voor de ontspannen sfeer en vele gezelligheid. Ik ben blij dat er zoveel bijzondere mensen op fietsafstand wonen.

Tot slot, wil ik mijn lieve vriendin Esther bedanken voor de fijne tijd die we samen hebben. Jouw steun en liefde zijn iets om voor thuis te komen en ik stel voor dat we de komende jaren nog veel meer samen gaan doen. Laten we beginnen met een voorproefje Hawaii in oktober!

Erik Langereis
Eindhoven, augustus 2008

Curriculum Vitae

Curriculum Vitae

Personalia

Family name	Langereis
First name	Erik
Date of birth	23 March 1979
Place of birth	Geldrop, The Netherlands

Education

1991 – 1997	Diploma Voorbereidend Wetenschappelijk Onderwijs, Strabrecht College, Geldrop, The Netherlands.
1997 – 2003	Master of Science Degree Applied Physics, Eindhoven University of Technology, Eindhoven, The Netherlands. Three months (Fall 2002) traineeship in the group of Prof. G. Possnert, The Ångström Laboratory, Uppsala University, Uppsala, Sweden. Master thesis project in the group “Equilibrium and Transport in Plasmas”, Department of Applied Physics, Eindhoven University of Technology, Eindhoven, The Netherlands.
2004 – 2008	PhD student in the group “Plasma and Materials Processing”, Department of Applied Physics, Eindhoven University of Technology, Eindhoven, The Netherlands. Four months (winter/spring 2007) working visit to the group of Prof. Y. J. Chabal, Laboratory for Surface Modification, Rutgers University, Piscataway, New Jersey, USA.